Enhancing Light In-Coupling for Thin-Film Solar Cells Using Plasmonic Nanostructures

Minh Chi To

Master Thesis in Physics,
Measurement Technology and Instrumentation

Department of Physics and Technology
University of Bergen

June 2021

Acknowledgement

My sincerest gratitude to my supervisors Assoc. Prof. Martin Møller Greve and Msc Mirjam Dyrhovden Fjell. Thank you both for the guidance, support and for all that time dedicated to reading my thesis again and again. Thank you Martin for your timely answers to all my questions and thank you Mirjam for all the tips you have shared with me.

Amongst my friends I would like to especially thank Lena Marie Setterdahl, Emilie Haugland Solheim and Ingrid Marie Stuen for being great friends and even better students such that it made me want to become better myself. I'd like to thank Andreas Havsgård Handeland for all the support and for listening to me whine every now and then, and Isabel Berg for helping me with proofreading by means of semi-snide remarks. To the rest of you, thanks for all the good times.

My love and thanks to my family. I know most of you don't have a scientific background, yet you have all shown interest in my work. And to my 3 year old niece Emma, yes, this thesis was written specifically just for you, even though you can't read yet.

Abstract

The increase in energy use, and the subsequent emission of greenhouse gases from fossil fuel usage has led Earth to the global climate crisis we are facing today. The goal of the Paris agreement is to limit global warming to below 2 °C [1], and in order to achieve this, emissions must be cut. A key to cutting emissions is to switch the energy sources to renewable ones, which emit no or very low levels of CO_2 relative to fossil fuels. One of the most promising renewable energy converters are photovoltaic solar cells. Solar cells have reached good conversion efficiencies, but still has a potential for improvement. In this thesis, the objective is to investigate if further increase in thin-film solar cell technology can be obtained using plasmonic nanostructures. The work has been carried out using a Finite-Difference Time-Domain (FDTD) simulation tool for electromagnetics. It has been determined that the light in-coupling of a CdTe and GaAs thin-film solar cell with ITO may be enhanced by adding plasmonic nanoparticles of aluminum to the front surface of the cells. The GaAs cell obtains an absorption enhancement of 0.75 %, while the CdTe cell when simulated without a glass substrate gains an absorption enhancement of 1.76%. It was found that the use of indium as a plasmonic scattering mechanism was only effective for the CdTe cell without glass substrate, where it resulted in an absorption enhancement of 0.59 %. Furthermore, it was found that the addition of the plasmonic nanoparticles to the front surface of a CdTe cell with the glass substrate gave no enhancement.

As a part of the ongoing work in the research group where this work was carried out, a part of this thesis was dedicated to test depositions of Al nanoparticles onto silicon solar cells. Al nanoparticles were synthesized by some collaborators at Rice University in the US, and deposited on silicon substrates and silicon solar cells using various deposition methods. The solar cell efficiency was compared to its pre-deposition state, and unfortunately these results did not show the positive response expected. Several potential reasons for this are suggested, such as large amount of agglomerated nanoparticles in the solution, and increased series resistances due to Al nanoparticles coated on the back of the cell. However, this needs to be investigated further before any conclusive statement can be made.

Contents

This page intentionally left blank.

List of Figures

Chapter 1

Introduction

1.1 Motivation and Background

Many devices made today need energy to function. It is becoming increasingly more common to make energy-dependent appliances, and as technology continues to advance, the need for more energy becomes apparent. The increase in the human population also necessitates more energy as there will be a higher electricity demand [2]. It is estimated that global energy consumption will increase by 50% between 2018 - 2050 [3]. Figure 1.1 depicts both global energy consumption and estimations of future regional usage.

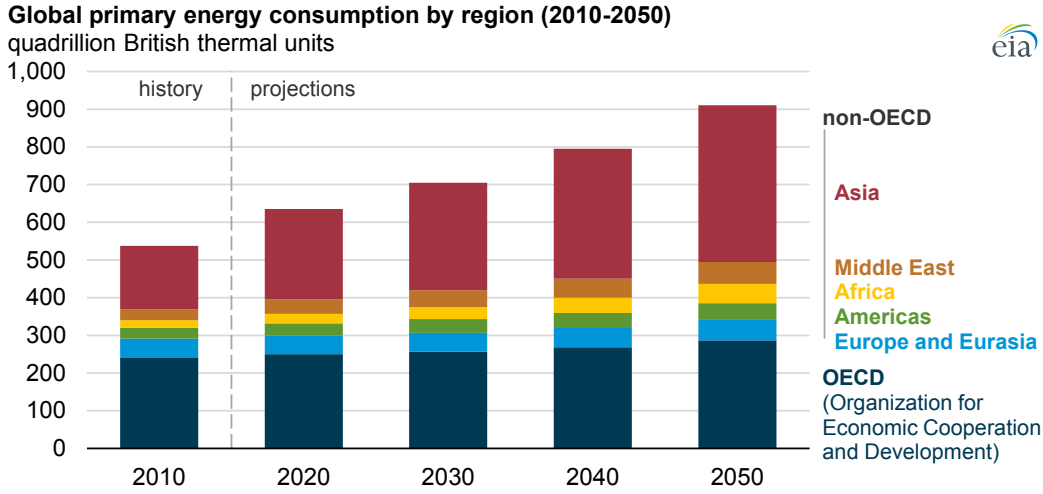

Figure 1.1: The global energy consumption from 2010 - 2050 in different regions. Note that after 2018, the global energy consumptions are projections. Figure from EIA [3].

Fossil fuel has long dominated the market, with the production and sale of these fuels representing a massive monetary industry. Fossil fuels were formed from the preserved remains of plants and animals that inhabited the Earth millions of years ago. Because of this, there is a limit on the availability of these energy sources, as there is no feasible way to replenish them [4]. In addition, a byproduct of using fossil fuel is the emission of greenhouse gases. Figure 1.2 illustrates the total and individual contributors of global

carbon emission of fossil fuel from 1750 - 2014. As can be seen, the total amount of carbon emission is growing at a steep rate due to the use of fossil fuels [5].

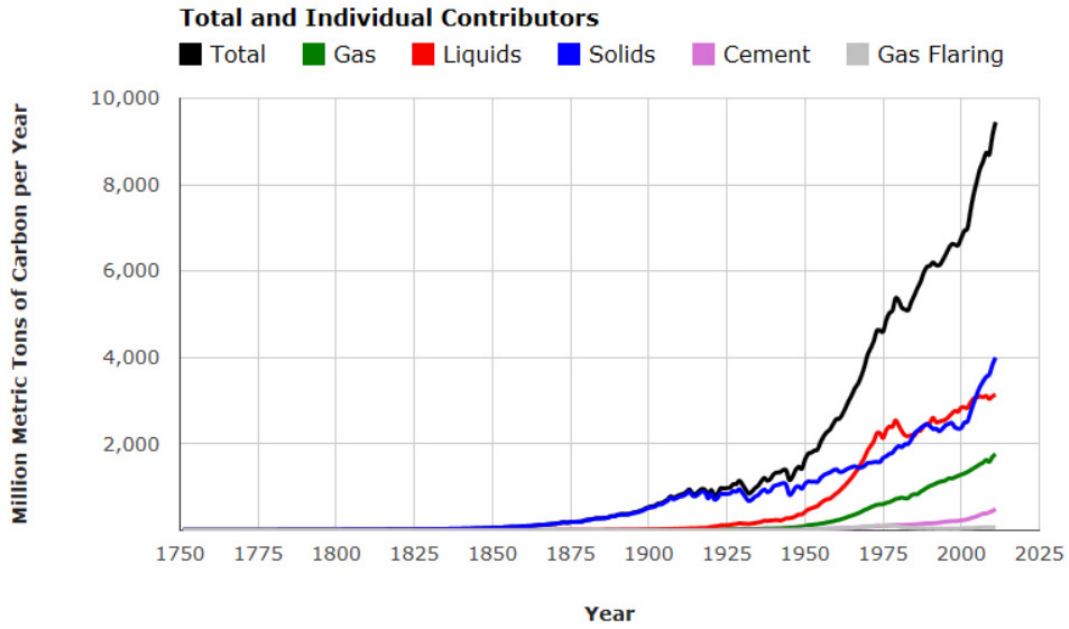

Figure 1.2: Global fossil fuel carbon emission from individual contributors and the combined total amount per year from 1750 - 2014. Figure from CDIAC [5].

The increase in energy consumption in the coming years, the limited stock of fossil fuel, and its serious drawback of massive carbon emission indicate that new energy sources must be considered. Preferably, the new energy sources should not have limited stock and have a low carbon emission to limit the damage to the environment. Renewable energy allows for the energy production from sources capable of consistent regeneration and without the same large amount of pollutants that fossil fuels produce [2]. Therefore, renewable energy is essential for the future, especially if the world is to limit global warming to below 2°C, which is the goal of the Paris agreement [1].

Renewable energy has been available for years, but fossil fuel has remained the largest percentage of energy production due to its high-energy return on investment. In the recent decade, renewable energy has become less expensive due to research and technological advances. Nevertheless, it is still necessary to find new ways to make renewable energy more cost-efficient to replace fossil fuel completely [6].

A prominent renewable energy source is solar power, as the sun provides a close to limitless amount of free energy. Solar cells have long been available commercially. The price of solar cells has dropped to a reasonable price point [7], and so it is expected that solar cells will become more utilized in the future. In 2019, PV systems contributed to 2.6% of the global power generation. The cumulative solar power capacity had risen from 516.8 GW in 2018 to 633.7 GW by the end of 2019. Solar power is currently under

strong growth, although due to the Covid-19 pandemic, had lower growth than what was expected in 2020. It is estimated that the impacts due to the pandemic will only end in 2024. Despite the drawbacks from the pandemic, it is estimated that by the end of 2022, the global solar power generation capacity will reach terawatt levels [8], indicating that solar power will keep growing at a fast pace.

Most solar cells are fabricated from silicon and can be either crystalline, polycrystalline, or amorphous [2], where the majority is the crystalline type. The thickness of the silicon wafer tends to be hundreds of micrometers thick ($\sim$ 300 µm). The refining steps of Si are expensive in terms of money and energy consuming, and there is, therefore, much research into reducing the thickness of the Si wafer without negatively affecting the efficiency significantly [9]. There is also research into other suitable materials that can be made with a low thickness, which are referred to as thin-film solar cells, and they are also available commercially on a large scale. These types of solar cells are often considered as an alternative to the usual crystalline silicon cell. As the name implies, these solar cells consist of thin films with an average thickness of $\sim$2 µm [9] and can therefore be considerably cheaper to produce due to the smaller amount of material necessary.

Thin-film solar cells currently have lower efficiency than Si solar cells [9]. However, further research is currently being conducted in efforts to improve the efficiency. The efficiency of a solar cell is directly correlated to the amount of light absorbed in the absorbing layer. Thus, an avenue for improvement is to modify the optical properties of a solar cell so that light in-coupling in the absorbing layer is increased. Such improvements can be made by implementing light trapping methods [10], which are applications that can enhance light confinement and absorption in solar cells [11].

A particular method to increase the efficiency of a cell involves using plasmonic structures for light manipulation at a sub-wavelength scale. Plasmonic nanoparticles can significantly impact the absorption of a solar cell by scattering the incident light into the absorbing layer within specific spectral regions [10]. In most work involving plasmonic structures, gold or silver has been commonly used and studied [12] due to their convenient characteristics. These metals have relevant optical properties and exhibit strong light interaction in the visible range. However, the materials are expensive due to scarcity, and exhibit light absorbance in the visible range. Research into other plasmonic metals as alternatives is currently an ongoing field of study, where aluminium and indium are promising candidates [13].

1.2 Objective

The primary objective of this thesis is to investigate enhancement in light in-coupling in CdTe and GaAs thin-film solar cells and consequently light trapping, using plasmonic nanoparticles of aluminium and indium. The results will be compared to literature, and the literature results will be cross checked in simulation where this is possible.

The secondary objective is to experimentally investigate the effects of adding plasmonic Al nanoparticles on silicon substrates and crystalline silicon solar cells.

1.3 Limitations

Experimentally adding the metallic nanoparticles on CdTe and GaAs solar cells was not possible to complete due to not having access to the thin-film cells. After we obtained promising theoretical results, we have reached out to several research groups to assist in fabricating the required substrates. However, unfortunately, we did not manage to establish a working collaboration within the time frame of this master thesis. Instead of using CdTe or GaAs, a silicon solar cell was utilized. Silicon is already an important research topic in the research group where this thesis has been carried out and this objective is an important step in the experimental realization for both (silicon and thin-film) solar cell technologies. Furthermore, only Al nanoparticles were available for experiments.

The ongoing pandemic lead to a severe hindrance in performing experimental work. Therefore, only a small amount of data was collected due to several push-backs and a limited time frame.

1.4 Thesis Outline

The outline of the thesis is as following:

Chapter 1. Introduction: Motivation and background is presented, as well as the thesis objective.

Chapter 2. Theory: Theoretical background behind solar cells and plasmonics is described here, as well as some information about the FDTD simulation tool.

Chapter 3. Methods: Describes the processes and steps carried out in the simulation and experimental part.

Chapter 4. Results and Discussion - Simulation: Results and discussion for the simulations of the CdTe and GaAs solar cells are presented here, along with the

replication of the setups based on existing literature pertaining to the GaAs cell.

Chapter 5. Results and Discussion - Experiment: Results and discussion for the deposition of Al nanoparticles onto Si substrates and a Si solar cell, and the cell's efficiency post-deposition.

Chapter 6. Conclusion: An overall conclusion of results obtained from simulations and experiments, and potential further work.

This page intentionally left blank.

Chapter 2

Theory

The theoretical background of the thesis is introduced in this chapter. A detailed description of photovoltaics and its fundamentals is described in the first part. Secondly, a cursory description of plasmonics is given. Thirdly, a brief introduction in light-matter interaction, and finally, a short introduction to the finite-difference time-domain simulation tool from Lumerical is described.

2.1 Photovoltaic Solar Cells

Photovoltaic (PV) solar cells, more commonly referred to simply as solar cells, are technological devices that convert sunlight into electrical energy [14]. Some of the electronic components in the cells produce electricity when exposed to photons through a process called the photovoltaic effect [15].

Solar cells can be divided into three major generations. The first generation is the wafer-based crystalline silicon cells, which can be divided into mono- and poly-crystalline [14]. The second generation is the thin-film cells, which are thin semiconductor substrates that are commonly deposited on large economical substrates such as glass, polymers, or metals [16]. The third generation utilizes sensitized structures, such as dye-sensitized cells, quantum dot materials, or perovskite-based solar cells [14][16].

An essential aspect of all solar cells is the absorption of photons via the excitation of electrons, as this is a vital part of electricity production. For photons to excite electrons into a higher energy state, they need to have sufficient energy to transfer over to the electrons since electrons can only have specific energy values. The minimum energy that the electrons need to absorb to be sufficiently excited can be determined by investigating the allowed electron energies [17][18].

2.1.1 Energy Band

When considering isolated atoms, their orbiting electrons are found to have discrete energy values that are separated by relatively large gaps. If these atoms are in a solid

and the interatomic distance between them decreases to only a few ångström (Å), then it will cause interaction amongst the atoms, and the identical discrete energies will split into many different values. Thus, the discrete energy values have turned into energy ranges with energy values so close that they seemingly form a continuum. These energy ranges form regions with allowed electron energies and are known as *energy bands* [18]. The energy bands are separated by a spacing called the *bandgap* that interrupts the continuum [19]. These energy bands may either be filled, partially filled, or empty of electrons. The minimum number of energy states in an energy band is twice the number of atoms in the material. The factor of two is due to the $1/2, -1/2$ spin of the electrons, so that each energy level may contain two electrons with opposite spin [20].

Statistic Distribution of Electrons

Electrons must follow the *Pauli exclusion principle*, which states that they cannot exist in the same energy states. So at absolute zero, the electrons will pack into the lowest available energy states and become a "sea" of electron energy states. The surface of this sea is referred to as the *Fermi level* or as the *chemical potential*, and no electron will have enough energy to rise above this level at absolute zero. A certain fraction of the electrons will occupy energy states above the Fermi level at temperatures above absolute zero. This fraction is characterized by the *Fermi-Dirac distribution* [21].

The Fermi-Dirac distribution gives the probability that a certain available energy state will be occupied at a given temperature and has the form shown in Equation 2.1 [21], where E_e is the electron energy [18], k is the Boltzmann constant, T is temperature, and E_F is the Fermi level [21].

$$f(E_e, T) = \frac{1}{\exp[(E_e - E_F)/kT] + 1} \tag{2.1}$$

The Fermi level is often on the order of a few electron volts (e.g. 7 eV for copper), while the *thermal energy* kT is only about 0.026 eV at 300 K. By putting these numbers into Equation 2.1, the probability is essentially 1 for energies below the Fermi level. Thus, the nature of the function shown in Equation 2.1 dictates that at room temperature, most of the energy states below the Fermi level are occupied as $f(E_e, T) \approx 1$. Only a few electrons have energies above the Fermi level as the function will rapidly approach 0, $f(E_e, T) \approx 0$, for increasing energies [21].

The distribution function for a temperature at absolute zero and a finite temperature is illustrated in Figure 2.1. The dashed line represents the distribution function at absolute zero. When the electrons have energy lower than the Fermi level, the distribution function is 1. When the electrons have energy above the Fermi level, the function is 0, which means that all the states below the Fermi level are occupied while the others are empty. When the temperature is finite, the function no longer has a decisive drop at the Fermi level, meaning the occupation probability is no longer 1 or 0, but instead somewhere in between [17]. This leads to the possibility that energy states above the Fermi level may be occupied.

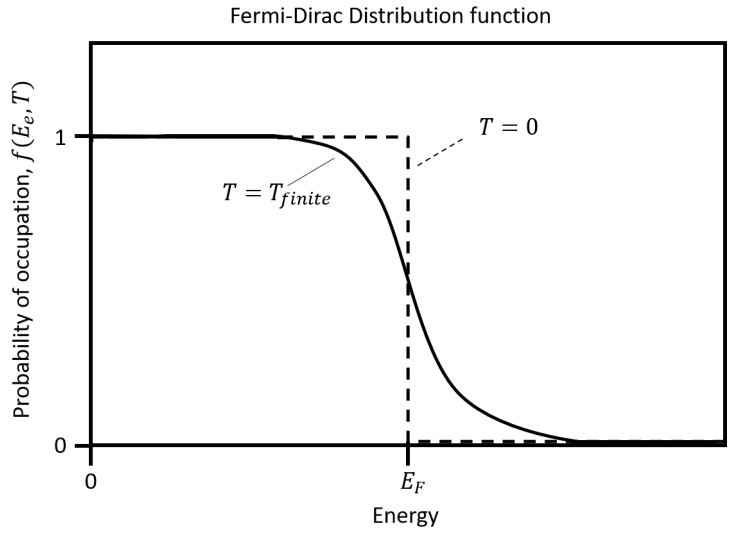

Figure 2.1: The probability of occupation of energy states for T = 0 K, and T = T_{finite} K.

The implication of the distribution function for energy bands is illustrated in Figure 2.2. In Figure 2.2a, the temperature is at absolute zero, and the distribution function has a well-defined edge at the Fermi level. There are no electrons with energy above the Fermi level, and so only the available energy states below the Fermi level are occupied. Note that only the colored area has available energy states, as there are none in the bandgap. Figure 2.2b depicts the distribution function when the temperature is above zero, and the function, as we know, no longer has a well-defined edge around the Fermi level. The function crosses the Fermi level, and if the gap between the energy bands is small enough, it can travel into the higher energy band such that the probability of occupation allows a small number of electrons to occupy the energy states in the higher energy band [21].

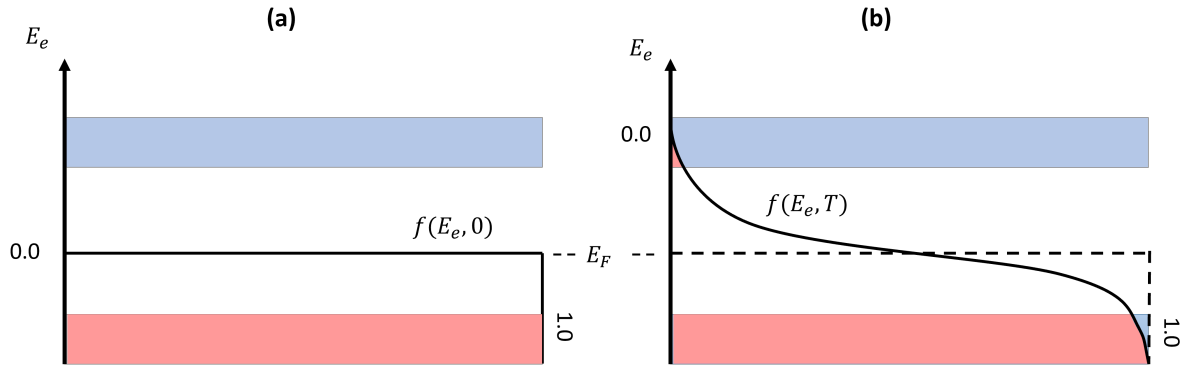

Figure 2.2: The probability of occupation of energy states when the temperature is 0 K, and the temperature is finite. The pink color represents occupied energy states.

So, at high temperatures, electrons may have sufficient energy above the Fermi level such that they may cross over the gap that separates the energy bands [21]. These electrons

will then contribute to conduction in the material. Thus, the spacing between the energy bands, the number of electrons occupying the bands, and the temperature will determine whether a material is an electrical insulator, a semiconductor, or a conductor [19].

2.1.2 Semiconductor

A semiconductor is a material that can be both an insulator and a conductor. The semiconductor has a bandgap that separates the energy bands of a certain width, E_G, such that at low temperatures, no electrons can occupy energy states above the Fermi level and the semiconductor may act as an insulator. When the semiconductor is heated to room temperature or higher temperatures, there is a finite probability that some electrons may occupy energy states above the Fermi level [21]. This will allow the semiconductor to conduct electricity and act as a conductor [19].

A semiconductor at absolute zero will have an energy band that is fully occupied, while the next band at a higher energy is empty. The highest occupied band is referred to as the *valence band* (VB), while the lowest unoccupied band is called the *conduction band* (CB) [17]. At a finite temperature, some of the electrons may occupy energy states in the CB. See Figure 2.3 for an illustration.

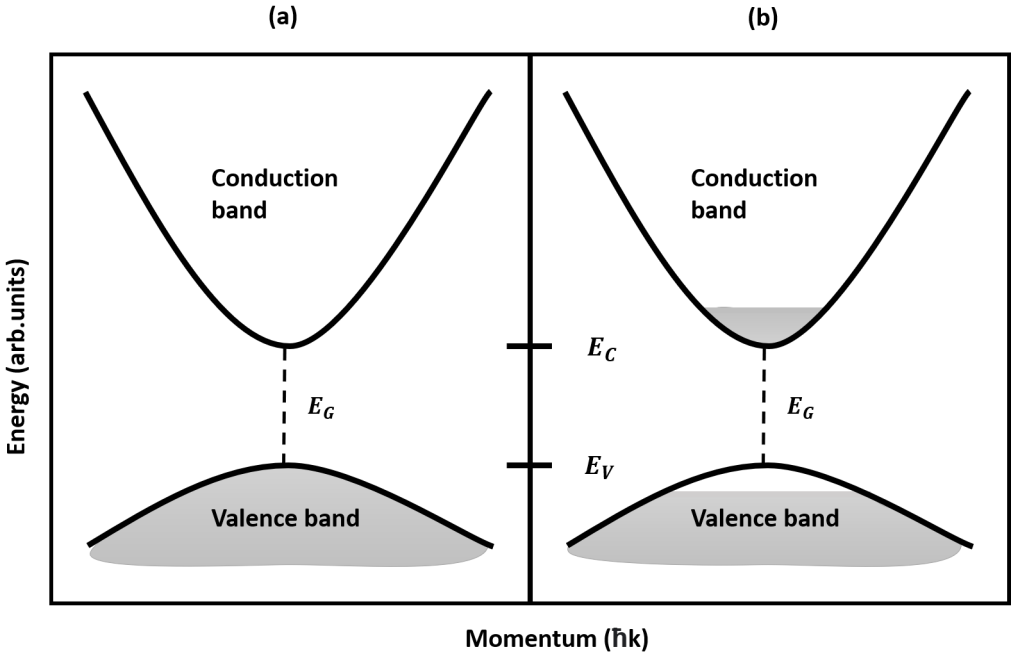

Figure 2.3: (a) The VB and CB for a semiconductor at absolute zero with an energy gap of E_G. (b) At a finite temperature, some of the electrons will occupy the CB instead of the VB. Note that this figure is analogous to Figure 2.2.

When an external electric field is applied to a semiconductor, an electron in the VB may move in response to the field. The electron jumps across the bandgap into the empty conduction band [19] through the absorption of a photon. The photon must have an energy of at least $\hbar\omega = E_G$, where ω is the angular frequency. Photons without the required minimum energy cannot excite electrons into the conduction band [18]. Increasing the temperature also gives rise to a situation where the electrons may jump across the bandgap by gaining energy from thermal motion. This is especially the case for semiconductors as they have a relatively small bandgap [19].

When electrons from the valence band get excited well into the conduction band by a photon, they start losing energy by step-wise generating phonons of energy E_Γ until they reach the conduction band edge, see Figure 2.4. Losing energy in small steps by step-wise phonon production is no longer possible as there are no available states for electrons with a little less energy. Thus, the next step is to return to the valence band. However, that requires the loss of energy equivalent to the bandgap E_G. One possible process is the emission of a photon. Another process is the simultaneous generation of a large number of phonons. As a result of the interruption of the step-wise phonon generation, the electrons may exist upwards to 10^{-3} s in the CB. This is a much larger time compared to metals, where the electrons only exist for 10^{-12} s in the CB. The amount of time that the electrons exist in the CB for semiconductors is what allows the conversion of electron energy into electrical energy to happen [18].

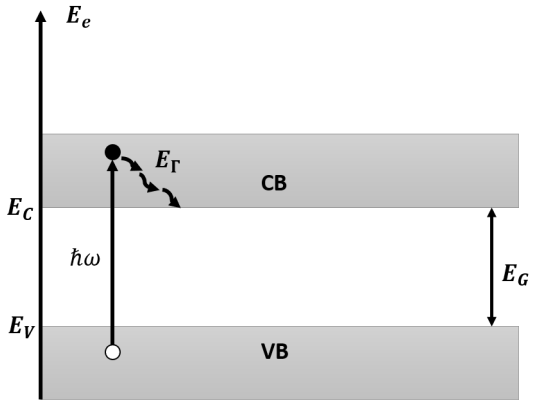

Figure 2.4: Excitation of an electron in the VB by the absorption of a photon of energy $\hbar\omega$ and then step-wise phonon production until the electron reaches the lowest energy of the CB. Redrawn from Würfel et al. [18].

When an electron is excited into the CB, it leaves behind a vacancy in the VB. This vacancy is referred to as a **hole**. A neighbor electron may move into the vacancy and thereby make the hole "move" by shifting the vacancy position. In this way, the hole can act as a charge carrier. When an electric field acts on the semiconductor, the charge carriers move in the opposite direction, and thus, holes act like a positively charged particle. In a pure semiconductor, also referred to as an *intrinsic* semiconductor, the number of valance holes and conduction electrons are equal in numbers [19].

There are by definition two classes of semiconductors, *direct* and *indirect*. Conservation of energy and crystal momentum is vital for the interaction between electrons, holes, and photons [22]. The crystal momentum is the associated momentum-like vector of electrons in a crystal lattice. This momentum is associated with the wave vectors **k** of the crystal lattice by Equation 2.2 [23].

$$\mathbf{P}_{crystal} \equiv \hbar\mathbf{k} \tag{2.2}$$

Whether a semiconductor is direct or indirect depends on its bandgap. The lowest energy state in the CB and the highest energy state in the VB are characterized by a certain crystal momentum (**k**-vector), respectively. If the crystal momentum for the electrons in the CB and the holes in the VB are the same, then the semiconductor has a direct bandgap and is a *direct semiconductor*. Figure 2.3 is an example of a direct bandgap. There is no difference in momentum for the maximum and the minimum of the VB and CB in the figure. Therefore, the excitation of electrons occurs with the smallest possible energy, $E_C - E_V = E_g$. This type of transition is called a *direct transition* [18].

If the crystal momentum is not the same, then the bandgap is indirect. Figure 2.5 depicts an *indirect semiconductor*. As can be seen, the maximum of the VB and the minimum of the CB do not have the same momentum. Excitation from the VB into the CB is not possible from only low-energy photon absorption as the photon's momentum is too small. In this case, excitation is only possible with a change of momentum, and it necessitates the participation of some other "particle," such as a phonon. This type of transition is called *indirect transition* [18].

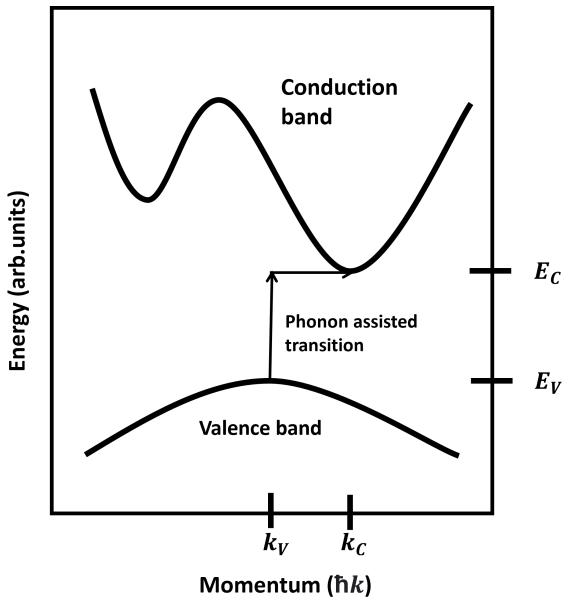

Figure 2.5: Illustration of an indirect semiconductor. The maximum of the VB and the minimum of the CB do not occur for the same momentum, so the transition must be phonon-assisted.

Doping

Combining a semiconductor with another material may lead to electric conductivity, as minimal amounts of impurities strongly influence the conductivity. Thus, it is essential to precisely control the impurity concentration in the construction of semiconductor devices [17].

Doping is a process where impurities are intentionally introduced into intrinsic semiconductors. A doped semiconductor is referred to as an extrinsic semiconductor. The introduced impurity will replace an atom of the semiconductor material in the atomic lattice. The two types of impurities are known as n-type and p-type [24]. Figure 2.6 illustrates the replacement of an arbitrary atom Z, with either an n-type or a p-type, where D and A represent the respective types.

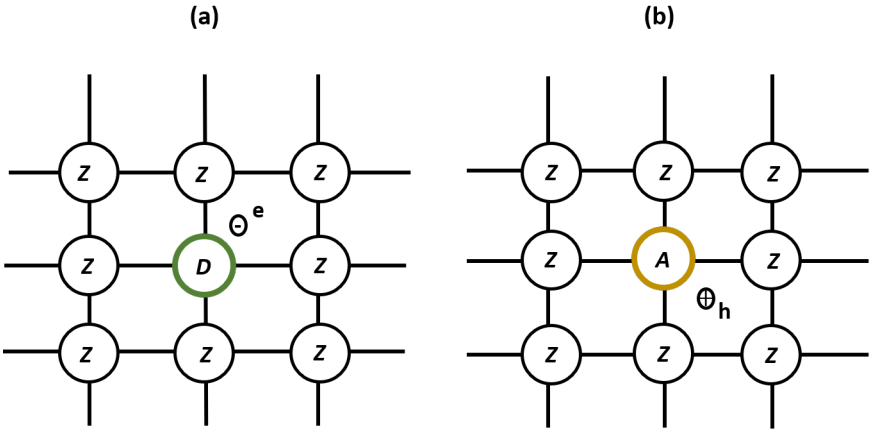

Figure 2.6: (a) An n-type atom has replaced the arbitrary atom Z, which results in an additional electron. (b) A p-type atom has replaced the arbitrary atom Z, which results in an additional hole.

N-type doping involves an introduced impurity that has a larger charge amount than the semiconductor material. There will then be an excess electron since the impurity has more than the necessary amount to form covalent bonds with its neighboring atoms. The extra electron is only loosely bound and will add an extra net-effective charge of $+e$ to the impurity, where e is elementary charge. The energy level of the excess electron will be slightly below the conduction band. See Figure 2.7a. This level is called a *donor level*, and the impurity is called a *donor*. The short bandgap between the conduction band and donor level makes it easy for the electrons in the donor level to jump to the conduction band. The overall effect is that the conductivity increases by a large margin, and the increased conduction is due almost entirely to electron motion [19].

P-type doping has an analogous effect to the n-type doping, however, the impurity has a lower charge amount than the semiconductor material. The impurity will not have enough electrons to form the required number of covalent bonds. To fulfill all the required covalent bonds, it can steal an electron from a neighbor atom. This creates a

neighbor atom with a vacancy that lacks an electron. The vacancy will act as a positive charge and as discussed can be illustrated as a hole. The stolen electron is bound to the impurity, or acceptor in this case, in an energy level called the *acceptor level* located slightly above the valence band. See Figure 2.7b. The conductivity for a semiconductor doped with acceptors is almost entirely due to hole motion [19].

As shown in Figure 2.7, the introduction of impurities causes the Fermi level to change considerably depending on the doping type. When the p-type and n-type are combined, they form a junction of great importance.

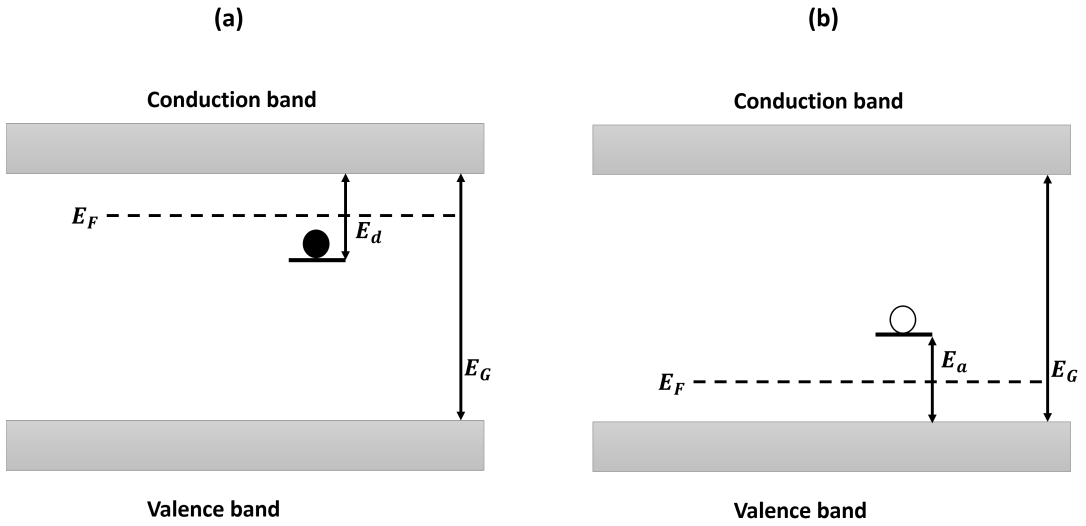

Figure 2.7: (a) The donors add additional electron energy levels close to the CB with an energy gap of E_d. The electrons that inhabit this level can then be easily excited into the CB. (b) The acceptors add additional hole energy levels, which the electrons in the VB can easily excite into due to the low energy gap E_a and leave excess holes in the VB [25].

The pn-junction

The junction between a p- and n-doped semiconductor is referred to as a pn-junction. In Figure 2.8, p- and n-doped semiconductors are step-wise joined together. Figure 2.8a shows the semiconductor while they are still separate. The Fermi level, E_F, of the p-doped is close to the valence band, while for the n-doped, it is close to the conduction band. The majority carrier in the p-doped are holes, and most of the acceptors are negatively charged. The majority carrier in the n-doped are electrons, and the donors are primarily positively ionized [17].

In Figure 2.8b, the two semiconductors are joined together, with the electrons from the n-side diffusing into the p-side and holes from the p-side diffusing into the n-side. When these mobile charge carriers meet, they recombine. This leaves a region of immobilized ionized acceptors and donors without the compensating charge from the generated carriers. This region is called the *depletion zone* due to its lack of mobile carriers

[17][26]. An electric field arises due to the excess and lack of electrons relative to the number of ions on either side. The field is located between the two sides and is marked by ϵ in the figure. The field represents an obstacle for the holes and electrons, so that moving into each other's side becomes difficult. As the depletion region widens, the electric field increases in turn, and this is a process that will happen until equilibrium is achieved [17].

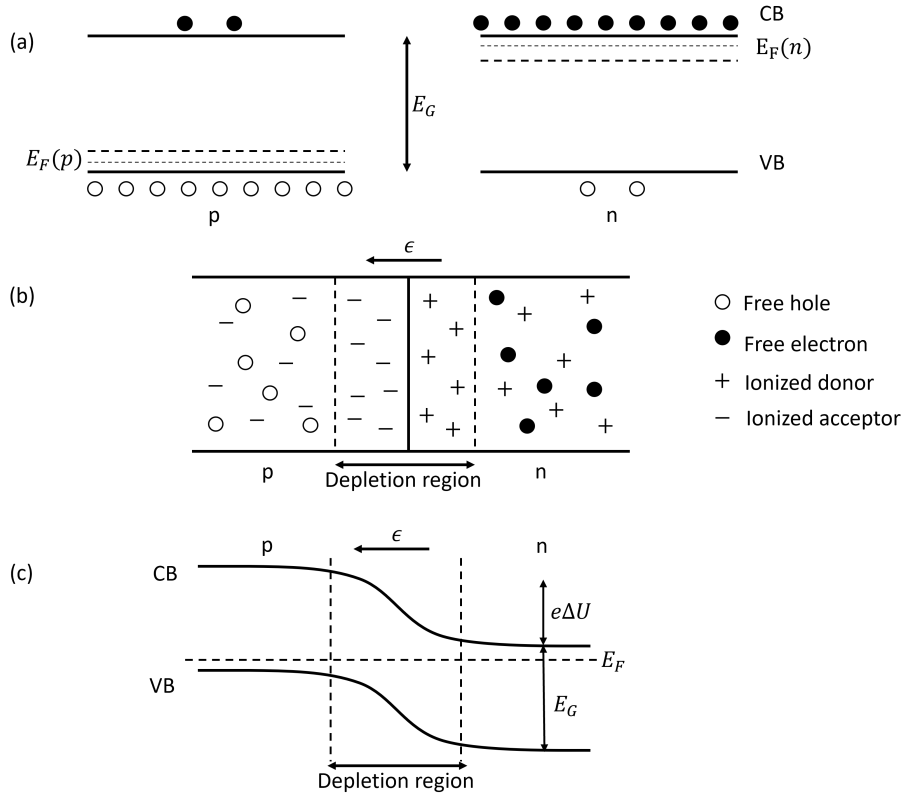

Figure 2.8: (a) p- and n-type doped semiconductor before combination. (b) the initial stage of charge diffusing into the opposite side. (c) the need for the Fermi level to be aligned forces the energy levels to bend. Redrawn from Hofmann [17].

Figure 2.8c depicts the last stage of combining p- and n-type semiconductors. When in thermal equilibrium, the Fermi level has to be aligned in energy for the whole system, which necessitates a macroscopic potential in the depletion layer. This will cause the energy levels to shift and "bend" the energy bands [17].

When an electron absorbs electromagnetic radiation of sufficiently high energy in the pn-junction, it can generate electron-hole (e-h) pairs in the depletion zone [24], or it can create e-h pairs outside the zone. However, these outside pairs may easily recombine unless they diffuse into the depletion zone. The e-h pair in the depletion zone will immediately be swept into the opposite direction due to the electric field. The holes will then drift into the p-side, while the electrons will drift into the n-side [27]. The motion of the carriers due to the electric field will produce a *drift current* [24].

The pn-junction may consist of two semiconductors of the same material, which have been p-doped and n-doped, respectively, or it might consist of two different materials. When the pn-junction consists of the same material, it is referred to as a homojunction. If the n-type and p-type are not of the same material, then the pn-junction is referred to as a heterojunction.

2.1.3 The Layers of a Solar Cell

The mechanism behind solar cells is based on three factors; (1) Absorption of light that will generate charge carriers, holes (p-type), and electrons (n-type), (2) separating the charge carriers and (3) collecting the separated charge carriers at respective electrodes [14].

Even though a solar cell could be made with only a pn-junction, it typically consists of many layers of materials, where each of them has a specific purpose. Figure 2.9 illustrates a generic solar cell. The most critical layer of the cell is the pn-junction layer, as it is this layer that generates current. Another important layer is the *Anti-Reflection Coating* (ARC) which is applied to the illuminated side of the cell. This will be further discussed in Section 2.3. Note that not all solar cells use ARC. The PV cell will have a front and back contact consisting of conducting material to collect the produced e-h pair [15].

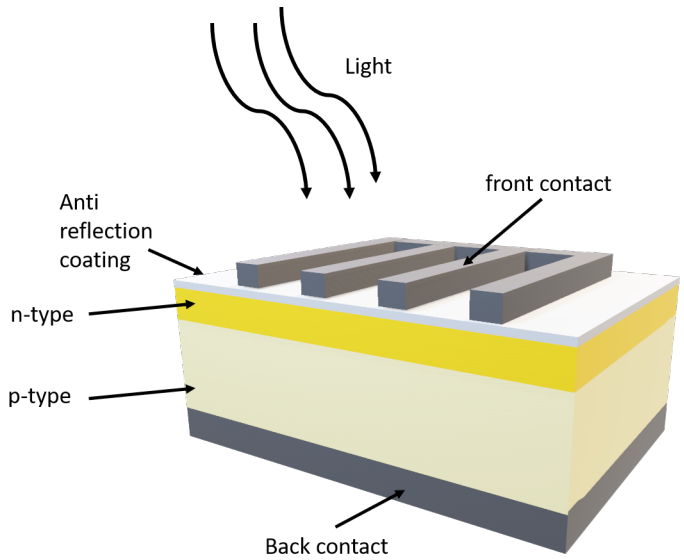

Figure 2.9: The basic build up of a solar cell. Note that the front contact does not cover the entire front surface such that it does not block too much of the incoming light.

In many solar cells, transparent conducting oxides (TCOs) are utilized as the front contact as they have high electric conductivity and high optical transparency [28]. The most common TCOs are doped metal oxides, such as $ZnO{:}Al$, $In_2O_3{:}Sn$ (referred to as ITO), and $SnO_2{:}F$ [29].

2.1.4 Shockley-Quisser Limit

When a solar cell is made of a single pn-junction (single-junction), it will have a theoretical upper limit to the solar conversion efficiency for a given illumination spectrum. This limit is known as either the *detailed balance limit* or the *Shockley-Queisser limit* [30].

The Shockley-Queisser limit postulates that all photons with energy above the bandgap will create e-h pairs, which will yield one electron per absorbed photon that will contribute to the electrical current. It also assumes that all e-h recombination events are radiative and will re-emit light. The limit only considers thermodynamic properties and will therefore always give slightly higher efficiency compared to what is realistic [31].

Shockley and Queisser first described the detailed balance limit in 1961 [32]. They described the ultimate efficiency of an ideal pn-junction illuminated by the sun, with the sun spectrum approximated by the emission of a black body whose surface temperature is 6000 K [30]. They found that for a solar cell at a temperature of 300 K with a bandgap of 1.1 eV, that the maximum efficiency was 30% [32].

The solar spectrum that reaches the Earth is today described by two terrestrial spectral irradiance distributions, where the first distribution, AM 1.5D, is 48.2% tilted on the Earth and includes only the direct sunlight. The second distribution, AM 1.5G, is also 48.2% tilted on the Earth, but it includes both the direct sunlight and the sunlight scattered by the atmosphere. Note that AM stands for air mass and is defined by $1/\cos\theta$ [30]. Figure 2.10 depicts spectral irradiance distributions AM 1.5D, AM 1.5G, AM 0, and the black body approximation of the sun, where AM 0 is the extraterrestrial irradiance distribution just outside the atmosphere.

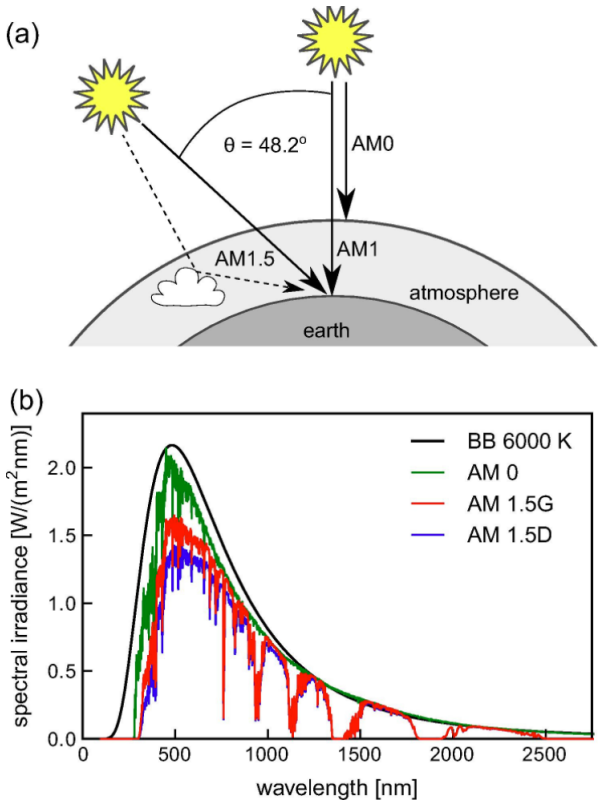

Figure 2.10: (a) Schematic representation of AM 1.5D (direct solid arrow down to earth), AM 1.5G (both solid and dashed angled arrows), and AM 0 (direct solid arrow down to atmosphere). (b) Spectral irradiance of a black body, AM 0, AM 1.5G, and AM 1.5D. Figure taken from Rühle [30].

The integrated power density of AM 1.5D, AM 1.5G, and the black body approximation are 900.1 W/m^2, 1000.4 W/m^2, and 1576.7 W/m^2, respectively. As shown in Figure 2.10b and the integrated power densities, the black body approximation gives a substantially higher spectral irradiance than the standard AM distributions. Thus, the limit calculated by Shockley-Queisser is not entirely accurate [30].

When calculated using AM 1.5G and a solar cell at temperature 298.15K (room temperature), the detailed balance limit is around 33.7%, which occurs at a bandgap of 1.34 eV. This theoretical upper limit only applies to solar cells that use a single pn-junction to collect power [30].

The spectral response of several solar cell materials are shown in Figure 2.11, which indicates which parts of the solar spectrum they can absorb photons in [33]. The spectral response of CdTe and GaAs is of particular interest in this thesis, as thin-film solar cells of these materials will be investigated.

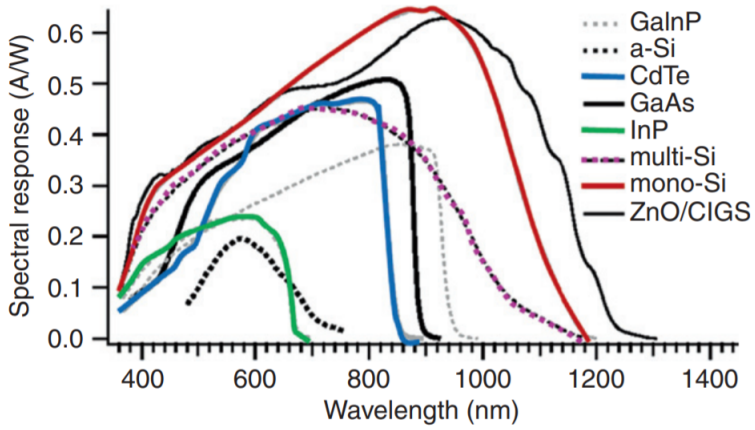

Figure 2.11: The spectral response of GaInP, a-Si, CdTe, GaAs, InP, multi-Si, mono-Si, and ZnO/CIGS. Figure taken from Myers [33].

2.1.5 Thin-Film Solar Cells

As stated previously, there are mainly three generations of solar cells. The most commonly used of these three is the first generation, the wafer-based silicon cells, as they have many advantages compared to other materials. It does, however, have one substantial disadvantage of having poor absorption of light [18]. The material cost must also be considered, as silicon wafers and their large thickness can be costly to produce [9].

Thin-film solar cells are often seen as an excellent alternative to silicon cells. The thin-film cells have the advantage of only needing a thickness of a few micrometers to be able to absorb most of the part of the solar spectrum that holds interest. These cells commonly have direct bandgaps and have large absorption coefficients as well. All these advantages point to solar cells with a significantly lowered cost to produce [18].

Due to the low thickness of thin-film cells, the proximity to the surface with its high surface recombination makes it necessary to have a buffer layer on the front surface. There should not be e-h pairs produced in this layer, and it must have a large bandgap. This layer is called a *window layer*, and it should let photons pass through unimpeded and keep electrons and holes from recombining at the front contact. It is also necessary that the interface between the window and absorbing layer have a low density of interface states so that recombination does not occur there [18].

A disadvantage with many materials that have direct bandgaps and favorable energy bands is that doping them does not give an equally good n-type and p-type. Therefore, the structures of thin-films are, most of the time, heterojunctions. An example of a heterojunction is the CdS/CdTe junction [18]. There are some exceptions like, GaAs, whose structure is that of a homojunction.

CdTe Thin-Film Solar Cell

Cadmium sulfide (CdS) and cadmium telluride (CdTe) combined form a heterojunction, where the CdS is the window layer, and the CdTe is the absorbing layer [34]. A CdS/CdTe solar cell, commonly referred to simply as a CdTe cell, was one of the first thin-film polycrystalline cells ever made, and panels with these cells have been commercially produced since the mid-90s [26].

A typical cell consists of a CdS layer deposited on a conducting glass plate with a thickness ranging from 60 - 100 nm, followed by a CdTe layer with a thickness of 2 - 4 microns. There is also a back contact consisting of some current-carrying metal [26][34].

The cell has relatively high stability, and the technology needed to produce it is relatively simple. It also has a direct bandgap of energy 1.5 eV and a spectral response occurring around the wavelength region 400 - 870 nm, as shown in Figure 2.11. This makes it very attractive for mass production, along with its average efficiency at about 16% [26], where state of the art CdTe cells have reached efficiencies as high as 22.1% [35]. The short circuit current density of the cell usually averages around 16 to 26 mA/cm^2. Cadmium by itself is highly toxic, but the environmental hazard can be negated by encapsulating it. The Earth's reserves of cadmium are limited, which limits mass production [26].

The initial production of CdTe solar cells happens step-wise by evaporating a thin CdS layer on top of a conductive glass substrate, followed by another evaporation of a CdTe layer and then deposition of a metal contact layer. The cell is then heat-treated in ambient oxygen for a short while, usually at temperatures around 450 °C and a flux, typically $CdCl_2$, that will cause partial crystallization of the two semiconductors [26].

The back contact will typically consist of a thin Tellurium layer followed by a copper layer, which will then be etched in a Br_2-methanol solution. After etching, the back contact will be covered in a current-carrying metal contact such as Au, or Mo. The back contact is completed by baking the CdS/CdTe cell at temperatures between 300 to 500 °C [26].

There are large degrees of variation when it comes to the methods of production. Some may choose another form of deposition, or perhaps temperature treatment. The choice of processing steps often stems from economic reasons [26][36].

GaAs Thin-Film Solar Cell

A gallium arsenide (GaAs) thin-film solar cell has shown exceptionally high efficiency of 29.1% [31]. In addition, it has a direct bandgap of 1.42 eV [16] and has a spectral response around wavelength 400 - 870 nm. This makes producing thin-film cells using GaAs very attractive [37]. However, GaAs cells suffer from high surface recombination [38] and are quite expensive to manufacture. The cost has been a major limiting factor in producing this thin-film cell, and GaAs cells are mostly used for spacecraft and satellites [39].

The measured short circuit current density of GaAs cells may be anywhere from 15 to 30 mA/cm^2, depending on both thickness and light trapping methods [40]. There are multiple ways to produce a single-junction GaAs cell. The more common ways are through chemical vapor deposition or evaporation [41]. For high-performance cells, GaAs thin-films are usually made by epitaxial lift-off, enabling highly reflective back contacts [37].

2.2 Plasmonics

Plasmonics is a research field within nanophotonics related to the interaction between electromagnetic (EM) waves and conduction electrons in conductors (metals, semiconductors, semimetals). Plasmonics is based on the phenomenon called plasmons, where the plasmons consist of conduction electron plasma and EM waves [11].

2.2.1 Surface Plasmons

A surface plasmon (SP) can be defined as the oscillation of conduction electrons at the interface between two materials where the real part of the permittivity has opposite sign [42]. SPs are mainly divided into two types based on their propagation characteristics along the interface. The first type is called surface plasmon polaritons (SPP), and they *propagate* along the interface. They occur when the interface surface is planar. The second type is called localized surface plasmons (LSP), which are *non-propagating* and occur for metallic nanoparticles [11]. The distinction between SPPs and LSPs is that the former occurs when the area is semi-finite, while the latter occurs when the area is enclosed or localized.

SPP is a surface charge density wave [43] that arises when the incident EM radiation couples with the conduction electrons of a metal and thereby excites an oscillation [44]. In other words, SPPs occur when SPs interact with light. The EM surface wave amplitude decays exponentially with distance normal to the interface in either direction, meaning away or into the dielectric [45][46], and therefore does not carry any energy away from the interface, which leads to the name *near-field* [47].

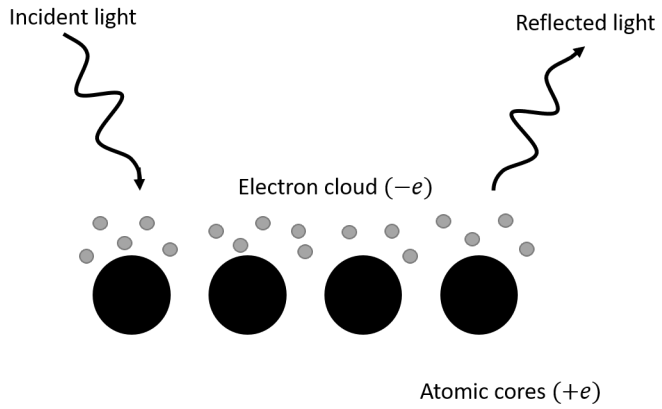

Figure 2.12: A depiction of the polarization effect caused by the movement of the conduction electrons due to incident light excitation, where the atomic cores are positively charged, and the electron cloud is negatively charged. Redrawn from Solanki et al. [11].

LSPs are the excitation of the conduction electrons of metallic nanoparticles coupled to the incident EM field [44]. When EM waves are incident on a nanoparticle, they cause movement of the conduction electrons via excitation. The excitation will cause the electrons to behave as an electron gas, and lead to polarization of the nanoparticles due to the displacement of the electrons from the cores, see Figure 2.12. The electron gas will be negatively charged, while the atomic cores are positively charged [48].

Due to the polarization in the particle and the surrounding medium, a restoring force will act upon the polarization charges. This will lead to the confinement of the electrons to dimensions smaller than the wavelength of the incident light. The restoring force will also cause oscillatory motion of the electrons, similarly to how a mass on a spring behaves, with a characteristic frequency. Suppose the frequency of the incident EM radiation is the same as this characteristic frequency. In that case, it will cause large oscillations in all the conduction electrons, producing electric fields near the particles [49]. The electric fields will act upon the electrons and further reinforce the oscillations [47].

Note that the polarization induced in the surrounding medium stems from the oscillating electrons. The polarization in the medium is in the opposite direction of the electron polarization. This induces a reduction in the restoring force for the electrons and will shift the characteristic frequency into a lower frequency [49].

The properties and the existence of surface plasmons can be described by quantum mechanics or by the dielectric function of the Drude model. However, the dielectric function approach is only adequate for describing the optical response of metals when the photon energies are below the threshold for energy band transitions [44].

2.2.2 Electromagnetism and Metal Interaction

The interaction between metals and EM fields can be explained with a classic approach by using *Maxwell's equations*, even for metallic nanostructures on the order of a few nanometers [44].

Maxwell's equations link four macroscopic fields together. The dielectric displacement $\mathbf{D}$, the magnetic induction $\mathbf{B}$, the electric field $\mathbf{E}$, and the magnetic field $\mathbf{H}$. Maxwell's equations for electromagnetism are as following, where ρ_{ext} and $\mathbf{J_{ext}}$ are the external electric charge and electric current densities, respectively [44][50].

$$\nabla \cdot \mathbf{D} = \rho_{ext} \tag{2.3a}$$

$$\nabla \cdot \mathbf{B} = 0 \tag{2.3b}$$

$$\nabla \times \mathbf{E} = -\frac{\partial \mathbf{B}}{\partial t} \tag{2.3c}$$

$$\nabla \times \mathbf{H} = \mathbf{J_{ext}} + \frac{\partial \mathbf{D}}{\partial t} \tag{2.3d}$$

Equations 2.3 are further linked through the polarization $\mathbf{P}$, and the magnetization $\mathbf{M}$, via Equations 2.4a and 2.4b, where ϵ_0 and μ_0 are the electric permittivity and the magnetic permeability of vacuum, respectively [44][50].

$$\mathbf{D} = \epsilon_0 \mathbf{E} + \mathbf{P} \tag{2.4a}$$

$$\mathbf{H} = \frac{1}{\mu_0}\mathbf{B} - \mathbf{M} \tag{2.4b}$$

With the presence of matter and a media that is isotropic and linear, the EM fields will be modified, and Equations 2.3a and 2.3b take the form of the constitutive relations given in Equations 2.5a and 2.5b. In addition, the external electric current density takes the form of Equation 2.5c, where ϵ_r and μ_r are the relative electric permittivity and magnetic permeability, respectively, and σ is the specific conductivity [42]. The relative permittivity ϵ_r is also called the dielectric constant [44].

$$\mathbf{D} = \epsilon_0 \epsilon_r \mathbf{E} \tag{2.5a}$$

$$\mathbf{B} = \mu_0 \mu_r \mathbf{H} \tag{2.5b}$$

$$\mathbf{J_{ext}} = \sigma \mathbf{E} \tag{2.5c}$$

Note that $\epsilon = \epsilon_0 \epsilon_r$ and $\mu = \mu_0 \mu_r$, where ϵ is referred to as the absolute permittivity, while μ is the permeability of a specific medium. So, Equation 2.5a may be written as the following:

$$\mathbf{D} = \epsilon \mathbf{E} \tag{2.6}$$

In Equation 2.6, the ϵ is written as a constant, implying that the displacement field responds immediately to the applied electric field. However, real materials will have a finite response time. By writing the solutions of Maxwell's equations as superpositions of monochromatic waves, the finite response time can then be taken into account. Equation 2.7 is a modified version of Equation 2.6, which takes the finite response into consideration, where ω is the angular frequency [47].

$$\mathbf{D}(\omega) = \epsilon(\omega)\mathbf{E}(\omega) \tag{2.7}$$

$\epsilon(\omega)$ is now frequency-dependent and complex, as it can be either a real or complex value. Because of the relation $\epsilon = \epsilon_0\epsilon_r$, the dielectric constant is also frequency-dependent. Thus, the dielectric constant is now a complex frequency-dependent function. It will provide a complete description of the optical response of materials in the classical picture. Note that once the dielectric constant is frequency-dependent, it is referred to as the dielectric function instead. To further develop a classical model for metallic nanoparticle plasmonics, a model for the dielectric function of metals is required [47].

2.2.3 The Dielectric Function From The Drude Model

Drude's model (also called the free-electron model) is known as the simplest model for the dielectric response of a metal. In this model, the conduction electrons are modeled as a gas of free, non-interacting electrons [47]. The dielectric function is of great interest for plasmonics as it can describe the optical response of metals. It is also related to determining the size, type, and geometry of the metals that may be applied as plasmonic material to yield the highest energy conversion efficiency [51].

For a free electron gas, the optical properties of metals in a wide frequency range can be described by the *plasma model*, where the free electron gas has a certain density n and is moving against stationary positive atomic cores. The frequency range can be limited depending on the type of metal. The plasma model disregards lattice potential and electron-electron interaction but instead assumes that some of the band structure is incorporated into the effective optical electron mass m [44].

The plasma model states that the applied EM field causes the electrons to oscillate. Their motion is damped due to collisions with a characteristic collision frequency $\gamma = 1/\tau$, where τ is the relaxation time of the free electron gas. The motion of a single electron in the plasma cloud, when subjected to an external electric field, $\boldsymbol{E}$, is given in Equation 2.8, where e is the electric charge [44] and $\mathbf{x}$ is the 1D displacement of the electron relative to the fixed background of atomic cores [47].

$$m\ddot{\mathbf{x}} + m\gamma\dot{\mathbf{x}} = -e\mathbf{E}(t) \tag{2.8}$$

The spatial displacement and any induced field that is affected by an applied oscillatory field with frequency ω will oscillate with the same frequency, such that $\mathbf{E}(t) =$

$\mathbf{E}(\omega)\exp[-i\omega t]$. A particular solution for Equation 2.8 will then be $\mathbf{x}(t) = \mathbf{x}(\omega)\exp[-i\omega t]$. Any phase shift between the driving electric field and response is incorporated into the complex amplitude $\mathbf{x}(\omega)$ through Equation 2.9 [44][50].

$$\mathbf{x}(\omega) = \frac{e}{m(\omega^2 + i\gamma\omega)}\mathbf{E}(t) \tag{2.9}$$

The induced polarization by the displacement of the conduction electrons by a distance $\mathbf{x}$ is given by Equation 2.10, where n is the conduction electron density [47].

$$\mathbf{P}(\omega) = -\frac{ne^2}{m(\omega^2 + i\gamma\omega)}\mathbf{E}(t) \tag{2.10}$$

The displacement function and the polarization are linked by the dielectric function, as shown in Equation 2.4a. The modified displacement function is then linked to the polarization through Equation 2.11, where $\epsilon_0(\omega)$ includes any dielectric response except for the polarization $\boldsymbol{P}$ [44].

$$\mathbf{D}(\omega) = \epsilon(\omega)\epsilon_r(\omega)\mathbf{E}(\omega) \equiv \epsilon_0(\omega)\mathbf{E}(\omega) + \mathbf{P}(\omega) \tag{2.11}$$

Thus, from Equations 2.5a, 2.10, 2.11 and the plasma frequency of the free electron gas $\omega_p = \sqrt{\frac{ne^2}{\epsilon_0 m}}$, the Drude form for the complex dielectric function of a free-electron gas is given in Equation 2.12 [44][47].

$$\epsilon_r(\omega) = 1 - \frac{\omega_p^2}{\omega^2 + i\gamma\omega} \tag{2.12}$$

The real and imaginary parts of the complex dielectric function $\epsilon_r(\omega) = \epsilon_1(\omega) + i\epsilon_2(\omega)$ are given in Equations 2.13a and 2.13b, respectively. The real part describes the stored charge (the ease of which electrons may be polarized) [13], where a negative value indicates that plasmonic phenomena may occur [52]. The imaginary part describes the loss and absorption by the metal [13].

$$\epsilon_1(\omega) = 1 - \frac{\omega_p^2\tau^2}{1 + \omega^2\tau^2} \tag{2.13a}$$

$$\epsilon_2(\omega) = \frac{\omega_p^2\tau}{\omega(1 + \omega^2\tau^2)} \tag{2.13b}$$

As stated previously, the dielectric function and its real and imaginary components can describe the optical response of materials as long as it is defined by classical mechanics [47]. If the medium is a non-magnetic solid, then the dielectric function is related to the complex refractive index for a medium N via Equation 2.14a [53], which will yield Equations 2.14b and 2.14c, where n is the refractive index and k is the extinction coefficient [44].

$$N = \sqrt{\epsilon_r} = n + ik \tag{2.14a}$$

$$\epsilon_1 = n^2 - k^2 \tag{2.14b}$$

$$\epsilon_2 = 2nk \tag{2.14c}$$

In addition, it is useful to study the dielectric function for different frequency regimes concerning the characteristic collision frequency γ [44]. For low frequencies, $\omega < \omega_p$, the Drude model gives a good description of the dielectric response. In this regime, the dielectric function $\epsilon_r < 0$, and the response is metallic with a dominant contribution by the conduction electrons [47].

When the EM frequencies are much lower than the plasma frequency, $\omega \ll \tau^{-1}$ [44], the imaginary component of the dielectric function will become much larger than the real component, $\epsilon_2 \gg \epsilon_1$, which means that n and k become comparable in magnitude, as shown in Equation 2.15. In this very-low-frequency regime, metals are mostly absorbing [44].

$$n \approx k = \sqrt{\frac{\epsilon_2}{2}} = \sqrt{\frac{\tau\omega_p^2}{2\omega}} \tag{2.15}$$

The dielectric function is mostly real at a frequency regime close to the plasma frequency as the damping is negligible, where Equation 2.16 describes the undamped free-electron plasma [44].

$$\epsilon(\omega) = 1 - \frac{\omega_p^2}{\omega^2} \tag{2.16}$$

In the limit of zero damping, $\tau \longrightarrow \infty$, the displacement at the plasmon frequency $\mathbf{x}(\omega = \omega_p)$, is finite for an arbitrary small driving field, corresponding to excitation of the electron gas. The limit of zero damping implies that the imaginary part of the dielectric function is zero. However, the dielectric function must satisfy the Kramers-Kronig relations, which connect the real and imaginary parts of the dielectric function, and which implies that $\epsilon_2(\omega) \neq 0$ [47].

The plasmon response in metal nanoparticles is well-defined for a frequency range above the plasma frequency corresponding to 1-2 eV photon energies. This is due to a small imaginary component. There is a significant increase in the magnitude of the imaginary component at higher frequencies, corresponding to significant damping of plasmon resonances [47], leading to large reflections [44].

As stated previously, some metals have a limited frequency range in which the plasma model can describe them. These metals are noble, and their interband transitions occur in the visible frequency range [44], which will contribute to the dielectric function. Thus, Drude's model cannot quantitatively or qualitatively produce the real dielectric function. Therefore, the model must be expanded to include multiple poles described by different resonance frequencies and decay constants, where the expanded model is referred to as the *Lorentz-Drude model* [47]. However, as long as the metals are not noble, then the dielectric function of the Drude model is adequate for finding the optical response of the metals [47].

2.2.4 Localized Surface Plasmon Response

If a metallic nanoparticle with diameter d is much smaller than the wavelength of the incident light, $d \ll \lambda$, then its interaction with the EM field can be analyzed with an electrostatic approach [44].

Figure 2.13 shows an isotropic and homogeneous sphere of radius a, located at the origin in an uniform electrostatic field $\mathbf{E} = E_0\hat{\mathbf{z}}$. The dielectric response of the sphere is described by the dielectric function $\epsilon(\omega)$, while the surrounding medium, which is isotropic and non-absorbing, is described by the dielectric constant ϵ_m [44].

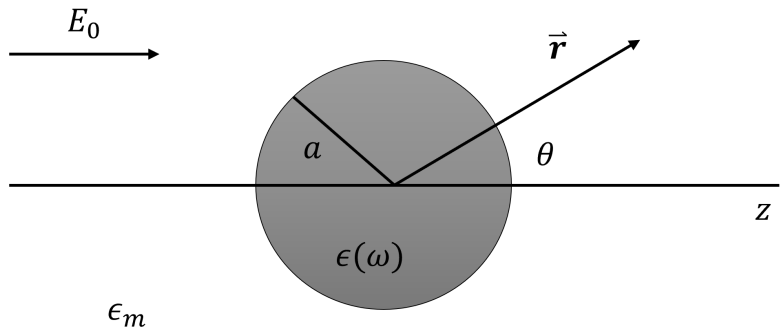

Figure 2.13: Sketch of a sphere located at the origin in an electrostatic field. Redrawn from Maier [44].

$$\Phi(r,\theta) = \sum_{l=0}^{\infty}[A_l r^l + B_l r^{-(l+1)}]P_l(\cos\theta) \tag{2.17}$$

The general solution of the *Laplace equation* of the potential, $\nabla^2\Phi$, is given in Equation 2.17, where $P_l(cos\theta)$ are the Legendre Polynomials of order l, and θ is the angle between position vector $\mathbf{r}$ and the z-axis [44].

The solution of the potentials Φ_{in} and Φ_{out} of the sphere can be written as Equations 2.18a and 2.18b. This is due to the requirement that the potential must be finite at the origin [44].

$$\Phi_{in}(r,\theta) = \sum_{l=0}^{\infty} A_l r^l P_l(\cos\theta) \tag{2.18a}$$

$$\Phi_{out}(r,\theta) = \sum_{l=0}^{\infty}[B_l r^l + C_l r^{-(l+1)}]P_l(\cos\theta) \tag{2.18b}$$

The coefficient B_l may be determined from the boundary condition at $r \longrightarrow \infty$ and results in $B_1 = E_0$ and $B_l = 0$ for $l \neq 1$. The coefficients A_l and C_l may be determined

by the boundary condition at $r = a$, which results in $A_l = C_l = 0$ for $l \neq 1$. The calculation of the remaining coefficients A_1 and C_1 transforms the potentials into Equations 2.19a and 2.19b [44].

$$\Phi_{in} = -\frac{3\epsilon_m}{\epsilon + 2\epsilon_m} E_0 r \cos\theta \tag{2.19a}$$

$$\Phi_{out} = -E_0 r \cos\theta + \frac{\epsilon - \epsilon_m}{\epsilon + 2\epsilon_m} E_0 a^3 \frac{\cos\theta}{r^2} \tag{2.19b}$$

Φ_{out} can be rewritten as Equation 2.20a by introducing the dipole moment $\mathbf{p}$, given in Equation 2.20b [44].

$$\Phi_{out} = -E_0 r \cos\theta + \frac{\mathbf{p} \cdot \mathbf{r}}{4\pi\epsilon_0\epsilon_m r^3} \tag{2.20a}$$

$$\mathbf{p} = 4\pi\epsilon_0\epsilon_m a^3 \frac{\epsilon - \epsilon_m}{\epsilon + 2\epsilon_m} \mathbf{E}_0 \tag{2.20b}$$

If the polarizability α is introduced via $\mathbf{p} = \epsilon_0\epsilon_m\alpha\mathbf{E}_0$, then the complex polarizability of a small sphere with sub-wavelength diameter located in an electrostatic field is given by Equation 2.21 [44].

$$\alpha = 4\pi a^3 \frac{\epsilon - \epsilon_m}{\epsilon + 2\epsilon_m} \tag{2.21}$$

The polarizability will experience a resonant enhancement when $|\epsilon + 2\epsilon_m|$ is a minimum. For the case of a small or slow-varying $\mathrm{Im}[\epsilon]$ around the minimum, Equation 2.21 can be simplified as Equation 2.22, known as the Fröhlich condition [44].

$$Re[\epsilon(\omega)] = -2\epsilon_m \tag{2.22}$$

Equation 2.22 indicates that the resonance frequency is strongly dependent on the surrounding dielectric medium, such that by increasing ϵ_m, the resonance will be red-shifted [44].

2.2.5 Plasmonic Response for Aluminium and Indium Nanostructures

Most work involving plasmonics has worked with nanostructures of gold or silver due to their convenient characteristics. The metals are noble elements with plasmon resonances in the visible spectra region [12]. However, these materials are expensive due to scarcity. Aluminium and indium are the most promising plasmonic metal candidates that could be viable alternatives [13].

In Figure 2.14, the real and imaginary parts of the dielectric function for Al and In are shown, where the data was used from Lumerical's database, which retrieved the data from Palik [54]. Note that the Al had a standard RMS (root-mean-square) error of 1.05668, while the In had an RMS error of 5.47806. As shown in Figure 2.14a,

both Al and In have $\epsilon_1 < 0$, which indicates that plasmon excitation may occur in the selected wavelength range. Figure 2.14b illustrates that In has a less steep increase in the imaginary part with increasing wavelength than the Al. This indicates that the loss in the In metal is less than in the Al metal and that In may be a more effective plasmonic material in the visible region than Al [13].

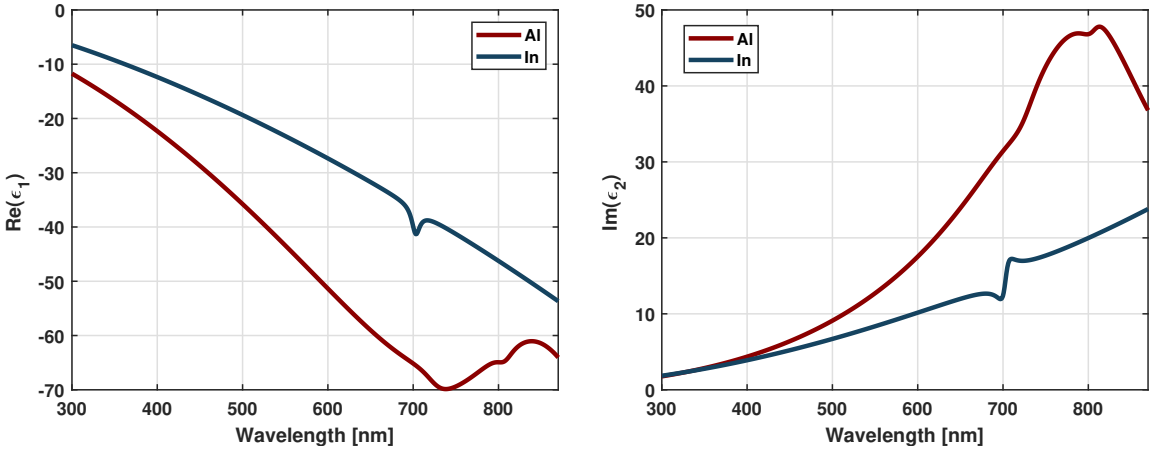

(a) Real component of the dielectric function.

(b) Imaginary component of dielectric function.

Figure 2.14: Dielectric function for aluminium and indium

The plasmonic response of Al has in the recent decade been significantly explored by various groups. The plasma frequency of Al is higher than that of gold and silver, which essentially allows for significant SP response to arise in the ultraviolet part of the spectrum. Another reason is that Al is an abundant element, making it an affordable material for mass production [12].

The plasma frequency of Al, $\omega_p \approx 15$ eV, corresponds to a wavelength of $\lambda \approx 83$ nm, while for gold and silver, their plasma frequency, $\omega_p \approx 8 - 9$ eV, corresponds to a wavelength of $\lambda \approx 140 - 155$ nm. In the Drude model, when considering a simple metal/air interface, SPs are predicted to arise in the frequency range $0 \leq \omega \leq \omega_s$, where $\omega_s = \omega_p/\sqrt{2}$ is referred to as the quasi-static surface plasmon frequency. As indicated by the relatively high ω_p of Al, the frequency range where SPs are allowed will be broader than for gold or silver [12].

The LSP resonance of Al nanostructures depends greatly on the presence of oxide within the material. Figure 2.15 illustrates the effect of an oxidation layer. The LSP resonance of pure Al nanostructures may also be tuned by increasing the diameter of the nanostructure. This induces phase delay across the nanostructure, which leads to broadening and red shifting of the LSP resonance [55].

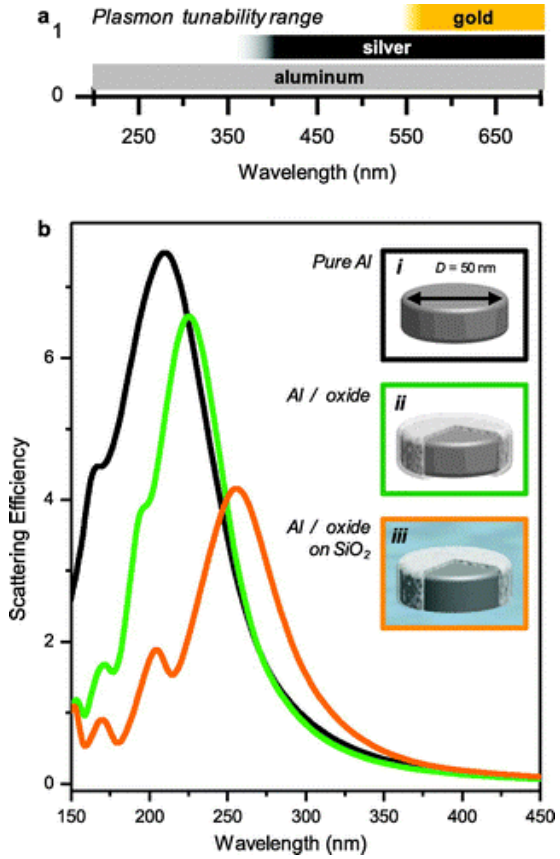

Figure 2.15: (a) Plasmon tuning ranges for gold, silver, and aluminium. (b) The LSP resonance of (i) a pure, isolated Al disk of diameter 50 nm, (ii) the same Al disk but with a 3 nm thick surface oxide and (iii) the Al disk with the oxide layer placed on top of an infinite SiO_2 substrate. Figure taken from Knight et al. [55].

The plasmonic response of In is far less researched than that of Al as both materials have similar qualities, such as LSP resonances arising in the ultraviolet spectral region. In addition, price of indium is significantly higher compared to aluminium, which often leads to In being overlooked in comparison to Al [56].

2.3 Light-Matter Interaction for Solar Cells

When light is incident on and interacts with the interface of two different dielectric materials with different refractive index, see Figure 2.16. Phenomena such as reflection, refraction, and transmission are observed [11].

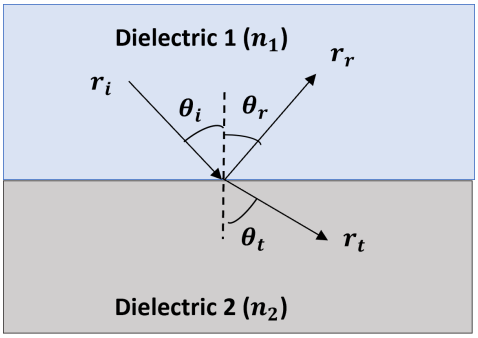

Figure 2.16: General schematic of light reflection, refraction and transmission at an interface between dielectric 1 and 2 with refractive index n_1 and n_2, respectively. Subscripts "i", "r" and "t" stand for incident light, reflected light, and transmitted light, respectively. Redrawn from Solanki et al. [11].

Reflectance refers to the proportion of light reflected back at the interface with respect to the incident light. Absorbance is the term used for the proportion of light that the medium absorbs, and transmittance represents the amount of light that transmits through the medium. These three quantities are at any time and point, related through Equation 2.23, where R is the reflectance, A is the absorbance, and T is the transmittance. The equation states that the sum of the three quantities must be equal to the total amount of incident light [11].

$$R + A + T = 1 \tag{2.23}$$

If the intensity of the incident light with wavelength λ is $I_0(\lambda)$ and the intensity of the transmitted light with wavelength λ is $I(\lambda)$, then per Beer-Lambert's law, the absorption in the absorbing layer can be given by Equation 2.24, where α is the absorption coefficient, and t is the thickness of the absorbing layer [11].

$$A = \frac{I_0 - I}{I_0} = 1 - \frac{I}{I_0} = 1 - \exp\left(-\alpha t\right) \tag{2.24}$$

As can be seen from Equation 2.24 the absorption in the absorbing layer of a solar cell depends on the absorption coefficient and the thickness of the material. Thus, the absorbing layer of a solar cell must have a certain thickness and be a material with high absorption coefficient such that it absorbs most of the available photons in the solar spectrum [11].

From the relation given in Equation 2.23, the absorbance of a solar cell will increase if the path of the photons within the cell increases. In addition, it can be seen that

by reducing reflectance from the cell, the absorption will increase. The reduction of reflection and transmission and the maximization of absorption is the premise of light trapping [11].

Anti-reflection coating (ARC) can be considered as a type of light trapping. The premise here is to coat the solar cell with some thin dielectric material of a certain thickness d and refractive index n, which will reduce the reflection of light from the front surface of the solar cell [11].

The addition of the ARC will cause interference between the reflected rays from the interfaces. Figure 2.17 depicts three dielectric materials with different refractive index. Interference will occur for the radiation rays reflected (r_{12} and r_{23}) from the two interfaces, and depending on the phase difference between the two reflected rays, destructive or constructive interference may occur. This will lead to either high or low reflection [11].

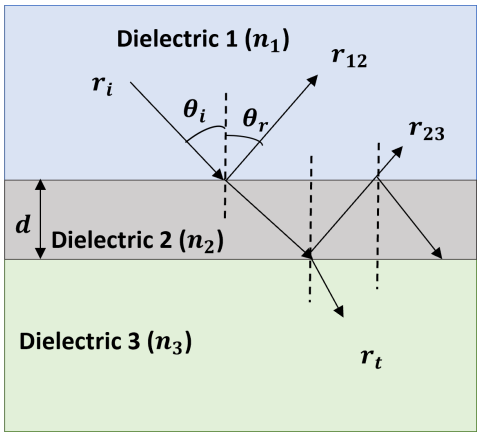

Figure 2.17: General schematic of light reflection, refraction, and transmission at a thin film dielectric with refractive index n_2 introduced at the interface between dielectric 1 and 3 with refractive index n_1 and n_3, respectively. Dielectric 1 is often air or some substrate the thin film is deposited onto. Redrawn from Solanki et al. [11].

The phase difference, $\Delta\phi$, between the reflected rays is related to the path difference between them, as shown in Equation 2.25, where d is the thickness of the thin film, λ is the wavelength of the light, and n is the refractive index of the medium in which the path difference occurs [11].

$$\Delta\phi = \frac{2\pi n}{\lambda} \cdot 2d \tag{2.25}$$

As seen in Figure 2.17, the two reflected rays occur in dielectric 2. They would result in a high reflection from the interface if the wavelength λ has a total phase difference of an even multiple of π, for example, 2π,4π, etc. If the phase difference of the wavelength is an odd multiple of π, such as π, 3π, 5π, etc., then the resultant reflection would be minimal [11].

The phase difference is thus of great importance. It is important to know that when incident light travels from a dielectric medium with a low refractive index to a dielectric medium with a higher refractive index, there will always occur a phase change of magnitude π. However, no phase change occurs if the light travels from a medium with a high refractive index to a medium with a low refractive index [11].

2.3.1 Light-Matter Interaction With Plasmonic Structures

Light-matter interaction such as scattering, absorption and plasmonic effect will occur when EM waves interact with metallic nanoparticles, based on their size, surrounding medium, and shape [57]. Light scattering can be classified into three domains based on a dimensionless quantity called size parameter x [11]. The quantity is defined in Equation 2.26, where a is the particle radius, λ is the wavelength of the incident light, and n_m is the refractive index of the medium [57].

$$x = \frac{2\pi \cdot a \cdot n_m}{\lambda} \tag{2.26}$$

The three domains are categorized based on the following principles [57]:

if $x \ll 1$: Rayleigh scattering (much smaller particle size than the wavelength of light)
if $x \simeq 1$: Mie scattering (particle size comparable to the wavelength of light)
if $x \gg 1$: Geometric scattering (much larger particle size than the wavelength of light)

When very small nanoparticles scatter EM waves, it is called Rayleigh scattering. The typical upper limit for particle diameter when considering Rayleigh scattering is about one-tenth of the wavelength. In this small size region, the exact shape of the scattering center is not important [11].

When the spherical particles have a larger diameter than the Rayleigh range and is approximately equal in size with the incident wavelength, the scattering falls under the Mie scattering domain. In this domain, the shape of the scattering center becomes important as Mie scattering only applies to spherical-shaped nanoparticles. It can also apply to spheroids and ellipsoids but only after certain modifications [58].

Rayleigh and Mie scattering are both elastic scattering types, in which the energy of the EM wave is not significantly changed. The two domains differ in many aspects. Whereas Rayleigh scattering occurs symmetrically, the Mie scattering is asymmetrical, see Figure 2.18. Mie scattering shows a larger amount of scattered light in the forward direction compared to the reverse direction. The bigger the particle size, the more light is scattered in the forward direction [11][59].

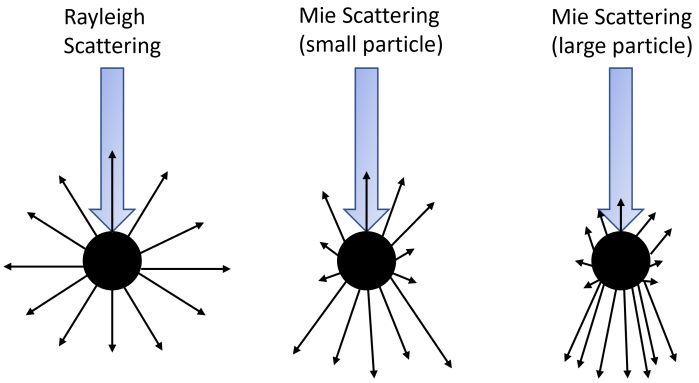

Figure 2.18: Rayleigh scattering occurs symmetrically in all directions. Mie scattering is asymmetrical, with light scattered predominantly forward and backward. For larger particles in Mie scattering, more light will be scattered in the forward direction. Redrawn from Solanki et al. [11]

2.3.2 Light Trapping Based on Plasmonic Nanoparticles

There are at least two ways plasmonic nanoparticles can be used as a light trapping mechanism for solar cells [59]. The first way utilizes metallic nanoparticles as sub-wavelength scattering elements, when placed on the solar cell front surface. These metallic nanoparticles can aid in coupling the freely propagating EM radiation into the active absorbing layer of the solar cell. In this method, multiple and high-angle scattering results in an increased optical path length in the absorbing material [11], see Figure 2.19a.

Another way consists of using the metallic nanoparticles as sub-wavelength antennas, where the plasmonic near-field is coupled to the semiconductor. This will effectively increase the absorption cross-section in the absorbing material near the nanoparticles. The coupled near-field gives rise to more light absorption and a higher creation of electron-hole pairs in the absorbing material [59]. See Figure 2.19b.

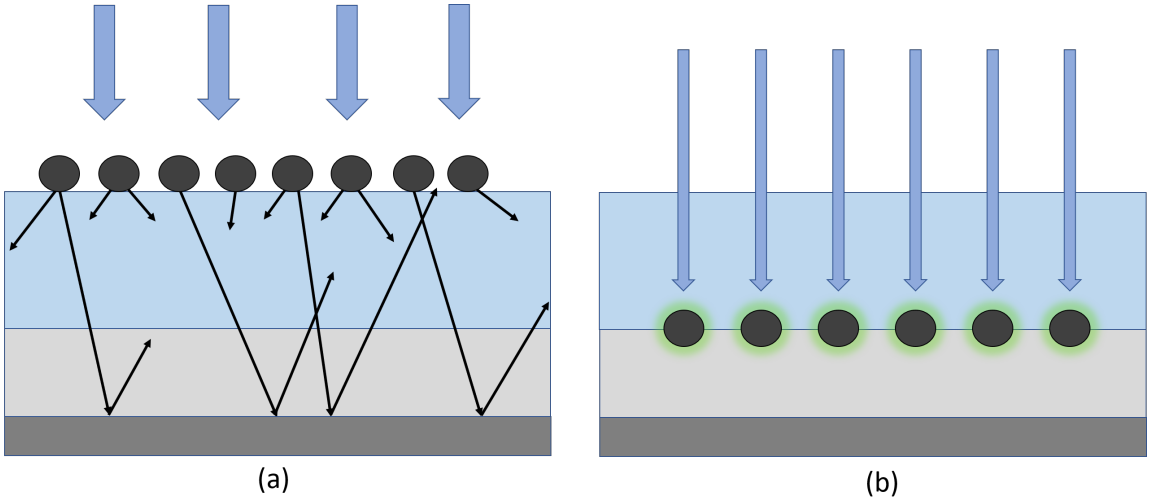

Figure 2.19: (a) Light trapping based on scattering from metallic nanoparticles placed on the solar cell front surface. (b) Light trapping based on the excitation of LSP on metallic nanoparticles embedded in a semiconductor.

2.4 Lumerical

Lumerical is a software with multiple packages. The software package of interest in the thesis is the finite-difference time-domain (FDTD) software package, which can be used to simulate, amongst several things, solar cells.

2.4.1 FDTD

The FDTD method is a computational electromagnetic technique that solves Maxwell's curl equations, given in Equation 2.27, in non-magnetic materials, where H, D, and E are the magnetic, displacement and electric fields. $\epsilon_r(\omega)$ is the complex dielectric function, and ϵ_0 and μ_0 are the electric permittivity and the magnetic permeability of vacuum, respectively [60].

$$\frac{\partial \vec{D}}{\partial t} = \nabla \times \vec{H} \tag{2.27a}$$

$$\vec{D}(\omega) = \epsilon_0 \epsilon_r(\omega) \vec{E}(\omega) \tag{2.27b}$$

$$\frac{\partial \vec{H}}{\partial t} = -\frac{1}{\mu_0} \nabla \times \vec{E} \tag{2.27c}$$

In a 3D environment, the equations will have six EM field components, E_x, E_y, E_z, H_x, H_y and H_z, that can be solved on a discrete spatial and temporal grid. The field components will be solved at different placements within the grid cell. The mesh of the grid cell determines how accurate a calculation is, as fundamental quantities are calculated from each mesh point [60].

The FDTD software package has a simulation region that can be either 2D or 3D based on coordinates *x, y, z*, *x-span, y-span*, and *z-span*, where the *span* parameters describe the length of the axis. There are also options to chose background material, simulation time, and temperature, which allows for in-depth simulations of solar cells [61].

The simulation region supports different types of boundary conditions (BCs), such as perfectly matched layer (PML), metal, perfect magnetic conductor (PMC), periodic and Bloch boundaries. The PML boundaries absorb EM waves incident upon them, meaning they model reflection-less boundaries. These boundaries work best when the simulation structures extend completely through the boundary condition region. The periodic BCs are utilized when both the simulation structure and the EM fields are periodic. Periodic BCs can be used in one or more directions to simulate a structure that is periodic in those directions [61].

The simulation region has a *mesh accuracy setting* that ranges from 1-8, where the default value is 2. This setting determines the number of mesh points in the simulation region, where 1 is the lowest accuracy and 8 is the highest accuracy. For a higher accuracy, more time and computer memory is necessary. It is possible to add a *mesh override region* to the simulation, which will override the mesh accuracy setting of the simulation region with a higher accuracy mesh region of arbitrary size. This will allow accurate simulation of small objects [61].

A *frequency-domain field and power monitor* is a simulation object that can measure the transmission of light as a function of frequency/wavelength, which is a useful tool for measuring the total amount of absorbed light in a simulation object [62].

2.4.2 Convergence Test

There will always be some numerical error associated with numerical simulations. Therefore, it is important to know where these errors may occur and what kind of steps are possible to take in order to make them as small as possible. In the FDTD software package, error reduction often leads to longer simulation time and increased need for computer memory. Therefore, it is important to find a compromise between error and time/memory, so that the simulations do not need significant time/memory to run [63].

In the case of finite difference schemes, such as FDTD, it is often assumed that the error in simulation results will diminish with a decreased grid size. However, more sources of error need to be considered such as proximity of a PML BC to a monitor and the mesh accuracy setting. A convergence test is a mathematical method that investigates whether the partial sums in a series of parameters tend towards a limit. Performing a convergence test on known sources of error may help in reducing the magnitude of the errors [63].

A problem with convergence testing is that there is no way to know the "correct" answer. To understand the convergence, varying an arbitrary parameter in N steps is necessary. Ideally, the N amount of steps is large enough so that the results become linear, which in this case means little variation between the results. This can be quantified by looking at each step of the parameter and defining the difference, σ_s, between the results of the current and the previous step. This gives Equation 2.28 [63].

$$\Delta\sigma_s(i) = \sqrt{\frac{\int(\sigma_i - \sigma_{i-1})^2 d\lambda}{\int(\sigma_i)^2 d\lambda}} \tag{2.28}$$

Ideally, the difference should become 0 such that the source contributes no error. Realistically, σ_s might become linear at some point other than 0, which means that the error of some other source dominates but that the current source also contributes some effect [63].

2.4.3 Quantities to Calculate from FDTD

The total absorbed light in the absorbing layer, P_{abs}, may be found by using two 2D frequency-domain field and power monitors in the z-normal to measure the incident and outgoing light from the layer. The total absorbed light will then be the difference between the monitor measuring incoming light and the monitor measuring the outgoing light, $T_{in} - T_{out}$. Technically, there should also be two monitors measuring the sides of the layer, but most of the light will flow in the z-direction such that the sides can be overlooked [64].

$$QE(\lambda) = \frac{P_{abs}(\lambda)}{P_{in}(\lambda)} \tag{2.29}$$

The quantum efficiency (QE) of the simulated solar cell is defined as Equation 2.29, where $P_{in}(\lambda)$ and $P_{abs}(\lambda)$ are the incident light and the total absorbed light in the solar cell at a wavelength λ, respectively. The integrated quantum efficiency (IQE), or the integrated absorption of the cell [38], is defined as Equation 2.30 [64], where $I_{AM1.5}$ is the AM 1.5G solar irradiance spectrum, c is the speed of light, and h is Planck's constant.

$$IQE = \frac{\int \frac{\lambda}{hc} QE(\lambda) I_{AM1.5}(\lambda) d\lambda}{\int \frac{\lambda}{hc} I_{AM1.5}(\lambda) d\lambda} \tag{2.30}$$

The numerator in the equation is the total amount of photons absorbed by the solar cell, while the denominator is the total amount of photons incident on the solar cell [38][64]. Equation 2.30 can be used to find the minimum thickness of the absorbing layer required to absorb most of the incoming photons [38].

The quantity enhancement factor G is defined as Equation 2.31, which can determine how the efficiency of a solar cell with metallic particles has improved [64], where $G = 1$

means no enhancement, while G $>$ 1 would be a positive enhancement and G $<$ 1 would be a negative enhancement.

$$G = \frac{IQE_{particle}}{IQE_{bare}} \tag{2.31}$$

The $IQE_{particle}$ and IQE_{bare} are the IQE for a solar cell with and without metallic particles, respectively [64].

$$J_{sc} = e \int \frac{\lambda}{hc} QE(\lambda) I_{AM1.5}(\lambda) d\lambda \tag{2.32}$$

Assuming that all electron-hole pairs contribute to the photocurrent, the short circuit current density can be defined as Equation 2.32, where e is the electron charge. For simplicity, the short circuit current density will be referred to as only current density [64].

Chapter 3

Methods

This chapter describes the approach and steps taken in the simulation and experimental parts of the thesis. Firstly, the structure of the simulation objects are outlined. Secondly, the determination and optimization of the thickness of each layer in the solar cells is described. Thirdly, the reduction of error by convergence testing is outlined. Fourthly, the description of the radius and period determination of the nanoparticles is outlined. Thereafter, a brief introduction to the scripts utilized for data processing is given, followed by a description of the reproduction of simulation setups based on existing literature. Lastly, the approach and investigation of depositing aluminium nanoparticles onto Si substrates and Si solar cells are described.

3.1 Thin-Film Solar Cell Simulations

The simulations of the GaAs and CdTe thin-film solar cells were performed using Lumerical's FDTD software package. The general structure of the thin-film simulations can be seen in Figure 3.1. The simulations consisted of a structure-group containing an ARC or TCO (1), a window and absorbing layer, which when combined will be referred to as the junction (2), and a nanoparticle (3). Some simulations only measured the base solar cell, meaning that the nanoparticle was not present. The BCs for the simulation region (4) were periodic in the x, y-direction, as the simulation structure was intended to be periodic in these directions so that an infinite structure occurred. In the z-direction, the BCs was set to PML to have no reflection from these boundaries.

As the efficiency of a solar cell is directly correlated with the amount of absorbed light in the absorbing layer, two frequency-domain field and power monitors were used to measure incoming (5) and outgoing (5*) light from the junction (if the cell was a homojunction), or from the absorbing layer (if the cell was a heterojunction). The amount of light lost due to reflection of the front surface was monitored using a third frequency-domain field and power monitor (6), which was placed behind a plane wave source (7). The plane wave source was located at a distance of half the maximum simulation wavelength from the front surface of the solar cells. For a GaAs solar cell, the plane wave source had wavelength interval from 300 - 870 nm, while for a CdTe solar cell the

wavelength interval was 300 - 850 nm. These interval were chosen based on Figure 2.11.

The monitor indicated by (8) measured the incident light on the ARC/TCO layer, while monitor (9) measured the incident light on the nanoparticle. The monitors were used to measure the absorption of the ARC and the nanoparticle, which was done to determine how much light was lost due to their presence. Note that monitor (9) measured a larger area than what the nanoparticle occupied, which gave a slight increase in the absorption lost due to the nanoparticles. This had to be done, as the calculation for the absorption lost due to the nanoparticle depended on both monitor (8) and (9), which required that they be the same size. However, despite the slight increase in absorption, it gave a good approximation.

The simulation region was placed so that the x, y, z boundaries ended while still located in the junction. Note how in Figure 3.1, the bottom monitor indicated by 5* was not placed at the actual bottom of the simulation region but was placed a distance D away from the PML BC. This was done to minimize the numerical error associated with PML reflection. Therefore, the thickness of the simulated junction was the distance from monitors 5 and 5* and not the whole junction that resides in the simulation region.

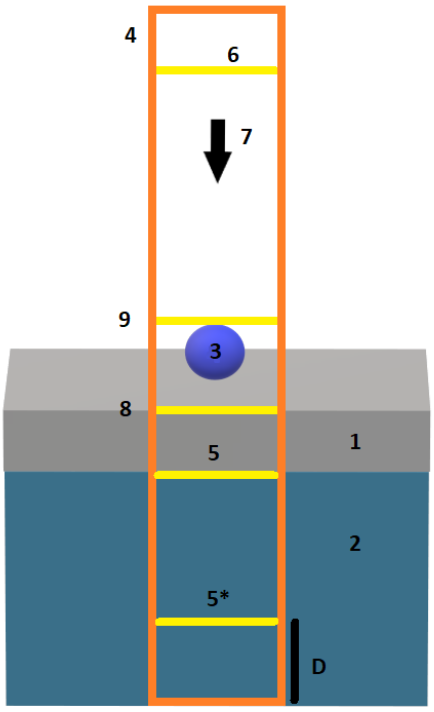

Figure 3.1: The basic setup of the solar cell simulations consisting of an ARC or TCO (1), a junction (of the same material) (2), nanoparticle (3), simulation region (4), a front monitor (5) and bottom monitor (5*), a reflection monitor (6), a plane wave source (7), ARC monitor (8) and nanoparticle monitor (9). The distance between the bottom monitor and z boundary is indicated by (D).

Since the CdTe solar cell is a heterojunction, it has a separate window layer, where Figure 3.2 depicts the general setup for the CdTe cell simulations when the glass substrate was included. The absorption of the cell was measured solely from the CdTe layer, which is the absorbing layer. The loss of absorption due to the CdS layer was also measured. Note that the plane wave source is shown to be inside the glass substrate. The substrate was simulated by setting the background material in the simulation region to SiO_2. Therefore, the source acted as if it was placed inside the glass substrate, which would allow a shorter simulation time without negatively affecting the simulations.

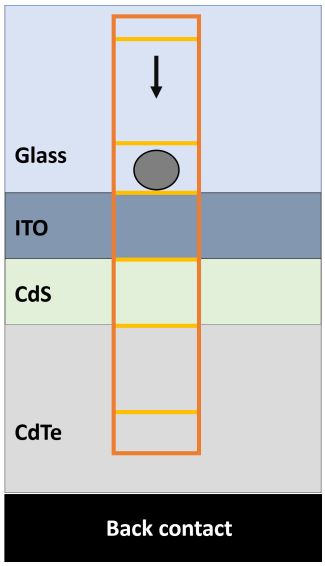

Figure 3.2: The simulation setup for the CdTe solar cell consisting of back contact, CdTe, CdS, ITO, glass, and nanoparticle. Each layer and the nanoparticle, except for the back contact and the glass, had corresponding monitors measuring the amount of absorption.

In order to simulate the solar cells, the refractive index of the materials used in the cells had to be known. The refractive index for CdTe and CdS were obtained in the paper written by Treharne et al. [65]. The data for ITO was retrieved from the paper written by König et al. [66]. Lastly, the data for TiO_2 came from the paper written by Sarkar et al. [67]. The data for the GaAs, Al, In, and SiO_2 came from Lumerical's material database, where Lumerical retrieved the data from Palik [54].

As the main objective in the thesis was enhancing light absorption in the thin-film solar cells, the optimal configuration of the cells had to be determined. The thickness of each layer in the CdTe and GaAs cell were determined through simulations, as described in Section 3.1.1. For the CdTe cell, the background material was set to glass, while the background was set to air for the GaAs cell. Both an optimal and less than optimal thickness of the absorbing layer in the CdTe and GaAs cells were determined. This was performed to investigate the effects of the nanoparticles for different absorbing layer thicknesses.

3.1.1 Determining Layer Thickness of the Films

When setting up the solar cell simulations, the thickness of the absorbing, window and TCO layers had to be evaluated to find which thickness gave the largest absorption in the cell, so that the cell was optimized. As the absorbing layer was of the greatest importance, the thickness of this layer was determined first. The thickness of the GaAs junction was swept from 250 - 2250 nm with 250 nm increments, while the CdTe layer was swept from 500 - 4500 nm with 500 nm increments. The GaAs cell was simulated with air as background material, while the CdTe cell was simulated with glass as background material.

The CdTe cell had a separate window layer consisting of CdS. The CdS layer was deposited onto the CdTe layer after its optimal thickness had been determined and was swept from 10 - 90 nm with 10 nm increments. The optimal thickness of the CdS layer was determined based on the largest integrated absorption measured by the absorbing layer, as the absorbing layer determines the absorption in the solar cell.

Both the GaAs and CdTe cells were simulated with an ITO layer. The thickness of this layer was swept from 10 - 90 nm with 10 nm increments. The ITO layer was deposited onto the junctions once their optimal thickness had been determined. The layer thickness was determined based on the largest integrated absorption measured in the absorbing layer.

To investigate whether the plasmonic nanoparticles could help reduce the thickness of the thin-film cells, a less than optimal thickness for the absorbing layers were chosen based on the results from the respective absorbing layer thickness sweeps.

3.1.2 Minimizing Numerical Error

As stated in Section 2.4.2, there is a numerical error associated with the proximity of the PML BC to the bottom monitor and the mesh accuracy setting. Convergence testing was performed for both optimized thin-film cells to minimize these errors. For the GaAs cell, the testing was performed with background material consisting of air. The testing done for the CdTe cell was performed with both air and glass as background material in separate simulations.

Note that the nanoparticle shown in Figure 3.1 was not present during the testing. The *z-span* was varied in size, where the starting point was a distance of 50 nm from the bottom monitor. The distance, D, increased with 50 nm per subsequent sweep and ended when the distance was 500 nm. The mesh accuracy of the simulation region was varied and tested from the range of 1-8. Both convergence tests calculated Equation 2.28 based on the measured absorption.

Based on the results gained from the convergence testing, the distance and the mesh accuracy with the most optimal values were chosen. The optimal values were determined

by the point where the σ_s became approximately linear. These optimal values were used in further simulations.

3.1.3 Determining Radius and Period of Nanoparticles

Since the main focus of the thesis was investigating the effect of Al and In nanoparticles when used as light trapping mechanisms on optimized GaAs and CdTe cells, the nanoparticles had to be optimized as well. In the search for which radius of the nanoparticles would yield the greatest enhancement, several nanoparticle radius sweeps were performed for different periods, where the period is the distance between the centers of the nanoparticles (see Figure 3.3).

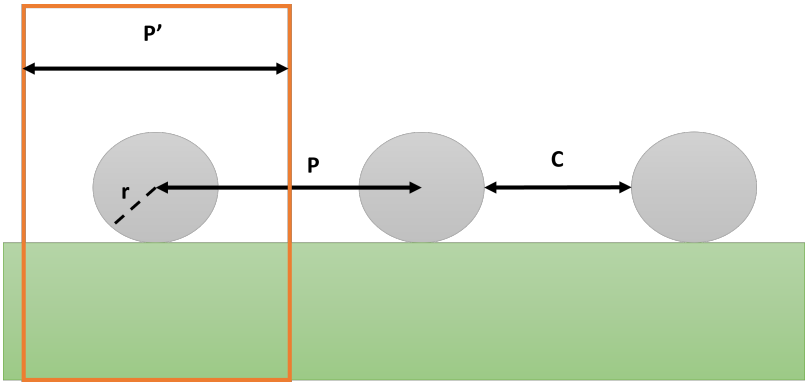

Figure 3.3: The relation between radius and period of nanoparticles. The distance between the centers of the nanoparticles (P) is the period of the nanoparticles. The radius of the nanoparticles determines how close (C) the nanoparticles are placed to one another. The distance (P') is how the period is set up in the simulations.

The radius parameter sweep for both nanoparticles performed for the GaAs cell had a range between 25 - 65 nm with increments of 5 nm. The radius parameter sweep for the CdTe cell had a range between 25 - 75 nm for the Al nanoparticles and 25 - 65 nm for the In nanoparticles, both with increments of 5 nm. Note that all radius parameter sweeps had a starting point of r = 0 nm, meaning no nanoparticles were present in the simulation. This was done due to the ease of calculating the enhancement factor (G) given in Equation 2.31.

The radius parameter sweeps of both the GaAs and CdTe cell were performed for several different period parameters, ranging from 200 nm - 400 nm with 50 nm increments. Thus, each radius sweep was performed five times. Therefore, the total amount of sweeps performed for each solar cell was ten sets, consisting of five sets each for the Al and In nanoparticles, respectively. From each data set obtained from the radius sweeps, the enhancement factor was calculated and plotted as a function of the period. Furthermore, the largest point of the enhancement factor obtained for each radius parameter was plotted versus the period, allowing for an easier determination of the most

suitable period and radius of the optimal nanoparticles.

The steps described above were performed once more for solar cells with less than optimal absorbing layer thickness. In addition, the same steps, except the radius parameter range was 10 - 50 nm with 5 nm increments for both nanoparticles, were performed for an optimized CdTe cell with background material consisting of glass.

Based on the optimal radius and period parameter of the Al and In nanoparticles, the absorption and reflection profiles of the optimized GaAs and CdTe cells were calculated both with and without the nanoparticles present. The current density given in Equation 2.32 was calculated for each of the absorption profiles measured for the respective solar cells.

3.1.4 Data Processing

In order to collect and process the data obtained from the simulations, a basic script in Lumerical's Script File Editor was developed. The script collected the data from the frequency-domain field and power monitors and then calculated quantum efficiency, integrated absorption, enhancement factor, and current density, given in Equations 2.29, 2.30, 2.31, and 2.32. This script was used for all simulations, except for simulations that performed convergence testing, and can be found in Appendix A.

A specific script was made and used for the convergence test simulations. The script was based on and adapted from a script presented at Lumerical's support website [63]. This modified script measured only the absorption of the absorbing layer and calculated Equation 2.28, which is the difference between current and previous measurements and can be found in Appendix B.

3.1.5 Reproduced Setups Based on Configurations from Published Papers

To determine whether the simulation setup used in the thesis was correctly configured, GaAs solar cell simulation setups from Singh et al. [68] and Jangjoy et al. [69] were reproduced. The paper by Singh et al. investigated and optimized Al nanoparticle arrays as a light trapping mechanism for thin-film GaAs solar cells without any ARC's [68]. Jangjoy et al. investigated the combined effect of ARCs and Al nanoparticles as a light trapping mechanism for GaAs thin-film solar cells, where the Al nanoparticles were either placed inside the ARC or on top of the ARC [69]. Some specific results obtained in the papers were compared to the results obtained by the reproduced setups to determine the similarities and differences.

In the paper by Singh et al. [68], the setup had a glass substrate as a back contact and no ARC. The thickness of the GaAs junction was 500 nm, and the glass was 100 nm. The general simulation setup is shown in Figure 3.4. The results of interest in the paper were the absorption profiles.

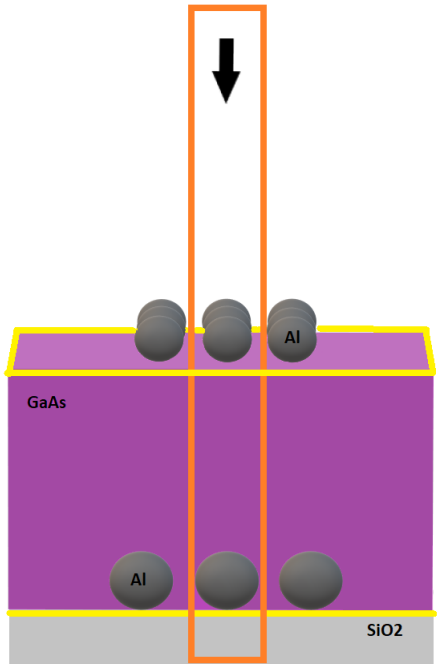

Figure 3.4: The schematic diagram of the thin-film GaAs solar cell with Al nanoparticle arrays at both top and bottom of the junction. Redrawn from Singh et al. [68].

Instead of having a single nanoparticle, as shown in Figure 3.1, the simulation had a 3 x 3 array of Al nanoparticles. The simulations were segmented into four parts, where each part measured the absorption profile of the junction. In the first part, an array of nanoparticles with a radius of 60 nm and a period of 200 nm was placed on the bottom of the junction. The second part consisted of an array with a radius of 45 nm and a period of 150 nm, which was placed on the top of the junction. The third part had both arrays present, and the fourth part had no array present. The four absorption profiles were plotted in one figure to determine whether the array profiles yielded better absorption than the completely bare cell.

The paper by Jangjoy et al. [69] simulated a GaAs solar cell with a thickness of 500 nm and a period of 200 nm. There were three different choices of ARC, which were ITO, SiO_2, and a combination of SiO_2-TiO_2, where the respective thickness of each ARC was 50 nm, 50 nm, and a combined thickness of 50 nm and 35 nm. Figure 3.5 illustrates the setup.

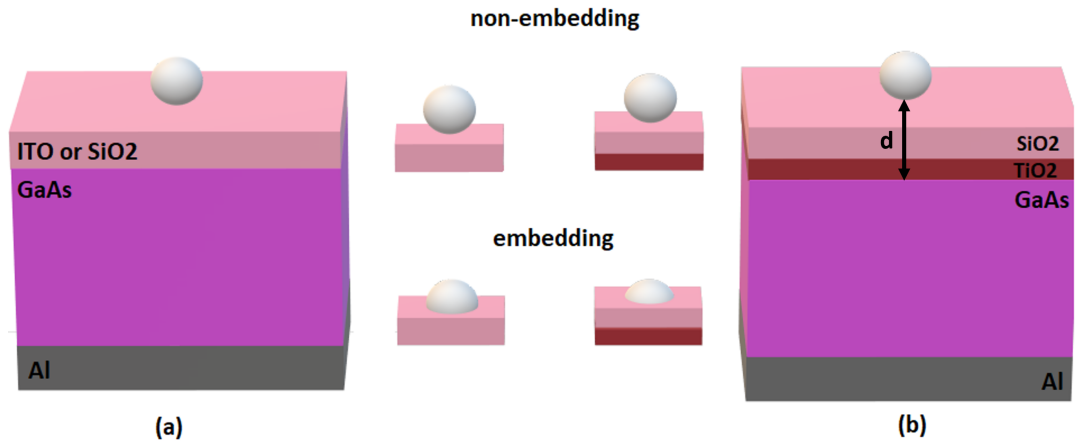

Figure 3.5: The schematic diagram of the GaAs solar cell with (a) ITO or SiO_2 as ARC or (b) SiO_2-TiO_2 as ARC, with the Al nanoparticles either on top of or embedded in the ARC. Redrawn from Jangjoy et al. [69].

The paper investigated the absorption profiles and current density for ITO, SiO_2, and SiO_2-TiO_2 when the Al nanoparticles were on top of or embedded into the respective ARC. In addition, it investigated the absorption profile and current density of the GaAs cell when it was completely bare, meaning it had neither ARC nor Al nanoparticles present. The Al nanoparticles had different radius and distances, d, from the junction depending on which ARC coated the solar cell and whether the nanoparticle was placed on top of or embedded in the ARC. See Table 4.1 for the radius and distance of the Al nanoparticles. The absorption profiles and current densities obtained by Jangjoy et al. were compared to the absorption profiles and current densities obtained by the reproduced setup.

The comparison of a completely bare GaAs cell was only usable if the combination of ARC and Al nanoparticles was of interest. However, if the interest lay with the effects given by only the Al nanoparticles, then it was necessary to compare with the GaAs cell when it had an ARC. Therefore, the absorption profile and current density of a GaAs cell with ITO ARC and no nanoparticles were also investigated in this thesis, so that the effect of only the Al nanoparticles could be determined. The current density was only found for a GaAs cell with either SiO_2 or SiO_2-TiO_2, as that was sufficient for comparison.

3.2 Experimental Work

In simulations, the placement and surface coverage of the nanoparticles are easy to choose. However, the experimental deposition of nanoparticles onto a substrate will not have a predetermined placement. The surface coverage of experimentally deposited Al nanoparticles on a substrate must therefore be investigated.

3.2.1 Deposition of Al Nanoparticles onto Si Substrates

An isopropanol solution containing Al nanoparticles with an approximate size of 100±20 nm was utilized as the source of Al nanoparticles. Six Si substrates of approximate size 1.2 x 1.2 cm^2 were prepared from a Si wafer. The Si substrates will be discussed as substrates 1 through 6. The solution underwent sonication with an *Ultrasound cleaning bath from VWR* [70] at a power setting 9, where sonication is a cleaning process via ultrasound that can separate smaller parts/objects from big clusters.

In order to investigate how the Al nanoparticles settled on the substrates and how to reduce agglomerations, multiple deposition methods were carried out. The Al nanoparticles were deposited onto substrate 1 by dipping and suspending the substrate in the upper part of the solution. At the same time, the solution underwent sonication for a time t $\approx$ 10 min at a temperature of T $\approx$ 30 °C. The substrate was dried by holding it at a relatively steep angle and placing the side of the substrate in contact with an absorbing tissue. This was an efficient way to remove excess solvents from the cell. Substrate 2 underwent deposition via the same method, except the substrate was placed face upwards on the absorbent tissue and dried via evaporation.

The deposition of the nanoparticles onto substrate 3 was carried out using a pipette method. Two droplets were dropped onto the substrate, and it was dried in the same manner as substrate 2. Substrates 4 and 5 were prepared via the same method as substrate 1, except the temperature was T = 60 °C for substrate 4, while substrate 5 was prepared at a temperature T = 70 °C.

The nanoparticle solution underwent a further sonication for approximately 8 hours more, and then substrate 6 was prepared with this solution at a temperature T $\approx$ 50 °C by sonicating for 10 minutes.

The surface morphology of the substrates once deposited with Al nanoparticles was investigated by utilizing scanning electron microscopy (SEM), which is shown in Section 5.1. The surface coverage of Al nanoparticles was found by using the image processing and analysis tool, ImageJ.

3.2.2 Investigation of Si Solar Cells with Al Nanoparticles

Based on the results found when depositing Al nanoparticles on Si substrates, Al nanoparticles were deposited onto two Si solar cells of different sizes, where the larger cell had a surface area of approximately 9 cm^2. In comparison, the smaller cell had a size of approximately 0.75 cm^2. The larger cell was dropped into the solution and left in there while the solution underwent sonication for t $\approx$ 10 min at a T $\approx$ 50 °C. The smaller cell was prepared with the same method as substrate 1 at T $\approx$ 50 °C. Both the cells were dried with the same method as substrate 1, at a steep angle and by touching the side of the cell to a piece of absorbing paper.

The surface morphology of the cells was investigated via SEM. In order to determine how the nanoparticles affected the Si solar cells, the efficiency of the solar cells was measured underneath an AM 1.5G spectrum simulator. The efficiency of the smaller cell post-deposition was compared to the pre-deposition cell.

Chapter 4

Results and Discussion: Simulations

In this chapter, results and discussion based on the simulation part are reported. The first part consist of the comparison based on the results obtained in literature and the reproduced setup. In the second part, the results from the GaAs solar cell simulations are presented and discussed, while the third part presents and discusses the results obtained from the CdTe solar cell simulations. Finally, the results of the GaAs and CdTe cells are compared to one another, and potential problems are discussed.

4.1 GaAs Solar Cell Comparison with Published Papers

The results of the reproduced setup based on the configurations given in the published papers by Singh et al. [68] and Jangjoy et al. [69] are compared to the results obtained by the respective papers.

Reproduced setup based on Singh et al.

The reproduction based on the setup from Singh et al. [68] was used to determine whether the simulation setup could be used for further simulations. The absorption profiles obtained in the paper are shown in Figure 4.1a, while the profiles obtained from the reproduced setup are shown in Figure 4.1b, where NP is the shortening of nanoparticle.

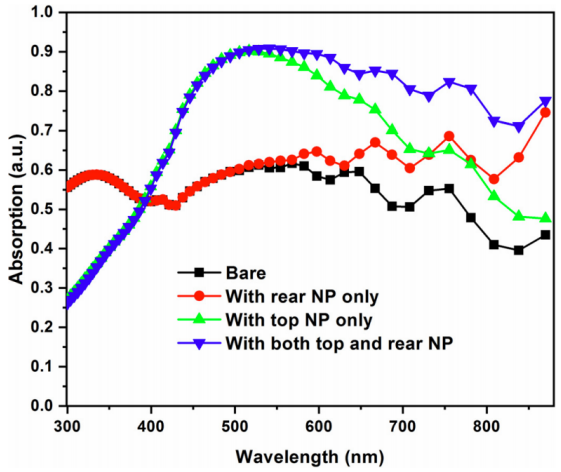

(a) Absorption profiles from Singh et al. [68]

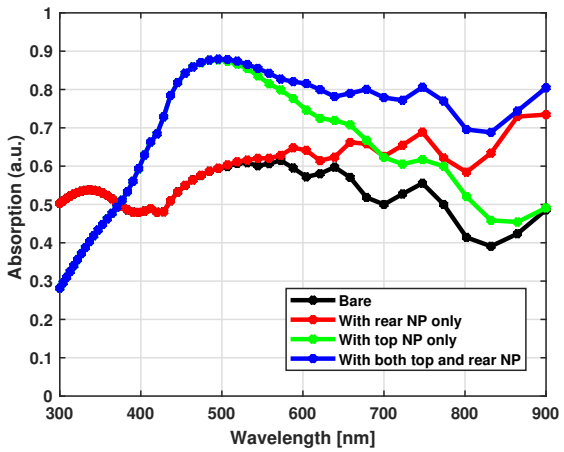

(b) Absorption profiles from reproduced setup

Figure 4.1: The absorption profiles of a GaAs cell of thickness 500 nm, without Al NPs and with Al NPs on top, at the rear, and both at the same time.

As can be seen, there was a great similarity between the two figures. However, some slight differences in the absorption profiles can be seen. For the bare and rear nanoparticle profiles, the absorption in the replication was slightly lower, with a difference of 0.05 in the wavelength region 300 - 400 nm. There was also a slight difference in absorption profiles for the top and the combined nanoparticle profiles, where the absorption profiles from the paper had a slightly larger absorption at wavelength 500 nm compared to the data obtained in the thesis. In addition, the combined nanoparticle profile in the paper had a larger absorption at a wavelength of 600 nm.

Any differences between Figures 4.1a and 4.1b were most likely due to mesh accuracy settings as the reproduced setup used the standard FDTD settings (see Section 2.4.1), which meant that the accuracy of the reproduction simulation was low. In general, there was a good amount of agreement between them. Based on this, it was concluded that the simulation setup was suitable for further studies.

Reproduced setup based on Jangjoy et al.

The paper by Jangjoy et al. [69] investigated for a GaAs solar cell the effects of adding Al nanoparticles to three ARCs at different distances from the absorbing layer. The enhancement gained by the Al nanoparticles and ARC combo was then compared to a completely bare GaAs without any ARC. When the nanoparticles were placed on top of the ARC, they will be referred to as *NPs on*, while if the nanoparticles were embedded in the ARC, they will be referred to as *NPs in*.

The absorption profile from Jangjoy et al. [69] of a bare GaAs cell is shown in Figure 4.2a. In addition, the absorption profiles of a cell with Al NPs on and NPs in ITO are shown in the figure. The absorption profiles from the reproduced setup are shown in Figure 4.2b. Note that the bare cell in these figures represents a GaAs cell without

ARC or nanoparticle. In Jangjoy et al., the absorption profiles of the nanoparticles show an oscillating behavior starting from wavelength 500 nm. It was not discussed in the paper why this happened, but it was found in this thesis that it was due to thin film interference, see Section 2.3, from the back metal contact, which was included in the simulation region of Jangjoy.

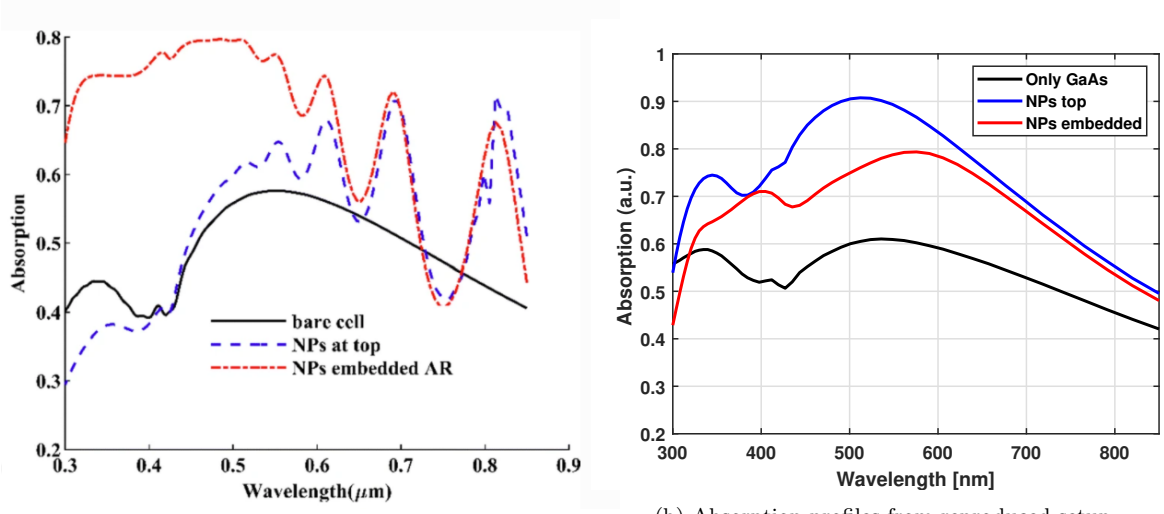

(a) Profiles from Jangjoy et al. [69]

(b) Absorption profiles from reproduced setup.

Figure 4.2: The absorption profiles of a GaAs cell with ITO. The black function was the absorption obtained for a cell with no ARC and no Al NP, the blue function was the absorption obtained for a cell with Al NPs on ITO, and the red function was the absorption obtained for a cell with Al NPs in ITO.

The absorption profile of the bare GaAs cell obtained by the reproduced setup (see Figure 4.2b) indicated a much higher absorption in the 300 - 450 nm wavelength region compared to the paper. Another difference between the figures was the shape of the two profiles for the cell with the added Al nanoparticles. The two profiles obtained in the reproduced setup were different from their counterparts in the paper. However, if the oscillations in the profiles from the paper are disregarded, then the difference becomes less dramatic. In addition to the difference in shape, the magnitude of the two profiles was different. In the paper, the absorption profile for the NPs in ITO was larger than that of the profile for the NPs on ITO, while in the reproduction, this was the reverse. In general, the reproduced setup gave absorption profiles with a larger amount of absorption. Due to all these reasons, it is reasonable to assume that the data for ITO used in the reproduced setup was different from the data the paper utilized.

As stated in Section 3.1.5, if the purpose was to investigate the enhancement in absorption due to the Al nanoparticles, then it is necessary to compare the absorption profiles of the Al nanoparticles versus the absorption profile of a GaAs cell with only the ARC present.

Figure 4.3 shows the absorption profiles for a GaAs cell when it was coated in ITO and when there were Al NPs on, and Al NPs in the ITO. As shown in the figure, the absorption for the ITO ARC without any nanoparticles was better compared to the absorption from the combination of ITO and nanoparticles in the wavelength region 350 - 520 nm.

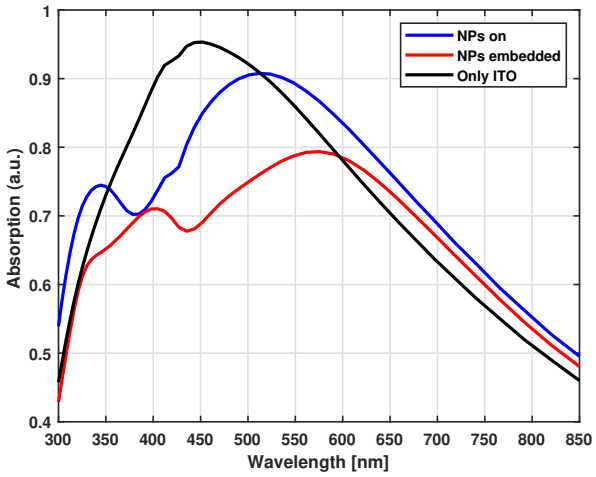

Figure 4.3: The absorption profiles obtained for GaAs cell with ITO. The black function was the absorption obtained from a cell with only ITO, the blue function was the absorption obtained from a cell with Al NPs on ITO, and the red function was the absorption obtained from a cell with Al NPs in ITO.

Furthermore, by comparing Figures 4.2b and 4.3, it becomes clear that most of the increased absorption for the nanoparticle profiles indicated in Figure 4.2b is almost entirely due to the ITO ARC. As will be shown in Table 4.1, the addition of the Al NPs on ITO gave an enhancement of 2% to the current density, while NPs in ITO made the current density drop by 6%. So, the significant increase in absorption for the nanoparticle profiles shown in Figure 4.2b was mostly due to the ITO ARC rather than the Al nanoparticles.

For the second ARC consisting of SiO_2, Figures 4.4a and 4.4b show the absorption profiles obtained when the solar cell had no ARC and SiO_2 with Al nanoparticles. Figure 4.4a was obtained in the paper, and Figure 4.4b was obtained from the reproduced setup. The respective nanoparticle profiles are shown to have a similar shape as long as the oscillations in the wavelength region 500 - 850 nm are disregarded from Figure 4.4a. In the wavelength region of 300 - 400 nm, the absorption profiles for the cell with the Al NPs in SiO_2 obtained by Jangjoy et al. had a larger magnitude compared to the absorption profiles obtained by the reproduced setup.

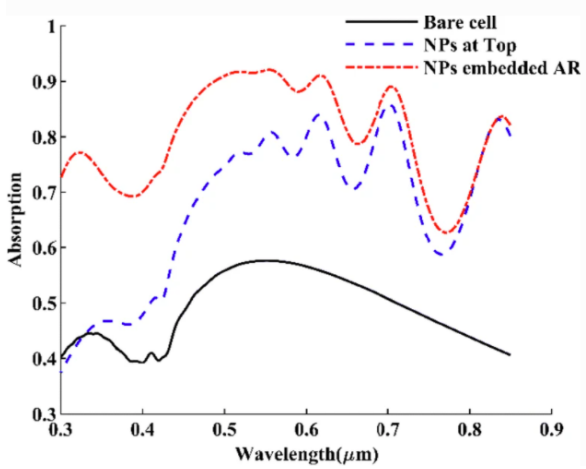

(a) Absorption profiles found for GaAs cell coated with SiO_2, taken from Jangjoy et al. [69]

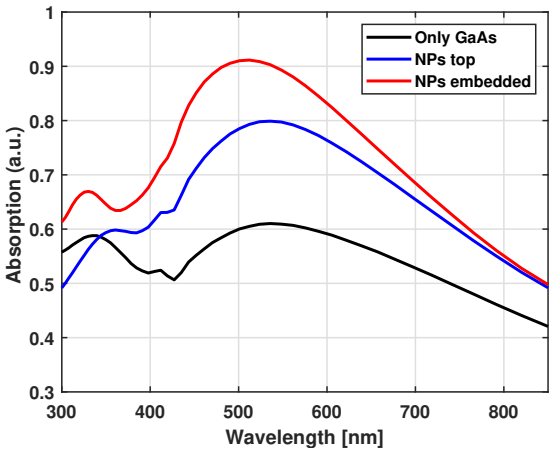

(b) Absorption profiles from reproduced setup found for GaAs cell coated with SiO_2.

Figure 4.4: The absorption profiles obtained for the cell with SiO_2. The black function was the absorption obtained for a cell with no ARC and no Al NP, the blue function was the absorption obtained for a cell with Al NPs on SiO_2, and the red function was the absorption obtained for a cell with Al NPS in SiO_2.

For the third ARC consisting of SiO_2-TiO_2, the absorption profiles are shown in Figures 4.5a and 4.5b, where the former was obtained by the Jangjoy et al. and the latter from the reproduced setup. Note that the figures have slightly different scalebars, due to the larger absorption in Figure 4.5b. The respective profiles are shown to have a mostly similar form as long as the oscillations in Figure 4.5a are disregarded. The magnitude of the absorption profile for the Al NPs on SiO_2-TiO_2 obtained by the reproduced setup was larger in the wavelength region 300 - 600 nm, compared to the absorption profile obtained by the Jangjoy et al. In addition, the absorption profile from the reproduced setup for the Al NPs on SiO_2-TiO_2 had larger values than the profile for the Al NPs in SiO_2-TiO_2. This is the opposite of what was found in the paper. The largest difference between the results from the paper and the reproduced setup was the absorption in the 300 - 450 nm wavelength region. As can be seen, the two absorption profiles for the Al nanoparticles obtained by the reproduced setup both had a dip occur at wavelength 425 nm, whereas the paper had a smooth curve at this point. The dip was likely due to the Al nanoparticles giving an enhancement in the absorption in the wavelength region 350 - 400 nm. The difference between the absorption profiles shown in Figures 4.5a and 4.5b was likely due to the TiO_2 material being different.

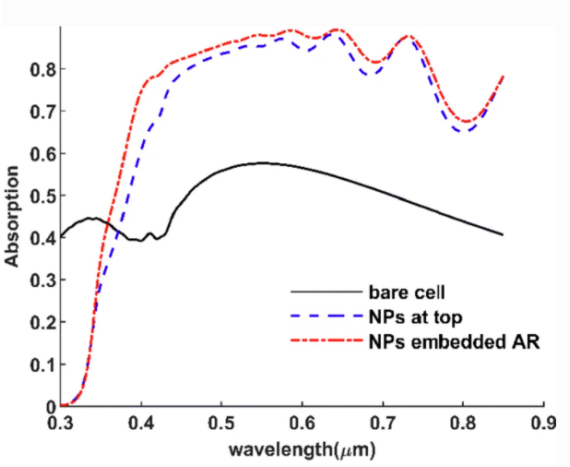

(a) Absorption profiles found for GaAs cell coated with SiO_2-TiO_2, taken from Jangjoy et al. [69]

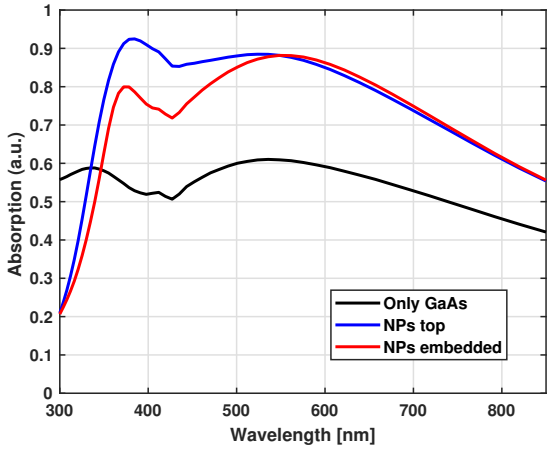

(b) Absorption profiles from reproduced setup found for GaAs cell coated with SiO_2-TiO_2

Figure 4.5: The absorption profiles obtained for the cell with SiO_2-TiO_2. The black function was the absorption obtained for a cell with no ARC and no Al NP, the blue function was the absorption obtained for a cell with Al NPs on SiO_2-TiO_2, and the red function was the absorption obtained for a cell with Al NPs in SiO_2-TiO_2.

Table 4.1: The optimal radius, r [nm], and distance from the top of the absorbing layer, d [nm], and the measured current density, J_{sc} [mA/cm^2], for each ARC and Al nanoparticles placement are indicated. The current density obtained by Jangjoy et al. [69] and the reproduced setup is given in separate columns.

GaAs cell	**ARC**	**r**	**d**	**J_{sc} Jangjoy**	**J_{sc} Thesis**
Bare GaAs	-	-	-	15.37	16.49
Only ARC	ITO	-	-	-	22.04
NPs on ARC	ITO	40	90	17.25	22.55
NPs in ARC	ITO	50	50	20.18	20.74
Only ARC	SiO_2	-	-	-	19.76
NPs on ARC	SiO_2	40	90	21.94	20.54
NPs in ARC	SiO_2	45	50	24.98	22.39
Only ARC	SiO_2-TiO_2	-	-	-	23.99
NPs on ARC	SiO_2-TiO_2	40	125	23.79	23.58
NPs in ARC	SiO_2-TiO_2	40	105	24.68	23.17

The data based on the absorption profiles shown in the figures above is given in Table 4.1. The table indicates the optimal radius and distance of the Al nanoparticles from the front surface of the absorbing layer for each ARC with the corresponding calculated current density obtained with these parameters. The table also shows the current density when only the respective ARCs were coated on the GaAs cell with no nanoparticles present, where only the thesis considered this configuration. This result is important as it is mainly the ARC that contributes to the increase in current density. It will be left to speculation as for why this was not included in the original paper.

There are multiple noticeable discrepancies between the calculated current densities. Firstly, the difference in the current density for a completely bare GaAs cell, where the data obtained in the reproduced setup had a 7% larger value for the current density compared to the data from the paper. Such a large difference signifies that the Jangjoy et al. setup and the reproduced setup did not completely correspond. This means that there could have been a recurring error in the ARC measurements solely due to this base material increase. If this difference was solely due to the mesh accuracy setting, there would not have been such a significant difference. However, this is under the assumption that the paper used the data for GaAs provided by Lumerical's database and did not find another source. If the paper used data found from another source, it could explain why there was such a noticeable difference.

When comparing the data for the GaAs cell coated with an ITO as ARC, the difference between the work in this thesis and the data of Jangjoy et al. is shown to be significant. The magnitude of the difference between the NPs on ITO current density was slightly above 5 mA/cm^2, meaning that the data from the thesis had a 30% larger current density compared to that of the paper. For the NPs in ITO calculations, the current density was 2% larger than the value obtained by Jangjoy et al. Note that the paper showed a further increase in current density when the nanoparticles were embedded rather than placed on top of the ITO. In contrast, the data obtained for the NPs in ITO from the reproduced setup had an 8% lower current density than the NPs on ITO and a 6% lower current density compared to the "Only ITO". The discrepancy for the ITO measurements was extreme. The most probable reason was the choice of ITO data since Lumerical does not have ITO in its material database. The reproduced setup used data extracted from König et al. [66], but the paper did not state what data they utilized. Therefore, it was not possible to verify if this was the main reason for the discrepancy in the two results.

The data obtained for the SiO_2 ARC by the reproduced setup also showed a slight deviation from the paper. The difference was not of the same magnitude as that of ITO, but it was still a noticeable deviation. The reproduced setup obtained a lower current density for both Al nanoparticle placement in comparison to the paper. For the Al NPs on SiO_2, the paper had a 6% larger current density than the one obtained by the reproduced setup. For the Al NPs in SiO_2, the paper had an 11% larger current density than the reproduced setup. The paper obtained an increase of 62% when considering

NPs in SiO_2 versus the completely bare solar cell, while the data from the reproduced setup increased by 35% for the same condition. Thus, the paper had almost two-fold increase in current density compared to the data from the reproduced setup.

The data obtained for the SiO_2-TiO_2 ARC shows that the deviation in current density was low for the Al NPs on SiO_2-TiO_2 when comparing the paper and the reproduced setup, where the difference was only 1%. However, the current densities for the NPs in SiO_2-TiO_2 deviated from one another with a difference of 6%. In addition, the current density obtained in the paper for the NPs in SiO_2-TiO_2 showed a larger value compared to the NPs on SiO_2-TiO_2. In contrast, the reproduced setup obtained a decrease in current density for the same situation. Note that the results from the reproduced setup indicate that the current density for both Al nanoparticle placement was worse than the current density measured for a cell with only the SiO_2-TiO_2 ARC. Thus, the presence of the Al nanoparticles contributed a negative effect on the absorption of the solar cell. The paper did not measure the current density for a cell with only the ARC present, so it is not possible to compare the result obtained by the reproduced setup with the paper.

Based on all the deviations between the paper and the work from the thesis, it can be concluded that there was not enough information to fully reproduce this part of the work of Jangjoy et al. It can be concluded that the choice of material data has great importance and that different material data sets can lead to large deviations in absorption profiles and current density. Despite the difference between the data from the paper and the thesis, interesting results were obtained in the thesis. Table 4.1 indicates that despite most of the increase in current density stemming from the ARCs, the Al nanoparticles contributed a non-trivial increase. The Al nanoparticles placed on top of the ITO gave a 2% increase in current density, while Al nanoparticles on and embedded in SiO_2 gave an increase of 4% and 13%, respectively. Based on these results, it can be concluded that for the specific GaAs solar cell configuration given in Section 3.1.5 with ITO or SiO_2 as ARC, that Al nanoparticles are an excellent light trapping mechanism.

4.2 Investigating GaAs Solar Cell with ITO and Nanoparticles

This section contains the results and discussion based on simulating a GaAs cell with ITO and the addition of Al or In nanoparticles to its front surface. The section presents the results obtained in the thickness sweep of the various thin films in the cell, convergence test for simulations, and the radius and period sweeps of the nanoparticles used for enhancing the light in-coupling. Based on the optimal values from the sweeps, the absorption and reflection profiles of an optimized cell are presented.

4.2.1 Layer Thickness of GaAs Solar Cell

The results of the GaAs layer thickness sweep can be seen in Figure 4.6a. When the layer increased in thickness, the integrated absorption also increased. The increase in integrated absorption was large for each thickness increment below 1000 nm. The increase per increment gradually stabilized for a thickness above 1000 nm until the integrated absorption became approximately stable at 1500 nm and a further increase in thickness gave minute improvements. Based on this, a thickness of 1500 nm was selected as the optimal absorbing layer thickness.

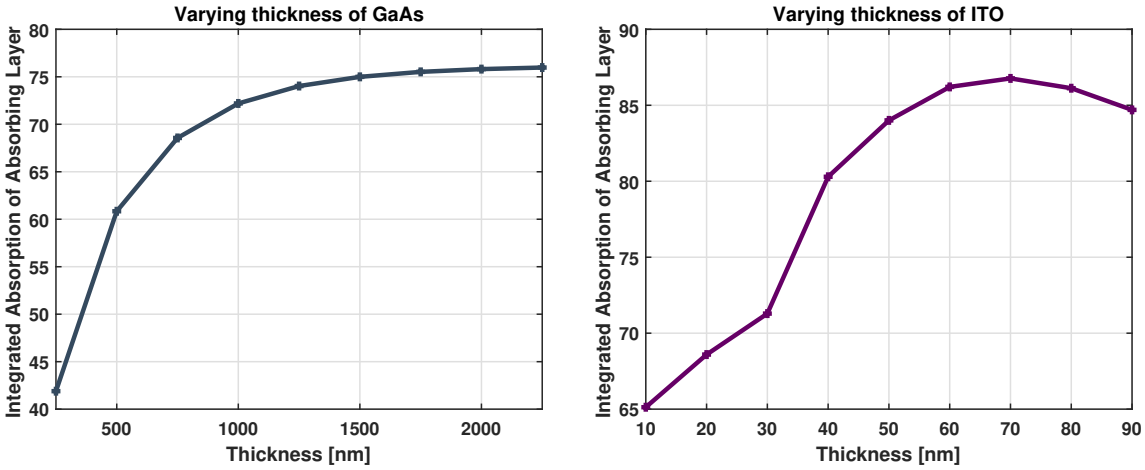

(a) GaAs layer thickness sweep for GaAs solar cell from 250 - 2250 nm.

(b) ITO layer thickness sweep for GaAs solar cell from 10 - 90 nm.

Figure 4.6: Integrated absorption in absorbing layer as a function of thickness for GaAs and ITO.

The thickness sweep of the ITO layer when placed on a 1500 nm thick GaAs layer can be seen in Figure 4.6b. For an ITO layer of thickness 30 nm and below, the integrated absorption in the cell saw a reduction in the absorption compared to when only the GaAs layer was measured. From a 40 nm thickness and above, the addition of the ITO layer resulted in a significant enhancement to the absorption, where the peak enhancement was for a thickness of 70 nm. When the thickness increased beyond 70 nm, the integrated absorption started to drop. This drop in absorption is most likely

due to an increase of absorption in the ITO layer itself. The optimal thickness of ITO was chosen to be 70 nm and would be used in the rest of the GaAs solar cell simulations.

Based on the results obtained, an optimized GaAs solar cell had an absorbing layer thickness of 1500 nm and ITO thickness of 70 nm. For a less than optimal thickness of the absorbing layer, a thickness of 500 nm was determined to be appropriate for comparison.

4.2.2 Convergence Test of GaAs Solar Cell

Based on the results from the subsection above, convergence testing was performed for an optimized GaAs solar cell, where the result of the convergence test for the distance between the PML boundary and the bottom monitor is shown in Figure 4.7a. As depicted, the calculated difference between current and previous absorption measurements, σ_s, was approximately linear for most data points. However, at distance 250 nm and distance 500 nm, relatively large differences between current and previous absorption measurements appear. The appearance of these peaks implies that the proximity between the bottom monitor and the lower PML boundary may have been a source of error. However, the magnitude of the difference between the current and previous measurements was low, so the difference was small. Therefore, σ_s could be considered approximately linear despite the two peaks. Based on this and the values shown in Figure 4.7a, a distance of 300 nm, with associated error of 0.04%, between the bottom monitor and the lower z-boundary of the simulation region was determined to be appropriate.

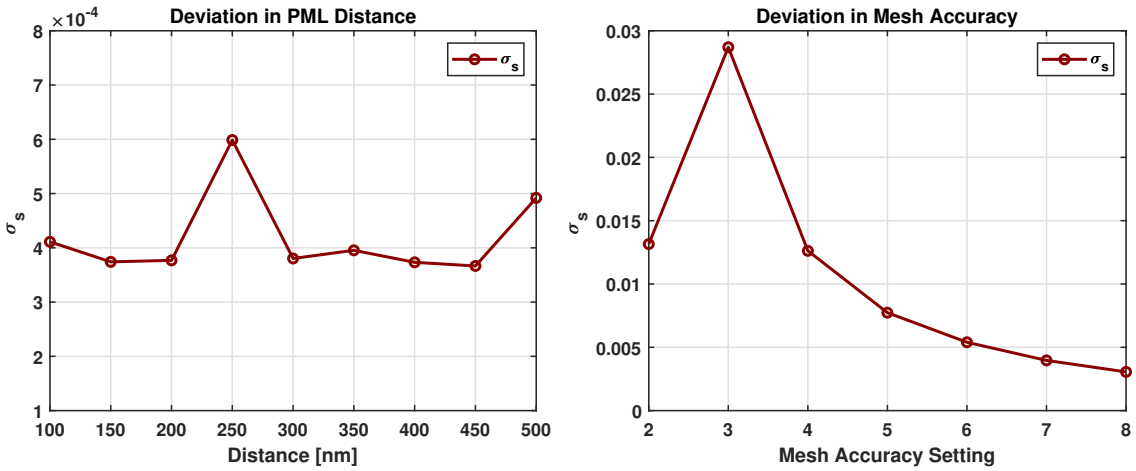

(a) PML distance convergence test.

(b) Mesh accuracy setting convergence test

Figure 4.7: Convergence test for GaAs cell. (a) σ_s shown as a function of the distance between the bottom monitor and lower z boundary. (b) σ_s shown as a function of the mesh accuracy setting.

The result of the convergence test for the mesh accuracy setting is shown in Figure 4.7b, where the difference between current and previous measured absorption is depicted as a function of the mesh accuracy setting. As can be seen, the σ_s was large for low

mesh accuracy setting values, and the mesh accuracy setting could be considered a source of error at this point. The difference function starts gradually stabilizing and becoming roughly linear around setting value 5. Therefore, mesh accuracy setting 5 was determined to be a reasonable choice for further simulations, as it had a low associated error of 0.8% and would not increase simulation time significantly, see Section 2.4.1.

4.2.3 Nanoparticle Radius and Period for GaAs Solar Cell

The radius and period sweep of the nanoparticles were performed on the optimized GaAs solar cell with the mesh accuracy setting and the distance between the bottom monitor and the PML boundary found in the previous subsection.

The results of the radius sweeps of the Al nanoparticles for an optimized GaAs cell can be seen in Figure 4.8a, where it shows the enhancement factor of each radius parameter as a function of the period. The figure indicates that for larger radius parameters at low periods, the enhancement was negative. For larger periods, the enhancement functions would gradually stabilize towards no enhancement. This indicates that the nanoparticles cannot cover a large part of the front surface as the cell will suffer a loss of absorption.

The largest point of each enhancement function is plotted versus the period in Figure 4.8b. The corresponding data are given in Table 4.2. As can be seen in both the figure and the table, the radius and period of the Al nanoparticles that gave the largest enhancement were 45 nm and 300 nm, respectively. The largest enhancement gained from adding the nanoparticles to the front surface of the cell was an increase in absorption of 0.75%.

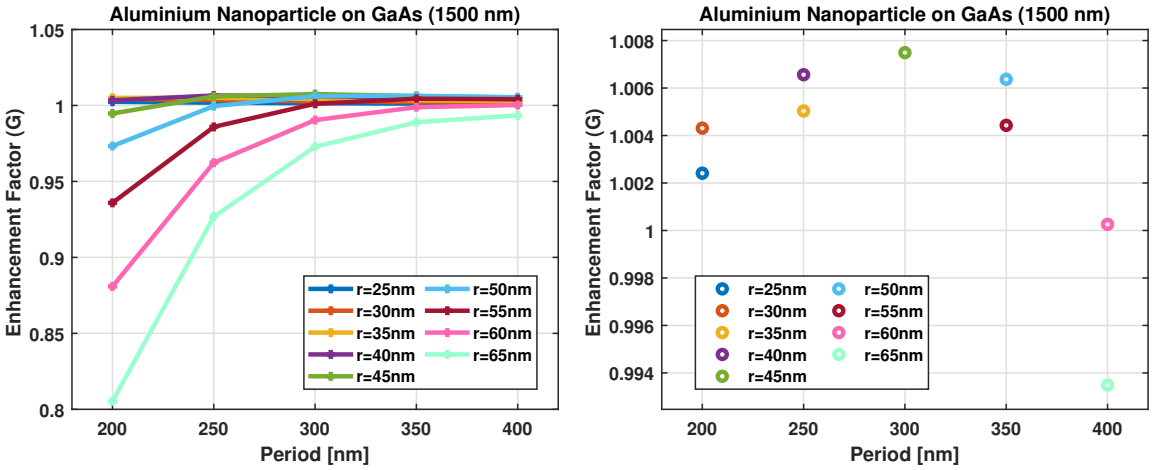

(a) Enhancement factor as a function of period for each Al radius parameter.

(b) Largest enhancement factor vs period for each Al radius parameter.

Figure 4.8: Enhancement factor calculated from a GaAs cell with absorbing layer thickness 1500 nm and Al NPs with radius parameter ranging from 25 - 65 nm.

Table 4.2: Largest enhancement factor calculated for each Al radius parameter at its corresponding period for the GaAs solar cell with absorbing layer thickness of 1500 nm.

Radius [nm]	Period [nm]	Enhancement Factor
25	200	1.0024
30	200	1.0043
35	250	1.0050
40	250	1.0066
45	300	1.0075
50	350	1.0064
55	350	1.0044
60	400	1.0003
65	400	0.9935

The results of the In nanoparticles radius sweeps are shown in Figure 4.9a. The enhancement factor of each radius is a function of the period. As can be seen, the enhancement functions behave similarly to the enhancement functions found for the Al nanoparticles.

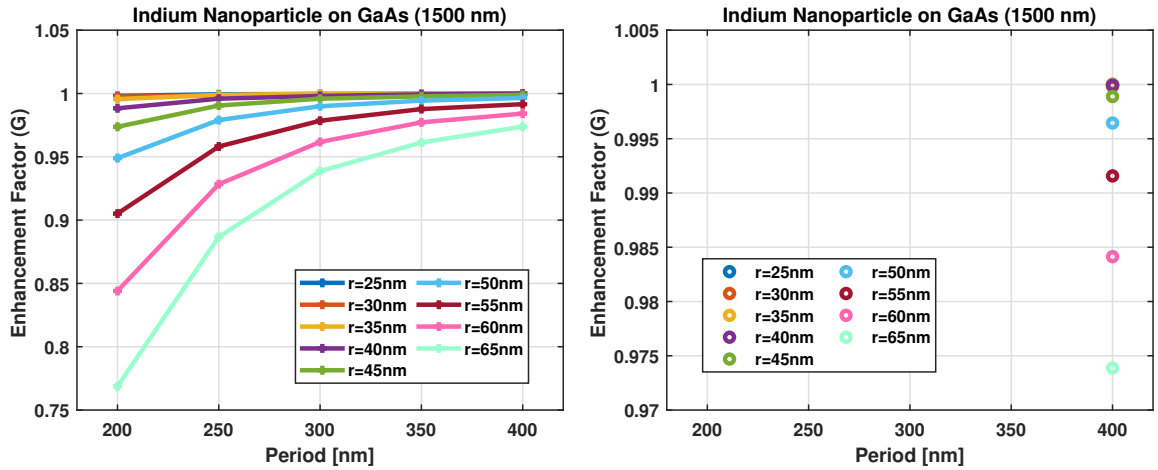

(a) Enhancement factor as a function of period for each In radius parameter.

(b) Largest enhancement factor vs period for each In radius parameter.

Figure 4.9: Enhancement factor calculated from a GaAs cell with absorbing layer thickness 1500 nm and In NPs with radius parameter ranging from 25 - 65 nm.

The largest enhancement obtained from each radius parameter is given versus the period in Figure 4.9b, where the corresponding data is given in Table 4.3. As can be seen, the In nanoparticles did not give any positive enhancement to the absorption for the investigated radius and period parameters. Every radius parameter had its largest

enhancement at a period of 400 nm, implying that a lowered number of In nanoparticles per area gave the largest amount of absorption. Note that in addition to the period of 400 nm, the four smallest radius parameters gave an enhancement of ≈ 1, which indicates that they stabilized towards no enhancement.

Table 4.3: Largest enhancement factor obtained for each indium radius parameter at its corresponding period for the GaAs solar cell with absorbing layer thickness of 1500 nm.

Radius [nm]	**Period [nm]**	**Enhancement Factor**
25	400	1.0000
30	400	0.9998
35	400	1.0000
40	400	0.9999
45	400	0.9989
50	400	0.9964
55	400	0.9916
60	400	0.9841
65	400	0.9739

To investigate the effect of the In nanoparticles and the reason for the non-positive enhancement, Figure 4.10 depicts the absorption and reflection profile of a GaAs cell without nanoparticles, and with In nanoparticles of radius 45 nm and with radius 65 nm, both with a period of 300 nm. As can be seen, the addition of 45 nm In nanoparticles increased the integrated absorption for the wavelength regions 325 - 450 nm and 650 - 870 nm. However, as can be seen, there was a significant amount of loss in the wavelength region 450 - 650 nm, which led to an overall loss of integrated absorption in the cell. The addition of the In nanoparticles led to a red shift in the absorption and reflection profiles. However, the shift occurred in such a way that more light was reflected away from the absorbing layer. Based on these results, In nanoparticles would not be suitable to be a plasmonic scattering mechanism for a GaAs cell with ITO and optimal absorbing layer thickness.

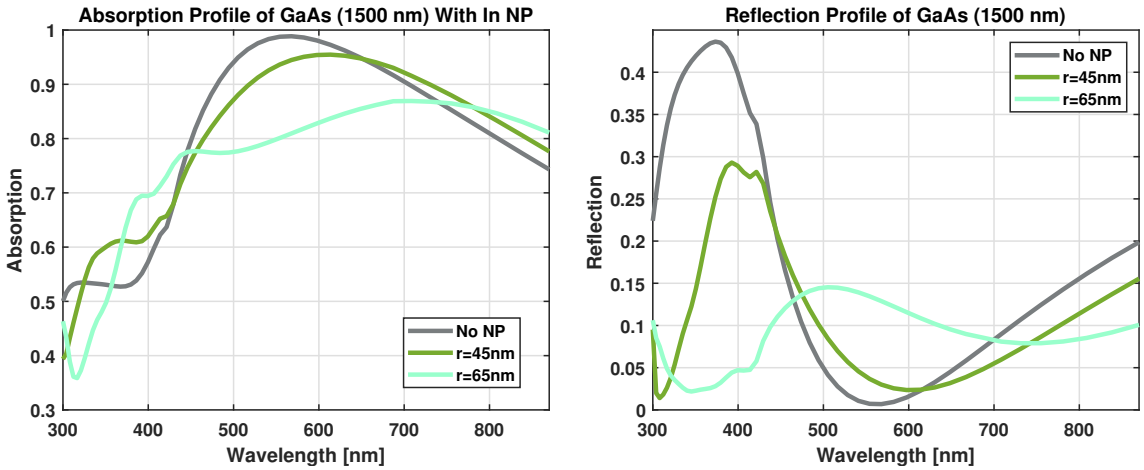

(a) Absorption profile.

(b) Reflection profile.

Figure 4.10: Absorption and reflection profile for a GaAs cell with absorbing layer thickness 1500 nm, without and with In nanoparticles of radius 45 nm and 65 nm at a period of 300 nm.

From the investigation on whether the nanoparticles affected the GaAs cell when its absorbing layer had a less than optimal thickness, the largest enhancement gained from the addition of Al and In nanoparticles on a GaAs cell with this configuration is shown in Figures 4.11a and 4.11b. The corresponding data are given in Tables 4.4 and 4.5. The largest enhancement obtained for the Al nanoparticles was found for a radius and period of 45 nm and 300 nm, respectively. The In nanoparticles were shown to give no positive enhancement to the absorption, similarly to the cell with optimal thickness.

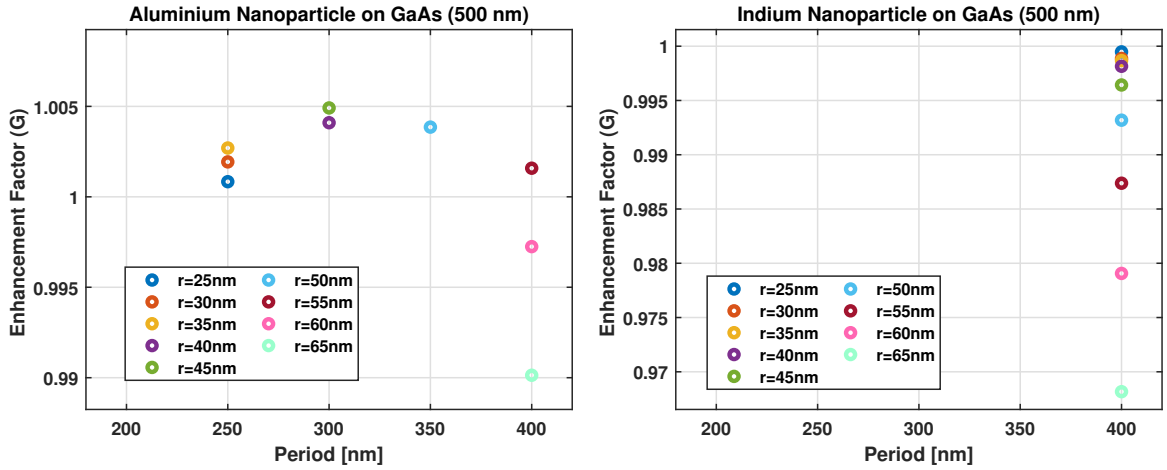

(a) Largest enhancement factor vs period for each Al radius parameter.

(b) Largest enhancement factor vs period for each In radius parameter.

Figure 4.11: Largest enhancement obtained from the addition of Al and In nanoparticles with radius parameter ranging from 25 - 65 nm onto a GaAs cell with absorbing layer thickness 500 nm.

Table 4.4: Largest enhancement factor obtained for each Al radius parameter at its corresponding period for the GaAs solar cell with absorbing layer thickness of 500 nm.

Al Radius [nm]	**Period [nm]**	**Enhancement Factor**
25	250	1.0008
30	250	1.0019
35	250	1.0027
40	300	1.0041
45	300	1.0049
50	350	1.0039
55	400	1.0016
60	400	0.9972
65	400	0.9901

Table 4.5: Largest enhancement factor obtained for each In radius parameter at its corresponding period for the GaAs solar cell with absorbing layer thickness of 500 nm.

In Radius [nm]	**Period [nm]**	**Enhancement Factor**
25	400	0.9995
30	400	0.9989
35	400	0.9987
40	400	0.9982
45	400	0.9964
50	400	0.9932
55	400	0.9874
60	400	0.9791
65	400	0.9682

As the In nanoparticles had no positive effect on either GaAs thickness, only the enhancement due to the Al nanoparticles was compared based on the absorbing layer thickness. By comparing Tables 4.2 and 4.4, the enhancement due to the Al nanoparticles was shown to be larger for a GaAs cell with optimal thickness. Based on tables, the addition of Al nanoparticles to the front surface of a GaAs cell, with the specific layout used in the thesis, can enhance absorption in the absorbing layer. Despite the

slightly lower enhancement obtained for the less than optimal thickness, it can be seen that Al nanoparticles may aid in reducing the thickness of the cell and thereby reduce the material usage and consequently the cost of manufacturing, which is one of the disadvantages of the GaAs solar cell.

The addition of In nanoparticles to the front surface of the GaAs cell was shown to have no positive enhancement on the absorption. Therefore, In nanoparticles should not be used as a plasmonic scattering mechanism for a GaAs cell with the specific setup utilized in the thesis.

4.2.4 Absorption Profile and Current Density of Optimized GaAs Solar Cell

Based on the results from all the previous subsections, the absorption and reflection profiles of the optimized GaAs solar cell, with and without the Al nanoparticles of radius 45 nm and period of 300 nm, were found and are shown in Figure 4.12. The absorption and reflection profile of the cell with In nanoparticles was disregarded due to its lack of positive enhancement.

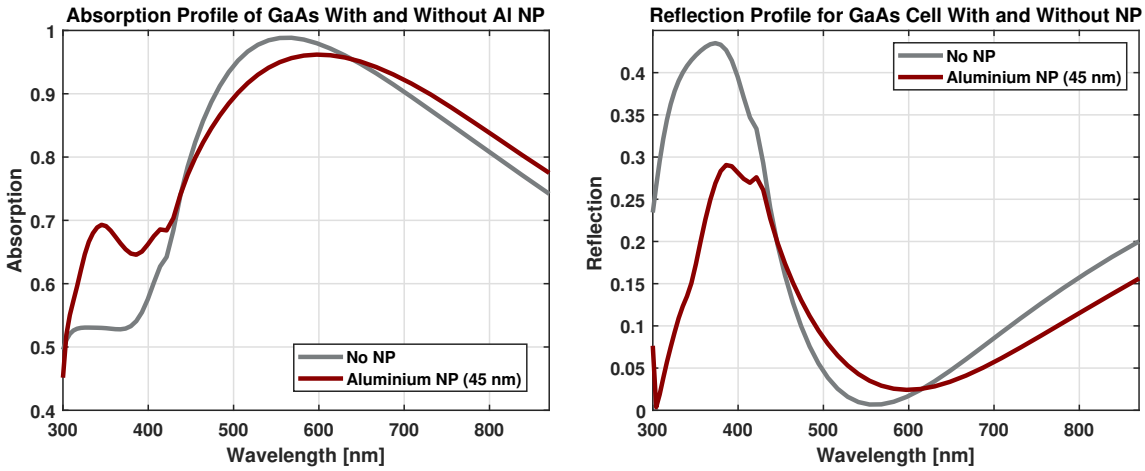

(a) Absorption profiles.

(b) Reflection profiles.

Figure 4.12: Absorption and reflection profiles for a GaAs cell with absorbing layer thickness 1500 nm, with and without optimal Al nanoparticles.

As shown in Figure 4.12a, the absorption profile for the cell with the Al nanoparticles had a significantly larger absorption in the wavelength region 300 - 430 nm and an increase in absorption in the wavelength region 630 - 870 nm compared to the absorption profile of the cell without the nanoparticles. In the wavelength region 430 - 630 nm, the addition of the Al nanoparticles led to a loss of absorption.

The reflection profiles of the GaAs cell with and without the Al nanoparticles are shown in Figure 4.12b. As can be seen, the reflection profile due to the Al nanoparticles is

slightly red-shifted. Due to this shift, the reflection profile has a much lower magnitude in the wavelength region 300 - 350 nm. This effect is probably caused by the periodic array of nanoparticles. In addition, the peak of the reflection profile for the cell with the nanoparticles has a lower magnitude due to the Al nanoparticles scattering more light into the cell.

By comparing the absorption and reflection profiles in Figure 4.12, it can be seen that despite the low reflection at wavelength 300 nm, the absorption profile does not have a corresponding increase in the same area. This indicates that the incident light is lost due to absorption by the other parts of the cell. To further investigate this, the incident light that was lost due to the Al nanoparticles is shown in Figure 4.13a. Note that the absorption profile shown in the figure is not completely accurate as the monitors measured a larger space than the actual space the nanoparticle occupied (see Figure 3.1), resulting in Figure 4.13a showing a slightly larger absorption than what it should be.

The amount of light absorbed by the ITO layer is given in Figure 4.13b. The addition of the Al nanoparticles led to a slight increase in absorption in the ITO layer. The absorption profiles shown in Figure 4.13 have a high absorption for wavelength 300 nm, which corresponds to the low absorption shown in Figure 4.12a.

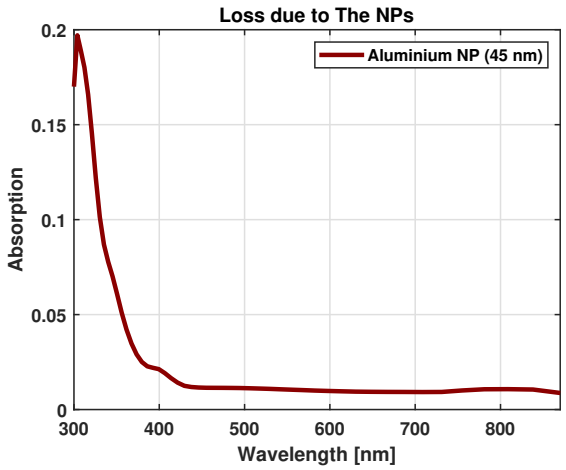

(a) Absorption profile for Al nanoparticles.

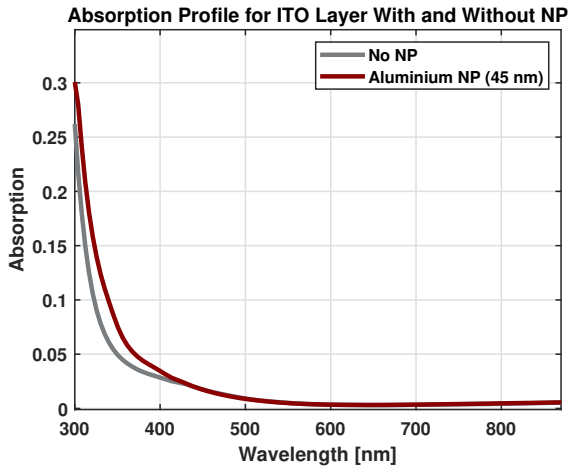

(b) Absorption profiles for the ITO layer.

Figure 4.13: Absorption profiles for the Al NP and the ITO layer, with and without the Al nanoparticles.

By investigating Figures 4.12a and 4.13b, it is apparent that the addition of the Al nanoparticles led to more light absorption in the solar cell in the wavelength region 300 - 430 nm. Thus, the Al nanoparticles were shown to have increased the absorption in the nearby material, which led to a larger current density in the cell with the Al nanoparticles present.

The current densities calculated based on the absorption profiles obtained for a cell with and without the Al nanoparticles are given in Table 4.6. The addition of the Al nanoparticles increased the absorption by 0.75% and is, therefore, a viable candidate to use for plasmonic light trapping schemes.

Table 4.6: The calculated current density for a GaAs solar cell with absorbing layer thickness 1500 nm, with and without Al nanoparticles of radius 45 nm and period 300 nm.

Configuration	**Radius [nm]**	**Period [nm]**	**J_{sc} [mA/cm^2]**	**G [%]**
No NP	0	-	28.035	-
Aluminium	45	300	28.245	0.75

4.3 Investigation of CdTe Solar Cell with ITO and Nanoparticles

This section contains the results and discussion based on simulating Al and In nanoparticles on the front surface of an optimized CdTe solar cell, with and without a glass substrate. The section presents the results obtained in the thickness sweep of the various thin films in the cell, convergence test for simulations, and the radius and period sweeps of the nanoparticles used for enhancing the light in-coupling. Based on the optimal values from the sweeps, the absorption and reflection profiles of an optimized cell with and without the glass substrate are presented.

4.3.1 Layer Thickness of CdTe Solar Cell

The layer thickness sweep result of the CdTe layer can be seen in Figure 4.14. The integrated absorption is shown to increase significantly for each thickness increment below 2500 nm, while the increments afterward did not yield as large of an increase. At thickness 4000 nm, the increase in absorption had approximately leveled out. Based on these results, a thickness of 4000 nm was chosen as the optimal absorbing layer thickness.

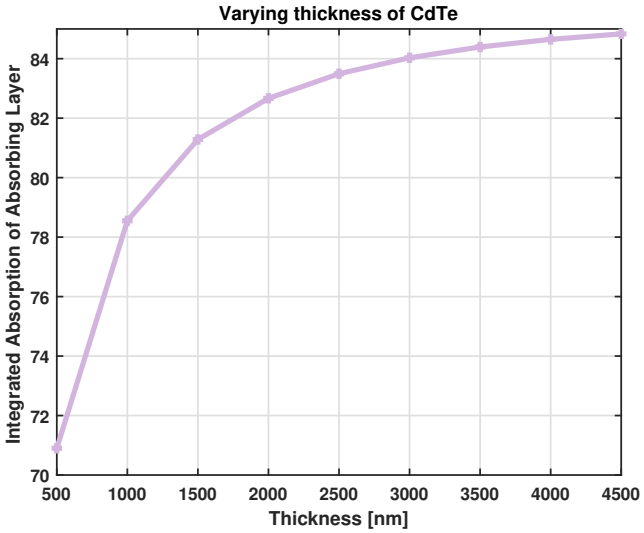

Figure 4.14: Integrated absorption of CdTe as a function of the CdTe layer thickness from 500 - 4500 nm.

The result of the CdS layer thickness sweep is shown in Figure 4.15. The shape of the function was very unstable for small thickness sizes, as indicated by the behavior occurring at thickness 20, 30, 40, and 50 nm. The integrated absorption reaches a peak point for a thickness of 20 nm. However, a valley occurs for thickness 30 and 40 nm before rising into another peak at 50 nm. This behavior implies that there may be a large error associated with these measurements. For a thickness increase after 50 nm, the absorption in the absorbing layer decreased steadily, which was due to more light

being absorbed by the CdS layer. The largest integrated absorption in the absorbing layer was obtained for a thickness of 20 nm. It was chosen as the optimal layer thickness, despite the potential error.

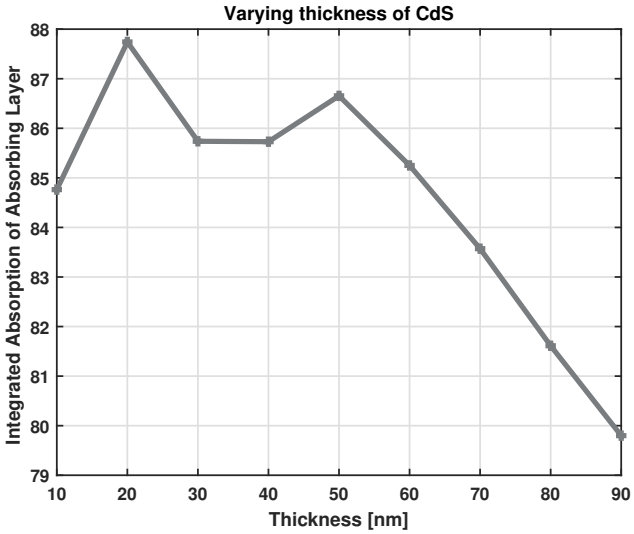

Figure 4.15: Integrated absorption of CdTe as a function of the CdS layer thickness from 10 - 90 nm.

The result of the ITO layer thickness sweep is shown in Figure 4.16. As depicted in the figure, the integrated absorption in the CdTe layer increased with each thickness increment up to a peak point at thickness 60 nm, which was chosen as the optimal thickness, before the absorption gradually decreased steadily due to more light absorption occurring in the ITO layer.

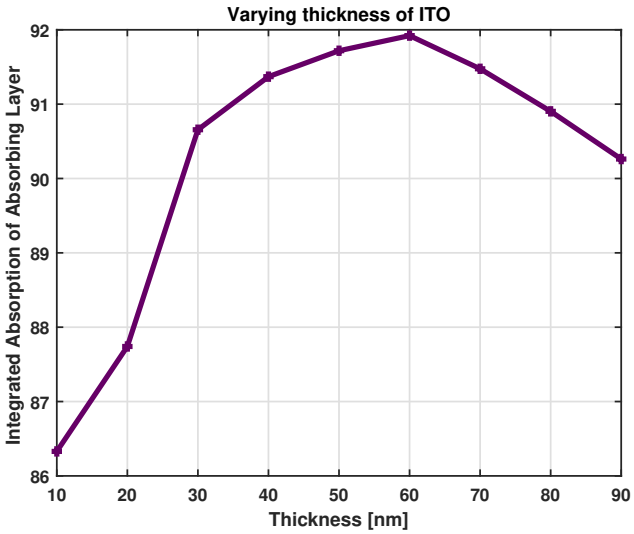

Figure 4.16: Integrated absorption of CdTe as a function of the ITO layer thickness from 10 - 90 nm.

Based on the data shown in Figures 4.14, 4.15, and 4.16, an optimized CdTe cell consists of a CdTe layer with a thickness of 4000 nm, a CdS layer with a thickness of 20 nm and

an ITO layer with a thickness of 60 nm. For a cell with less than optimal thickness, the CdTe layer was chosen to be 1000 nm.

Note that it is likely that by having glass as the background material in the simulation that the integrated absorption in the cell and the thickness of the layers may differ from results obtained if the simulation used air as background material.

4.3.2 Convergence Testing of CdTe Solar Cell

Based on the results obtained by the previous subsection, convergence testing for the distance between the PML boundary and the bottom monitor was performed for the optimized CdTe cell when the background material was air, where the result is shown in Figure 4.17a. The difference between current and previous measured absorption, σ_s, had approximately the same value except for the peak at 200 nm and valley at 450 nm. The magnitude difference of the peak and valley are of a small order, and it can therefore be assumed that there was little numerical error associated with the PML distance.

Figure 4.17b shows the result of the PML convergence test when the background material was glass. As can be seen, the differences had approximately the same values except for the two peaks at distances 250 nm and 350 nm. Similarly to Figure 4.17b, the difference in magnitude of these peaks was small, and it can be assumed that there was little numerical error associated with the PML distance.

Due to the great similarity and approximately linear behavior of both PML distance convergence tests, it was determined that a distance of 300 nm, with a corresponding associated error of approximately 0.025%, would be best suited for further simulations.

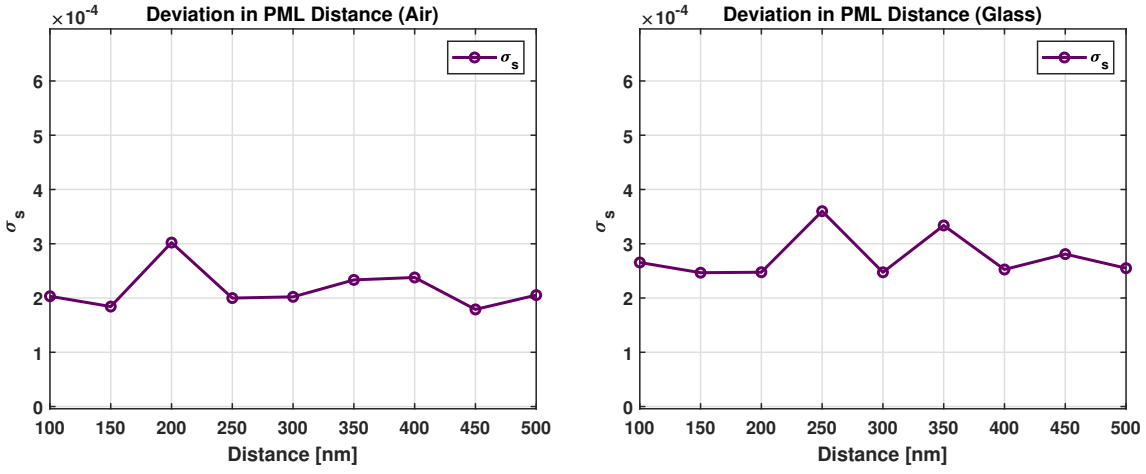

(a) Background material consisting of air.

(b) Background material consisting of glass.

Figure 4.17: The difference between current and previous results shown as a function of the distance between the bottom monitor and lower z boundary for a CdTe cell.

The result of the convergence test for the mesh accuracy setting when the background material was air is indicated in Figure 4.18a. As can be seen, at no point did the σ_s approach a linear approximation. This was also the case for the convergence test done when glass was the background material, as shown in Figure 4.18b. This means that for the CdTe cell, the mesh accuracy setting was a prominent source of error. The error was most likely due to the thickness of the CdS layer, as 20 nm may be too thin for the mesh setting in the simulation region to simulate properly. Because this mesh setting was suspected to be the cause, this was investigated by implementing a mesh override region that covered the entire CdS layer.

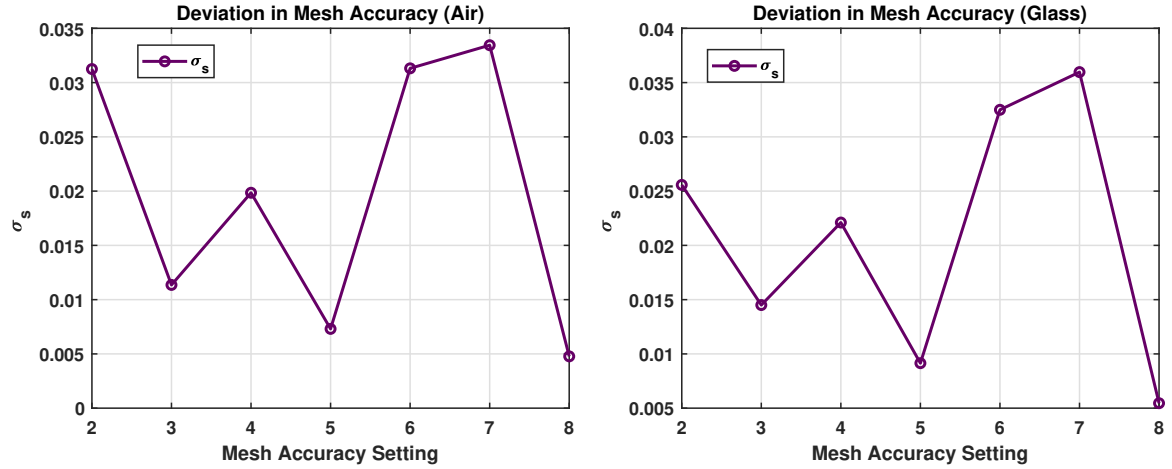

(a) Background material consisting of air.

(b) Background material consisting of glass.

Figure 4.18: The difference between current and previous results shown as a function of the mesh accuracy setting for a CdTe cell.

The result of investigating the addition of a mesh override region to the Cds layer, with background material of glass, is shown in Figure 4.19. As can be seen, the difference between current and previous measurements approached a linear approximation. It can be concluded that the fluctuations that are shown in Figures 4.18a and 4.18b were due to the thickness of the CdS layer being too thin to simulate accurately. The addition of the mesh override region increased the simulation time significantly, and due to the time frame, was not implemented in further simulations for the CdTe cell. This was not a problem because the potential error associated with the mesh accuracy setting (see Figure 4.18) had a low magnitude even without the additional mesh override region.

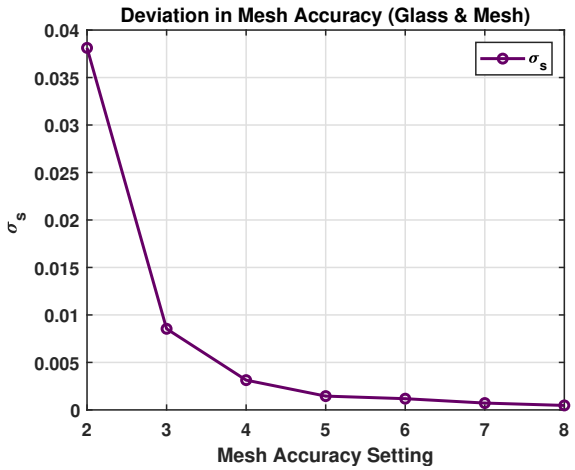

Figure 4.19: The difference between current and previous results shown as a function of the mesh accuracy setting for a CdTe cell with a mesh override region covering the CdS layer and glass as background material.

Since the mesh override region was not utilized in further simulations, the mesh accuracy setting had to be determined from Figures 4.18a and 4.18b. The corresponding σ_s of the mesh accuracy settings for both air and glass are given in Table 4.7. Since the values fluctuated with large magnitude differences between each mesh accuracy setting, the choice of which mesh setting to utilize was uncertain. Based on the values in Table 4.7 and Figures 4.18a and 4.18b, it was determined that mesh accuracy setting 5, with a corresponding error of approximately 0.8%, was a reasonable choice as a trade-off between error and time.

Table 4.7: Difference between the current and previous measurement σ_s obtained by the convergence test for CdTe cell with air and glass as material background to corresponding mesh accuracy setting.

Mesh Accuracy Setting	$\boldsymbol{\sigma_s}$ **(Air)**	$\boldsymbol{\sigma_s}$ **(Glass)**
1	-	-
2	0.0312	0.0255
3	0.0113	0.0145
4	0.0198	0.0221
5	0.0073	0.0091
6	0.0313	0.0324
7	0.0334	0.0359
8	0.0047	0.0054

4.3.3 Nanoparticle Radius and Period for CdTe Solar Cell

The radius and period sweep of the nanoparticles were performed on the optimized CdTe solar cell with the mesh accuracy setting and the distance between the bottom monitor and the PML boundary found in the previous subsection. As the thesis was interested in the potential enhancement for a CdTe solar cell without and with a glass substrate, the sweeps were performed for both CdTe configurations.

Background Material: Air

The CdTe configuration without the glass substrate was first considered. The results of the radius sweeps of the Al nanoparticles are shown in Figure 4.20a, which shows the enhancement factor as a function of the period. At a period of 200 nm, it is shown that for radius < 45 nm, the functions gave an enhancement of $G > 1$. For larger periods, the enhancement approached $G \approx 1$. For radius > 50 nm and a period of 200 nm, the functions gave an enhancement of $G < 1$ and increased for larger periods until $G \approx 1$. This indicated that the functions would reach a peak point above $G = 1$ before gradually stabilizing towards no enhancement for larger periods.

The largest enhancement point of each enhancement function given in Figure 4.20a is shown in Figure 4.20b, where the corresponding data is given in Table 4.8. As shown in the figure and the table, the largest enhancement achieved by the addition of Al nanoparticles was when the nanoparticles had a radius of 45 nm and a period of 250 nm. Note that the difference between the enhancement obtained from radius parameter 45 and 50 nm was negligible, and either parameter could be used as the optimal radius parameter. It is likely that the peak points of either radius parameter occurred at some period between 225 - 325 nm and that there would be a larger magnitude difference between them if the actual peak points were measured.

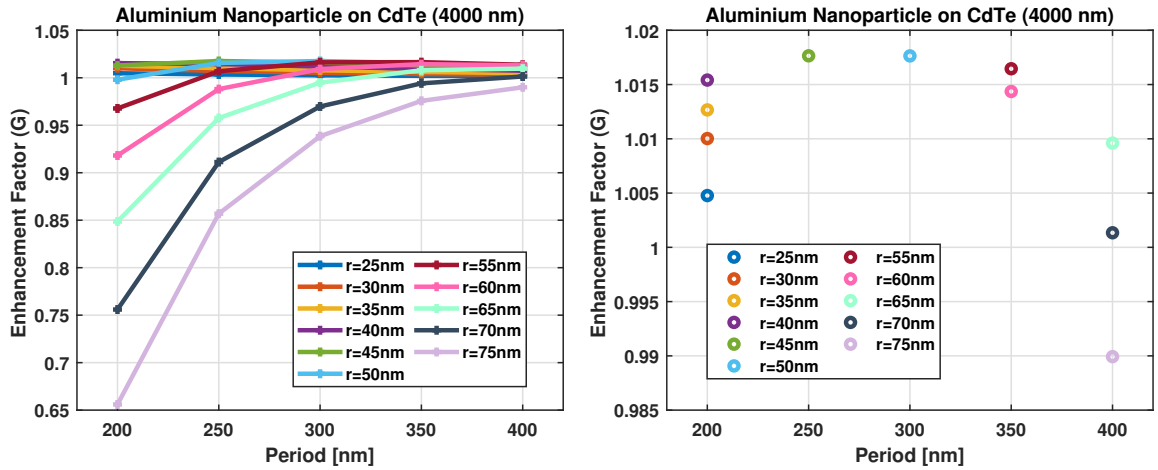

(a) Enhancement factor as a function of period for each Al radius parameter.

(b) Largest enhancement factor vs period for each Al radius parameter.

Figure 4.20: Enhancement factor calculated from a CdTe cell with absorbing layer thickness 4000 nm and Al NPs with radius parameters from 25 - 75 nm.

Table 4.8: Largest enhancement factor calculated for each Al radius parameter at its corresponding period for the CdTe solar cell with absorbing layer thickness of 4000 nm.

Radius [nm]	**Period [nm]**	**Enhancement Factor**
25	200	1.0048
30	200	1.0100
35	200	1.0127
40	200	1.0154
45	250	1.01765
50	300	1.01764
55	350	1.0165
60	350	1.0144
65	400	1.0096
70	400	1.0013
75	400	0.9899

The results of the radius sweeps for the In nanoparticles are given in Figure 4.21a, which shows the enhancement factor for each radius parameter as a function of the period. It is similar to Figure 4.20a, except the function magnitudes are lower compared to the Al functions.

The largest enhancement factor obtained by each function in Figure 4.21a is shown in Figure 4.21b, where the corresponding data is given in Table 4.9. As shown in both the figure and table, In nanoparticles with a radius of 40 nm and a period of 250 nm gave the largest enhancement in absorption.

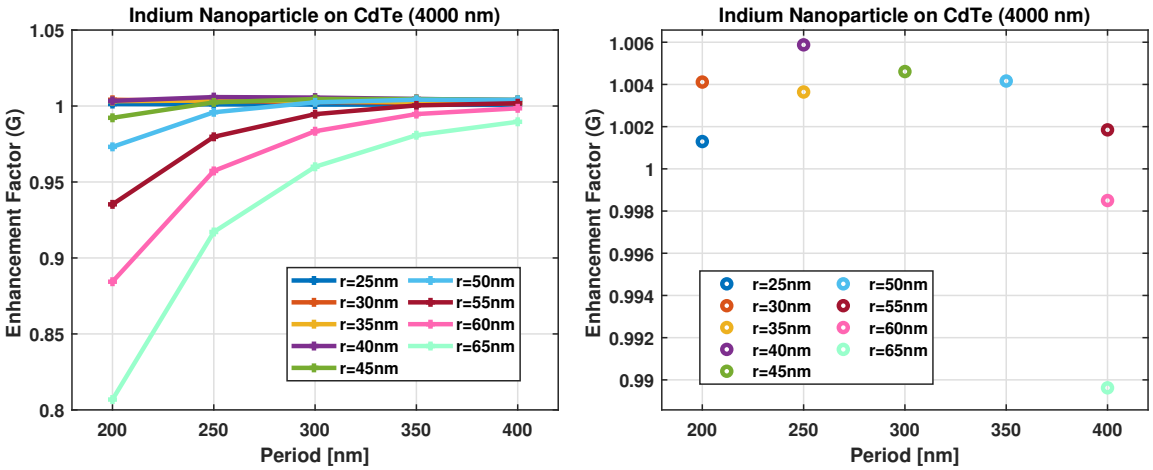

(a) Enhancement factor as a function of period for each In radius parameter.

(b) Largest enhancement factor vs period for each In radius parameter.

Figure 4.21: Enhancement factor calculated from a CdTe cell with absorbing layer thickness 4000 nm and In NPs with radius parameters from 25 - 65 nm.

Table 4.9: Largest enhancement factor calculated for each indium radius parameter at its corresponding period for the CdTe solar cell with absorbing layer thickness of 4000 nm.

Radius [nm]	**Period [nm]**	**Enhancement Factor**
25	200	1.0013
30	200	1.0041
35	250	1.0036
40	250	1.0059
45	300	1.0045
50	350	1.0042
55	400	1.0018
60	400	0.9985
65	400	0.9896

From the investigation on whether the nanoparticles gave an enhancement to a CdTe cell with less than optimal absorbing layer thickness, the largest enhancement of the radius sweeps for the Al and In nanoparticles performed for a cell with this configuration are shown in Figures 4.22a and 4.22b, respectively. The corresponding data are given in Tables 4.10 and 4.11. As both nanoparticles were shown to give an enhancement to the absorption, the enhancement factors obtained by both nanoparticles for the less than optimal CdTe cell will be compared to the enhancement factors found for the optimized CdTe cell.

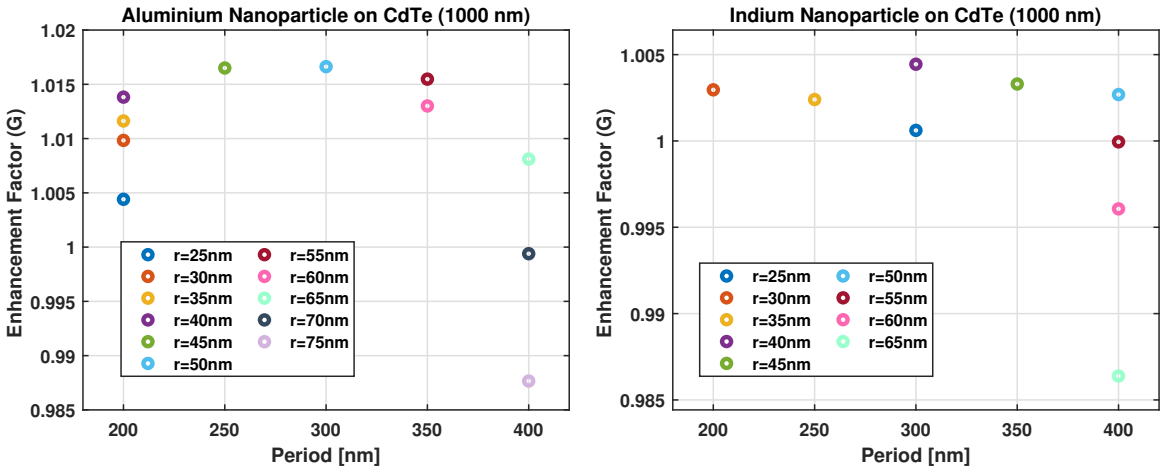

(a) Largest enhancement factor vs period for each Al radius parameter.

(b) Largest enhancement factor vs period for each In radius parameter.

Figure 4.22: Largest enhancement obtained from the addition of Al and In nanoparticles with radius parameter ranging from 25 - 75 nm and 25 - 65 nm, respectively, onto a CdTe cell with absorbing layer thickness 1000 nm.

Table 4.10: Largest enhancement factor calculated for each Al radius parameter at its corresponding period for the CdTe solar cell with absorbing layer thickness of 1000 nm.

Radius [nm]	**Period [nm]**	**Enhancement Factor**
25	200	1.0044
30	200	1.0098
35	200	1.0116
40	200	1.0138
45	250	1.0165
50	300	1.0166
55	350	1.0155
60	350	1.0130
65	400	1.0081
70	400	0.9994
75	400	0.9877

Table 4.11: Largest enhancement factor calculated for each In radius parameter at its corresponding period for the CdTe solar cell with absorbing layer thickness of 1000 nm.

Radius [nm]	**Period [nm]**	**Enhancement Factor**
25	300	1.0006
30	200	1.0030
35	250	1.0024
40	300	1.0044
45	350	1.0033
50	400	1.0027
55	400	0.9999
60	400	0.9961
65	400	0.9864

As can be seen, when comparing Figures 4.20b and 4.22a, there was little difference between the largest enhancements found for the Al nanoparticles for a cell with a thickness of 4000 nm or 1000 nm. There was only a magnitude difference, where the enhancement gained from the addition of the nanoparticles onto a cell with a CdTe thickness of 1000 nm had a slightly lower magnitude than a cell with a CdTe thickness of 4000 nm.

The difference in magnitude between the largest enhancement gained by adding In nanoparticles onto a CdTe cell with absorbing layer thickness of 4000 and 1000 nm was large, as shown in Figures 4.21b and 4.22b. The magnitude of all the enhancement factors gained by adding the nanoparticles onto a cell with a CdTe thickness of 1000 nm was lower than the enhancement factor found for the cell with CdTe of 4000 nm. In addition, the largest enhancement of radius parameters 25, 40, 45, and 50 nm occurred at different periods for the different CdTe thicknesses. This shift in period may indicate that the large RMS error value of the In material led to more imprecise measurements, as the Al nanoparticle measurements did not have a shift in period.

The effect of the nanoparticles had a lesser effect on the light in-coupling on the CdTe cell with a less than optimal absorbing layer thickness, which can be seen in Tables 4.8, 4.9, 4.10, and 4.11. Therefore, the addition of Al and In nanoparticles is best suited for a CdTe cell with an optimal thickness but can still be used to negate the loss of efficiency in reduced absorbing layer thickness. The parameters for the Al and In nanoparticles that gave the largest enhancement for the optimized CdTe cell is given in Table 4.12

Table 4.12: The radius and period parameters of the Al and In nanoparticles, which gave the largest enhancement in an optimized CdTe cell.

NP	Radius [nm]	Period [nm]
Al	45	250
In	40	250

Background Material: SiO_2

As CdTe solar cells are commonly fabricated on glass substrates as the front of the cell, the addition of the nanoparticles onto a CdTe with a glass substrate was investigated, where the nanoparticles had the glass as its surrounding medium, see Section 3.1. Figure 4.23a depicts the results of the radius sweeps of Al nanoparticles on a CdTe cell with a thickness of 4000 nm when the background material was set to SiO_2. The functions are shown to approach G = 1. The largest enhancement value of each function is shown in Figure 4.23b, and as can be seen, there is little enhancement to be gained by Al nanoparticles as a light scattering mechanism to this configuration.

The parameters of the Al nanoparticles that gave the largest enhancement are given in Table 4.13. As indicated in the table, the largest enhancement obtained was approximately 0.04%, where the radius was 10 nm and the period was 400 nm. This implies that the addition of Al nanoparticles to the cell was a hindrance rather than an aid in increasing the light in-coupling of the cell.

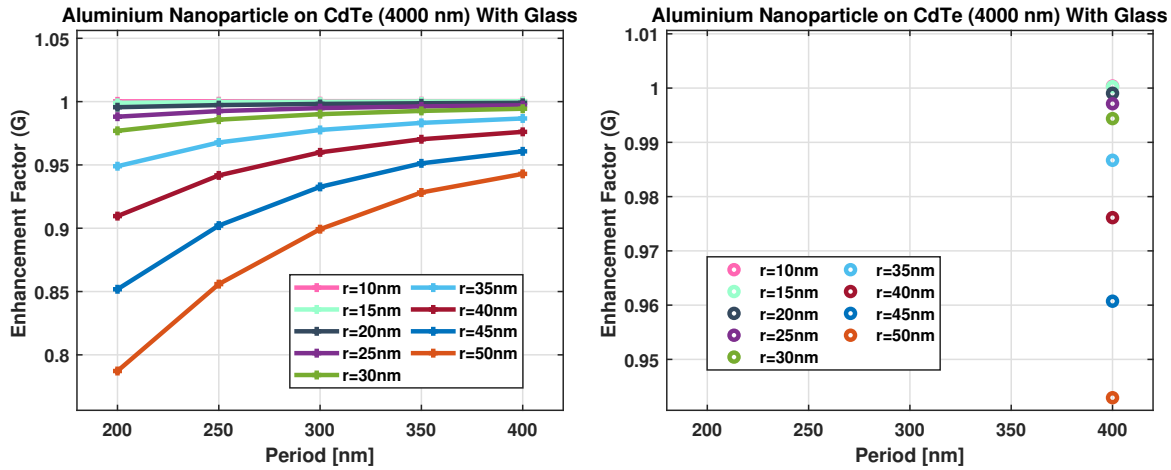

(a) Enhancement factor as a function of period for each Al radius parameter.

(b) Largest enhancement factor vs period for each Al radius parameter.

Figure 4.23: Enhancement factor calculated from a CdTe cell with absorbing layer thickness 4000 nm and Al NPs with radius parameter ranging from 10 - 50 nm, where the background material was glass.

The enhancement results of the radius sweeps for the In nanoparticles added to a CdTe cell with glass as background material are shown in Figure 4.24a. The functions shown in the figure are mostly similar to the ones found for the Al nanoparticles shown in Figure 4.23a, except that the functions for the In nanoparticles had a larger negative magnitude for radius parameters 25 - 50 nm. The largest enhancement values of each function are shown in Figure 4.24b, where it can be seen that there is little enhancement to be gained.

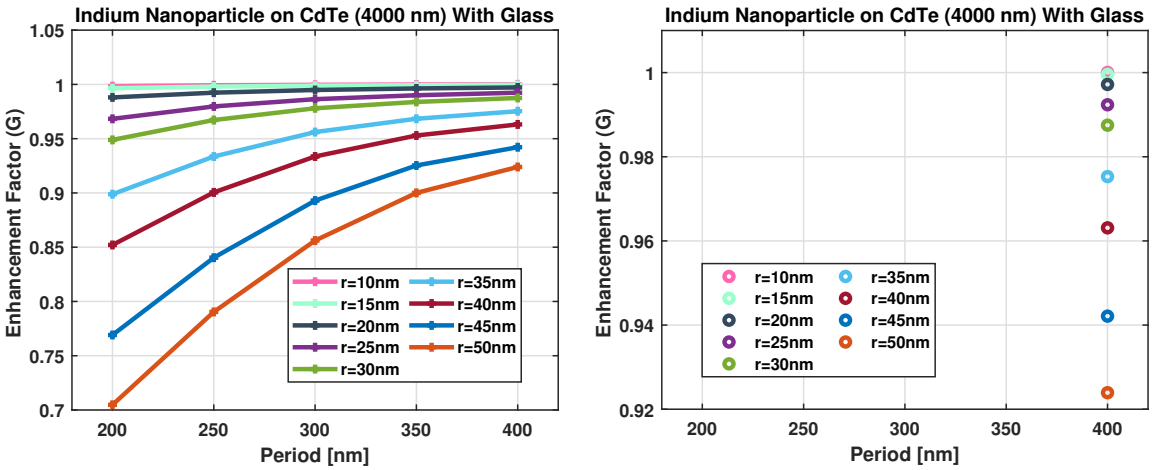

(a) Enhancement factor as a function of period for each In radius parameter.

(b) Largest enhancement factor vs period for each In radius parameter.

Figure 4.24: Enhancement factor calculated from a CdTe cell with absorbing layer thickness 4000 nm and In NPs with radius parameter ranging from 10 - 50 nm, where the background material was glass.

The parameters of the In nanoparticles, which gave the largest enhancement to the cell, are given in Table 4.13. The enhancement gained by the addition of In nanoparticles was approximately 0.01%, with the same parameters as the Al nanoparticles.

The magnitude of the enhancements indicated in Table 4.13 is of such a low value that it is questionable whether the nanoparticles gave any positive enhancement or if it was due to numerical error. Even if the enhancement was due to the nanoparticles, the increase in light absorption was only 0.04% and 0.01% for the Al and In nanoparticles, respectively. Thus, the addition of either Al or In nanoparticles to a CdTe cell with a glass substrate is unwise due to its inefficiency. Since the simulation considered a configuration where the nanoparticles were encased in glass (see Figure 3.2), it is likely that such a setup is unpractical. Realistically, the addition of any type of plasmonic nanoparticles would be deposited onto the glass substrate and thereafter have the ARC/TCO or some other thin film deposited onto this substrate. Thus, the nanoparticles are more likely to be encased by the ARC/TCO or thin film, and not by the glass. This configuration was not considered in the thesis due to the interest in comparing the same setup, where the nanoparticles were placed on top of the ITO, with the GaAs solar cell.

Table 4.13: Largest enhancement factor obtained by the addition of Al and In with optimal radius and period, respectively, onto a CdTe cell with absorbing layer thickness 4000 nm and with glass as background material.

NP	Radius [nm]	Period [nm]	G	Enhancement [%]
Al	10	400	1.0004	0.04
In	10	400	1.0001	0.01

4.3.4 Absorption Profile and Current Density of Optimized CdTe Solar Cell

Based on the nanoparticle parameters found for a CdTe cell without a glass substrate in the previous subsection, the absorption and reflection profiles of an optimized CdTe solar cell were found, with and without Al or In nanoparticles. Figure 4.25a illustrates the absorption profiles, while the reflection profiles are shown in Figure 4.25b.

As shown in Figure 4.25a, the addition of either nanoparticles improved the amount of absorbed light in the wavelength regions 325 - 500 nm and 600 - 850 nm. In the wavelength region of 300 - 325 nm and 500 - 600 nm, the presence of both nanoparticles is shown to decrease the absorption compared to a cell without them. The profiles of the Al and In nanoparticles differ from one another in the wavelength region 300 - 600, where the Al nanoparticles gave a larger enhancement in absorption. At wavelength region 600 - 850 nm, the absorption profiles of the nanoparticles are approximately the same.

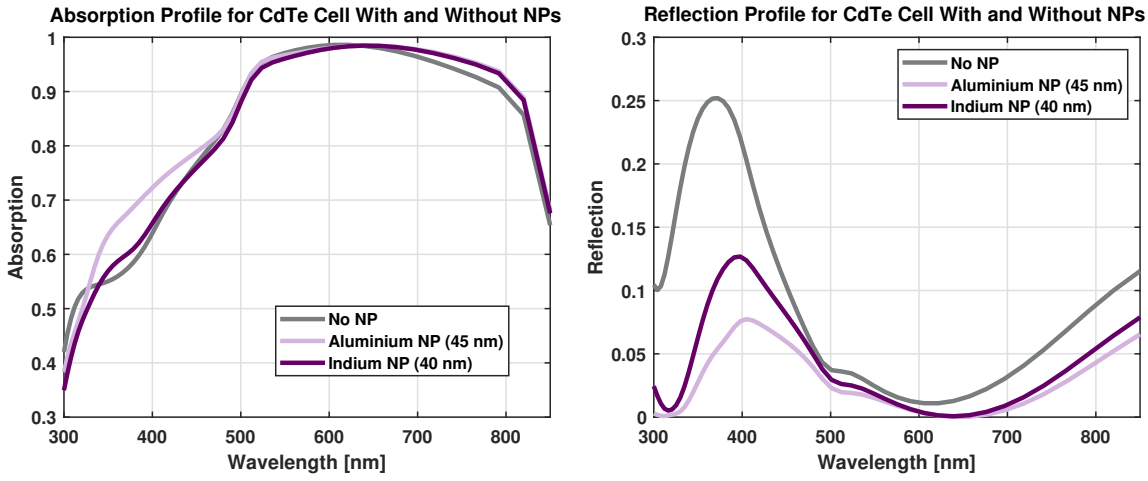

(a) Absorption profiles.

(b) Reflection profiles.

Figure 4.25: Absorption and reflection profiles for a CdTe cell with absorbing layer thickness 4000 nm and no glass substrate, with and without optimal Al and In nanoparticles.

The reflection profiles of the cell obtained by the nanoparticles show a slight red shift compared to the reflection profile of the cell without any nanoparticles. In addition, the magnitudes of the red-shifted reflections are significantly lower than the reflection of the bare cell. The red shift and the decreased magnitude in reflection correspond to the increased absorption in the wavelength region 325 - 500 nm.

When comparing the absorption and reflection profiles in Figure 4.25, it can be seen that despite the low reflection at wavelength region 300 - 325 nm, the absorption profile does not have a corresponding increase in the same area. As found for the GaAs cell in Section 4.2.4, this was due to absorption in the ITO and Al nanoparticle. In order to investigate if this was the same case for the CdTe cell, the absorption in each layer and in the nanoparticles was measured.

The loss of absorption in the solar cell due to the presence of the nanoparticles is shown in Figure 4.26a. Note that the absorption profiles were not completely accurate due to the monitors measuring the amount of light in an larger amount of space, see Figure 3.1. Despite this inaccuracy, the figure was sufficient to illustrate why the absorption profiles of the nanoparticles in Figure 4.25a have a lower absorption in the wavelength region 300 - 325 nm compared to the bare cell. Comparing Figures 4.25b and 4.26a shows that the lowered reflection 300 - 375 nm is mostly due to the nanoparticles absorbing the incoming light.

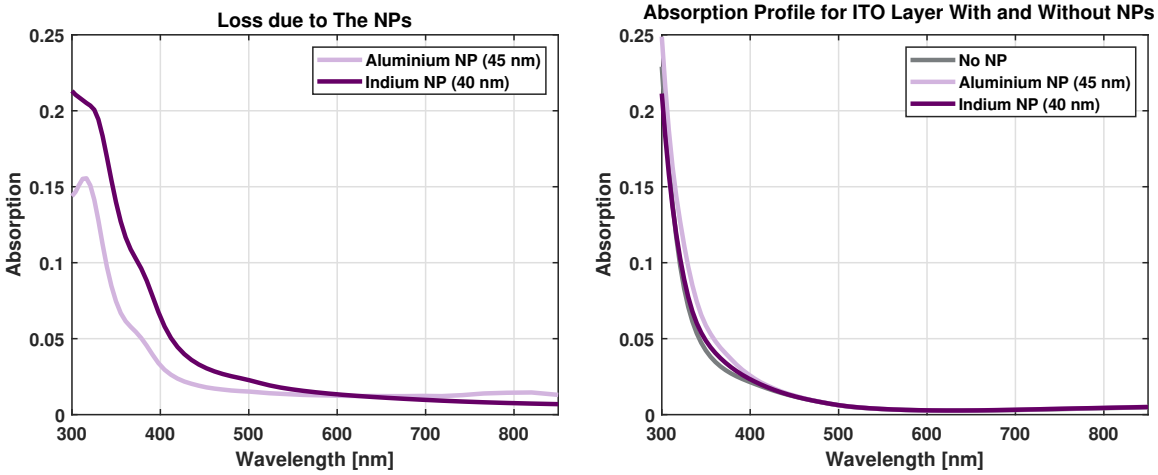

(a) Absorption profiles of Al and In.

(b) Absorption profile of ITO.

Figure 4.26: Absorption profiles for the nanoparticles and the ITO layer, with and without the nanoparticles.

The absorption in the ITO layer is illustrated in Figure 4.26b, and as can be seen, there was some loss of light via absorption in the ITO layer for wavelength region 300 - 550 nm. The addition of the nanoparticles caused a slight increase in absorption in the ITO layer, especially from the Al nanoparticles.

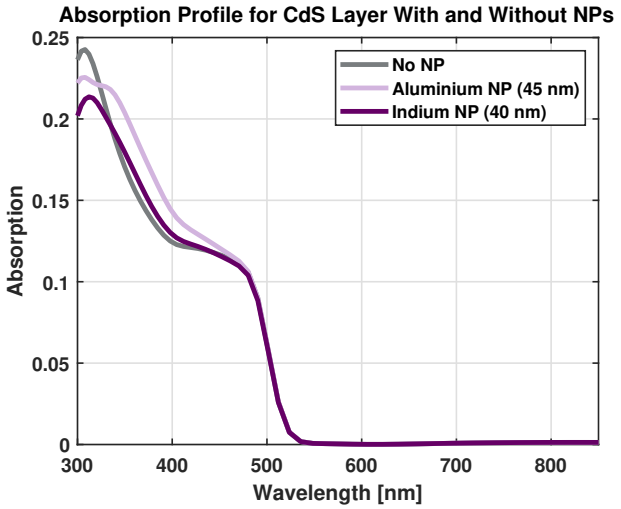

Figure 4.27: Absorption profiles for the CdS layer, with and without the nanoparticles.

Some light was also lost due to absorption by the CdS layer, as shown in Figure 4.27. When adding nanoparticles, the peak occurring at wavelength 325 nm decreased in size. However, this was mostly due to the nanoparticles themselves absorbing the light in this region. The In nanoparticles did not cause any significant increase in absorption. However, the Al nanoparticles did result in a significant increase in the absorption from wavelength region 350 - 500 nm.

Based on the various absorption profiles and the data shown in Table 4.14, the Al nanoparticles provided the largest enhancement to absorption, mostly due to the lowered reflection in the wavelength region 325 - 500 nm. The enhancement obtained by the addition of Al nanoparticles with a radius of 45 nm and a period of 250 nm gave an increase of 1.76% in light absorption. The enhancement gained by adding In nanoparticles with a radius of 40 nm and a period of 250 nm to the optimized CdTe cell was an increase of 0.59% in light absorption. Therefore, adding Al or In nanoparticles to the front surface of a CdTe cell without a glass substrate may improve the light in-coupling in the absorbing layer and improve the absorption of the cell. This may not be the case for a CdTe cell with a glass substrate, as indicated in Table 4.13, and further investigation had to be performed.

Table 4.14: The calculated current density for a CdTe solar cell with absorbing layer thickness 4000 nm, with and without Al and In nanoparticles of radius 45 nm, period 250 nm, and radius 40 nm, period 250 nm, respectively.

Configuration	**Radius [nm]**	**Period [nm]**	**J_{sc} [mA/cm^2]**	**[%]**
No NP	0	-	26.283	-
Aluminium	45	250	26.747	1.76
Indium	40	250	26.440	0.59

The absorption and reflection profiles of a CdTe cell with a glass substrate and Al and In nanoparticles with parameters given in Table 4.13 are shown in Figures 4.28a and 4.28b. As can be seen, the nanoparticle profiles are almost identical to the profile without the nanoparticles. Therefore, it can be concluded that the enhancement given in Table 4.13 was due to numerical error, not because of the nanoparticles. The addition of either Al or In nanoparticles as scattering mechanisms on the front surface of a CdTe cell with a glass substrate is therefore not a viable way to increase light in-coupling in the cell.

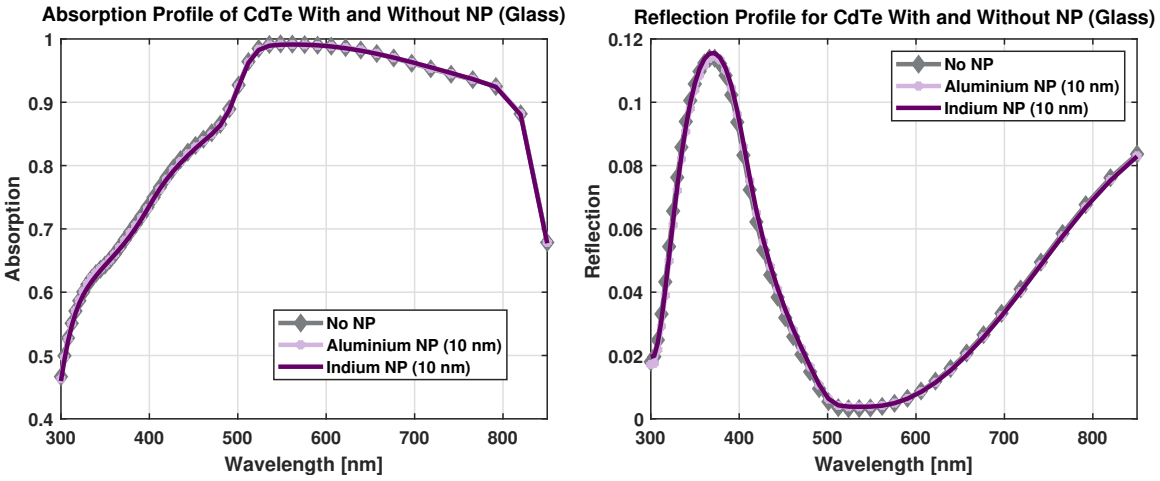

(a) Absorption profiles of CdTe with glass substrate.

(b) Reflection profiles of CdTe cell with glass substrate.

Figure 4.28: Absorption and reflection profiles for a CdTe cell with absorbing layer thickness 4000 nm and glass substrate, with and without optimal Al and In nanoparticles.

4.4 Comparison of Optimized GaAs and CdTe Solar Cells with Nanoparticles

As the optimized GaAs and CdTe solar cells had similar simulations performed, a comparison of the enhancement due to the nanoparticles was carried out. This was done to determine the overall effect of the nanoparticles, which nanoparticle material was best suited to be a plasmonic scattering mechanism, and which solar cell technology was more receptive towards this type of light trapping scheme.

As shown in Table 4.15, the addition of Al nanoparticles gave an increase in light in-coupling in the absorbing layer for both the GaAs cell and the CdTe cell without the glass substrate. The largest enhancement for either the GaAs or CdTe cell was obtained when the absorbing layer thickness was optimal. In addition, the Al nanoparticles with a radius of 45 nm gave, in both situations, the largest enhancement, although the period differed from one another.

The increase in light in-coupling had a larger magnitude for the CdTe cell compared to the GaAs cell by approximately 1%. It can therefore be concluded that the addition of Al nanoparticles is more suited for a CdTe solar cell with no glass substrate than

a GaAs solar cell. However, when the glass substrate was present in the CdTe cell simulation, which is the case for most CdTe cells, the addition of the Al nanoparticles gave no positive enhancement.

Table 4.15: Largest enhancement gained by the addition of Al nanoparticles to a GaAs cell of thickness 1500 and 500 nm, and a CdTe cell of thickness 4000 and 1000 nm, with or without a glass substrate.

Thin-film cell	**Radius [nm]**	**Period [nm]**	**Enhancement [%]**
GaAs (1500 nm)	45	300	0.75
GaAs (500 nm)	45	300	0.49
CdTe (4000 nm)	45	250	1.75
CdTe (1000 nm)	50	300	1.66
CdTe (Glass)	10	400	0.04

The addition of In nanoparticles to the front surface of the GaAs and CdTe cell gave an increase in light in-coupling for only the CdTe cell without the glass substrate, which can be seen in Table 4.16. The addition of In nanoparticles to the GaAs cell with a thickness of either 1500 nm or 500 nm did not yield any positive enhancement in light in-coupling. The addition of In to the CdTe cell of both thicknesses gave an enhancement in light in-coupling, where the optimal thickness gained the most enhancement. However, the addition of the In nanoparticles to a CdTe cell with the glass substrate gave no enhancement.

As shown in Tables 4.15 and 4.16, the magnitude of the enhancement due to the In nanoparticles was relatively low compared to the enhancement due to Al nanoparticles. The GaAs cell had no positive enhancement in light in-coupling due to the In nanoparticles, and since the cell only showed minor enhancement due to the Al nanoparticles, the cell likely had no positive enhancement due to the low magnitude of the enhancement gained by the In nanoparticles.

Table 4.16: Largest enhancement gained by the addition of an In nanoparticles to a GaAs cell of thickness 1500 and 500 nm, and a CdTe cell of thickness 4000 and 1000 nm, with and without a glass substrate.

Thin-film cell	**Radius [nm]**	**Period [nm]**	**Enhancement [%]**
GaAs (1500 nm)	25	400	0.00
GaAs (500 nm)	-	-	-
CdTe (4000 nm)	40	250	0.59
CdTe (1000 nm)	40	300	0.44
CdTe (Glass)	10	400	0.01

Based on the results in Tables 4.15 and 4.16, it can be determined that the thickness of the absorbing layer plays a large role in the effect of the nanoparticles. The results imply that the light scattered by the nanoparticles can penetrate deeply into the absorbing layer before it is absorbed. In addition, the tables indicate that the GaAs cell was less affected by the addition of the nanoparticles compared to the CdTe cell. By studying Figures 4.10 and 4.12, it can be seen that this was due to an increased reflection in the wavelength region 425 - 625 nm.

As shown in Figures 4.10a, 4.12a, and 4.25a, the nanoparticles mostly increased the absorption in the wavelength region 300 - 400 nm. The figures indicate that the Al nanoparticles gave a greater response than the In nanoparticles, which is why the Al nanoparticles are best suited for being utilized as a plasmonic sub-wavelength scattering mechanism.

4.5 Potential Errors

There were likely some sources of error in the simulations due to its numerical nature. One such source was the method of calculating the current density assumed that all electron-hole pairs contributed to the photocurrent [64], which meant that the current density would inherently have a larger value compared to a realistic solar cell. This can be negated by using Lumerical's FDTD and CHARGE software packages concurrently, where the CHARGE software package will calculate the actual photocurrent in the solar cell. For an even more realistic simulation, the HEAT software package can measure the heating of the solar cell and find how much energy is lost due to heat [71].

Another potential source of error was the mesh accuracy setting for the simulation of the CdTe cell. Due to the non-linear shape of the convergence test results, the measurements for the cell may have been inaccurate. Lastly, the RMS error value for the In data in Lumerical's database was quite large. This could potentially have led to imprecise measurements when considering the In nanoparticles.

Chapter 5

Results and Discussion: Experiments

The results of the experimental part are described and discussed in this chapter. Firstly, the results of the deposition of Al nanoparticles onto the Si substrates and the Si solar cells are reported and discussed. Finally, the efficiency of a post-deposition Si solar cell is compared to its pre-deposition efficiency.

5.1 Deposition of Al Nanoparticles

The results of the deposition of the Al nanoparticles are given as surface morphology images. The surface morphology of substrates 1 and 2 are shown in Figures 5.1a and 5.1b, respectively. As can be seen, a large amount of agglomerations of various sizes has occurred. Substrate 2 had larger agglomerations compared to substrate 1. The surface coverage of the nanoparticles is given in Table 5.1, where substrate 1 had surface coverage of 4.3% and substrate 2 had surface coverage of 10.0%. Substrate 2 had a large surface coverage compared to substrate 1 due to the large agglomeration in the upper left corner. Drying the solution of the substrate via evaporation may have resulted in larger agglomerations. However, there is not enough data to conclude anything with certainty.

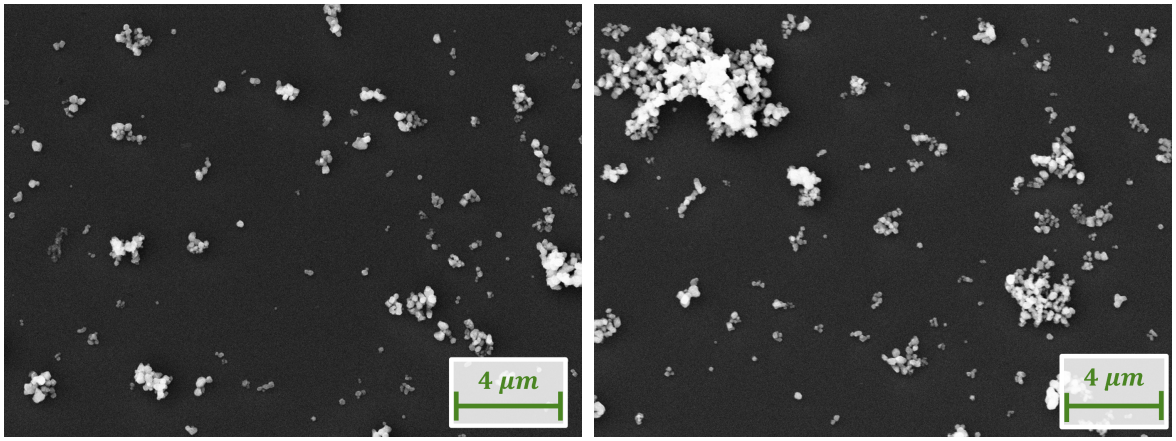

(a) Substrate 1 (b) Substrate 2

Figure 5.1: SEM imaging of substrate 1 and 2.

Figures 5.2a and 5.2b shows the surface morphology of substrates 3 and 4. The surface morphology of the two substrates are shown to be mostly similar, meaning that utilizing a pipette vs. dipping and suspending the substrate in the solution for 10 min had no significant effect on the surface morphology. Substrate 4 had fewer large agglomerations than substrate 3. However, this might be due to either the increased sonication time or the increased temperature. The surface coverage for each substrate is given in Table 5.1, where substrate 3 had a surface coverage of 3.5% and substrate 4 had surface coverage of 2.8%.

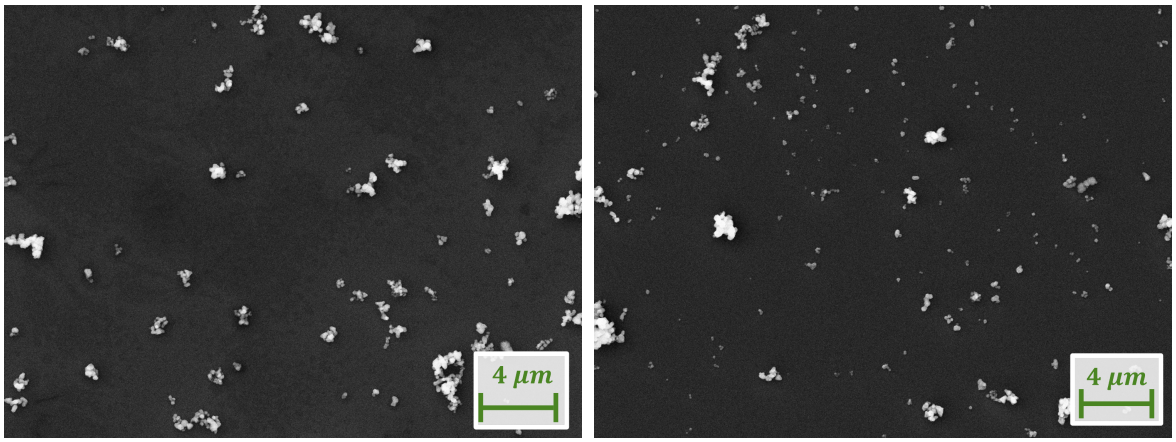

(a) Substrate 3 (b) Substrate 4

Figure 5.2: SEM imaging of substrate 3 and 4.

The surface morphology of substrate 5 is shown in Figure 5.3a. There are some large agglomerations present in the image. However, most of the particles indicated in the image are agglomerations consisting of only a couple of nanoparticles. It is uncertain whether the decrease in large agglomerations was due to the sonication or the temperature. The surface coverage of the substrate is given in Table 5.1, and was 4.9%.

Figure 5.3b shows the surface morphology of substrate 6. As can be seen, there are almost no nanoparticles present in the image. It is likely that during the long sonication time, the large agglomerations sank to the bottom of the solution and left a low number of particles in the upper part of the solution, which led to a very low surface coverage of 0.2%.

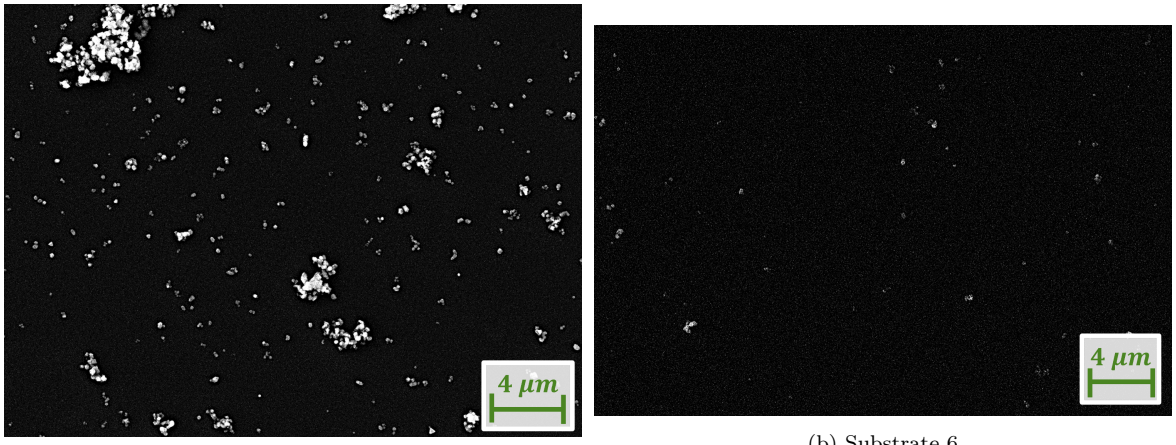

(a) Substrate 5

(b) Substrate 6

Figure 5.3: SEM imaging of substrate 5 and 6.

Table 5.1: Surface coverage of Al deposited Si substrates.

Substrate	**Surface Coverage [%]**
1	4.34
2	10.02
3	3.56
4	2.80
5	4.92
6	0.24

The surface morphology of the large and small Si cells is shown in Figures 5.4a and 5.4b. The large cell is shown to be almost completely covered in large agglomerations of Al nanoparticles. This was due to the deposition method, as the cell ended up in contact with the bottom of the solution container. Thus, depositing the Al nanoparticles onto the cell by dropping the cell into the solution is not a good deposition method. The image of the surface morphology of the small cell had a small number of nanoparticles coated onto its surface. No large agglomerations were present in the image compared to the surface morphology of the large Si cell. It was difficult to estimate the surface coverage of the cells, as the structured silicon seen as brighter areas in the image was often counted as nanoparticles. In the end, it was concluded that the uncertainty was

too large when trying to estimate the surface coverage, so it was left for now as no good solution for this was found.

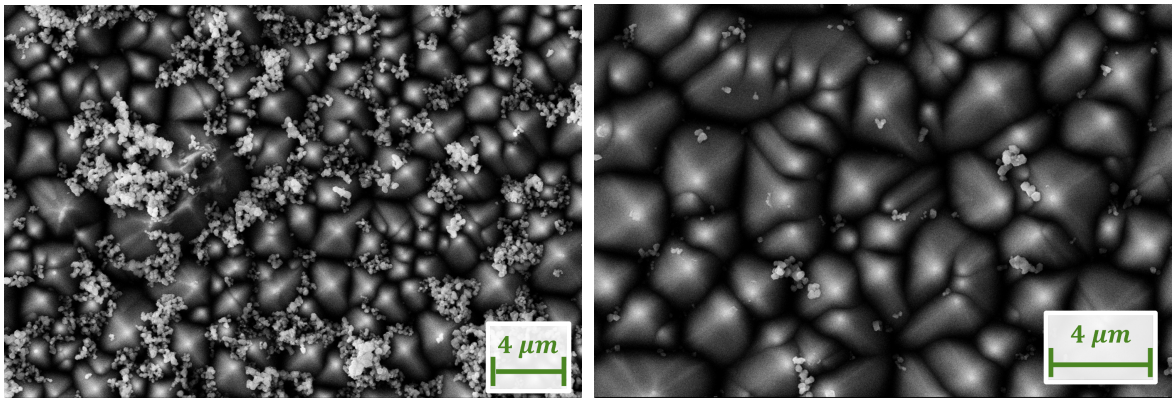

(a) Large Si cell (b) Small Si cell

Figure 5.4: SEM imaging of the large and small Si solar cells. Note that the large Si cell was imaged at a lower magnification due to the large agglomerations, while the small Si cell was imaged at a larger magnification due to the small nanoparticles.

5.2 The Efficiency of a Si Solar Cell With and Without Al Nanoparticles

In order to determine whether the pre- and post-deposition of the small Si solar cell had the same solar conditions when their efficiency was measured, the efficiency of a reference solar cell with no nanoparticles was measured on the day the pre-deposition cell was investigated. This efficiency was then compared to the efficiency measured for the same reference solar cell on the day the post-deposition cell was measured, where the efficiencies are given in Table 5.2. As can be seen, there was a large difference between the measured efficiency, indicating that the post-deposition measurements had different solar conditions such that the cell absorbed fewer photons compared to the pre-deposition cell. Due to the different solar conditions, the efficiencies measured for the post-deposition day yielded different efficiency, regardless of the nanoparticles.

Table 5.2: Efficiency of a reference cell, which had no nanoparticles, measured on different days.

Experiment Day	**Efficiency of a Reference Cell**
Pre-deposition	15.35
Post-deposition	14.59

The efficiency measured for the small Si cell, both pre- and post-deposition, is given in Table 5.3. The efficiency measured for the pre-deposition cell had a larger efficiency compared to the post-deposition cell. Even if the difference in solar conditions is considered, there was still a large loss in efficiency post-deposition.

Table 5.3: Efficiency of the small Si cell pre- and post-deposition of Al nanoparticles. Note that the difference in solar conditions has not been taken into account.

	Efficiency	
	Pre-deposition	**Post-deposition**
Measurement 1	17.00	12.95
Measurement 2	16.96	12.88
Measurement 3	16.95	12.90
Mean Value	**16.97 ± 0.03**	**12.91 ± 0.04**

There may be several reasons for the loss of efficiency post-deposition. One reason may be due to the agglomerated particles creating big particle clusters on the post-deposition Si cell, which, as shown in Figures 5.5a and 5.5b, are clearly visible even at a low magnification in an optical microscope. It is clear that so large clusters result in a significant geometric scattering, as discussed in Section 2.3.1, and consequently shadowing of the underlying solar cell. This has led to a significant amount of scattered and reflected light and consequently a decrease in efficiency. Other reasons the efficiency was low may be increased series resistance due to the nanoparticles acting as resistors, or causing electrical short-circuiting due to their deposition on both the front and backside, leading to disruptions in the circuit. This is ongoing work in the research group and is being investigated further. Due to the limited amount of available data in this thesis, no conclusion can be made at this point without further investigation.

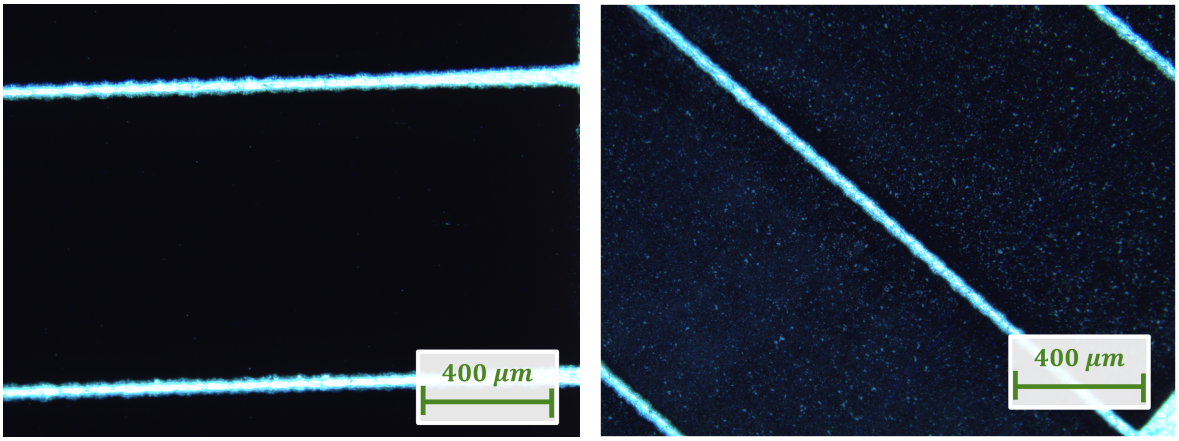

(a) Pre-deposition Si cell (b) Post-deposition Si cell

Figure 5.5: Imaging of the front surface of the pre- and post-deposition Si solar cells taken at the same settings. The post-deposition cell is shown to have large visible particle clusters.

This page intentionally left blank.

Chapter 6

Conclusion

The primary objective of this thesis was to investigate via numerical simulations if the efficiency of thin-film solar cells could be improved by using plasmonic nanostructures. Based on literature review carried out in the start of the thesis, it was decided that Al and In nanoparticles were the best candidates for enhancing light in-coupling into the CdTe and GaAs thin-film solar cells in question. As a first step, results for the GaAs solar cell were compared to existing literature, specifically the papers by Singh et al. [68] and Jangjoy et al. [69].

It was found that the absorption profiles obtained by the reproduced setup from the paper by Singh et al. [68] were found to have similar results as the paper, and the correlation with existing literature was good. However, the absorption profiles and current density obtained in the reproduced setup based on the paper by Jangjoy et al. did not give the same results as the published data [69]. One of the differences between Jangjoy et al. and the reproduced setup was that the absorption figures obtained for the Al nanoparticles in the paper had oscillations in the wavelength region 500 - 870 nm. This was determined in the thesis to be due to the inclusion of the back contact in the simulation region, as it led to thin film interference. The difference in magnitude for the absorption profiles and the current densities, was concluded to be due to differences in the material data used in the simulations and also due to mesh accuracy settings.

Another difference between the thesis and the paper by Jangjoy et al. was that the thesis also considered the current density calculated from the GaAs solar cell when it was coated in only the ARCs. It was determined that the addition of Al nanoparticles to the top of ITO could give a 2% increase in current density compared to a cell with only ITO. The Al nanoparticles also increased the current density for the GaAs cell with the SiO_2 ARC, where the cell had an increase of 4% and 13% in current density when the nanoparticles were placed on top of and embedded in the SiO_2, respectively, compared to the cell with only SiO_2. Based on these significant increases in calculated current densities, it can be concluded that Al nanoparticles are effective light trapping mechanisms for a GaAs solar cell with thickness of 500 nm, and with either ITO of thickness 40 nm, or SiO_2 of thickness 40 and 45 nm.

Next a detailed study of Al nanoparticles for increasing the efficiency of GaAs and CdTe solar cells was carried out. It found that it is possible to increase light in-coupling for both solar cell technologies. For the GaAs solar cell, Al nanoparticles enhanced the light absorption for a cell using two different absorbing layer thicknesses of 1500 and 500 nm. The largest enhancement in light absorption for the GaAs cell was 0.75% using an absorbing layer thickness of 1500 nm. This was obtained by using Al nanoparticles with a radius of 45 nm and a period of 300 nm. For the CdTe solar cells, Al nanoparticles enhanced the light absorption for a cell using two different absorbing layer thicknesses of 4000 and 1000 nm when the background material in the simulation was air. The largest enhancement in light absorption for the CdTe cell of absorbing layer thickness of 4000 nm was 1.76 %, which was obtained by using Al nanoparticles of radius 45 nm and a period of 250 nm.

The In nanoparticles only gave a positive enhancement to the CdTe cell without the glass substrate of both absorbing layer thicknesses. The largest enhancement of 0.59 % in absorption for the CdTe cell of thickness 4000 nm was obtained using In nanoparticles of radius 40 nm and period of 250 nm.

When the simulation considered a CdTe cell with the glass substrate, the addition of nanoparticles of either Al or In to the front surface did not positively enhance the light in-coupling. Therefore, it is concluded that both Al and In nanoparticles are unsuited for this specific CdTe solar cell configuration. As the layout of this specific configuration likely did not imitate a realistic CdTe fabrication, there may be other CdTe-glass configurations that will be receptive towards the use of these nanoparticles as a light trapping mechanism.

In conclusion, the addition of the Al nanoparticles as sub-wavelength scattering mechanisms only positively enhanced the light in-coupling in the absorbing layer when the thin-film solar cells were simulated in a background consisting of air. In the case of the In nanoparticles, only the CdTe cell without the glass substrate obtained an enhancement due to their presence. Despite the less steep increase in the imaginary component for the In metal, as shown in Figure 2.14b, the Al nanoparticle is found to be the most effective plasmonic material.

The secondary objective of the thesis was to experimentally investigate the effects of adding plasmonic Al nanoparticles on a crystalline silicon solar cell. The deposition of Al nanoparticles onto a small Si solar cell gave a worse efficiency compared to the pre-deposition state. Several theories have been made to explain why this is the case, such as increased series resistance, short-circuiting, or reflection from the Al nanoparticle agglomerations. The loss of efficiency was likely due to increased reflection from the agglomerated particles. However, no conclusive statement can be made whether all the loss was due to reflections without further investigation.

6.1 Further Work

The thesis has only looked at the effect of Al or In nanoparticles as sub-wavelength scattering mechanisms. Thus, investigating whether they can be used as sub-wavelength antennas in either GaAs or CdTe to enhance light in-coupling is a promising avenue for further research. Combining both scattering and antenna mechanisms may be of interest in future work.

Based on the results of the comparison between Jangjoy et al. [69] and the thesis (see Table 4.1), further investigation of the increase in current density for a GaAs cell with SiO_2 and Al nanoparticles may be of interest.

Due to the ongoing pandemic, only a few experiments were performed. Therefore, further investigation on how to deposit the Al nanoparticles with less amount of agglomeration is necessary. In addition, more research into the loss of efficiency from an Al coated Si solar cell must be performed to determine the cause.

This page intentionally left blank.

Appendix A

Script For Sweeps and Calculations

The script utilized for radius sweeps and calculations of Equations 2.29, 2.30, 2.32 and 2.31.

```
########################################################
# Description:  This file will calculate QE, IQE, G
# and J_sc of a solar cell with and without NPs
# The "sweep_material" must be set up manually in the
# Optimizations and Sweeps tab in the FDTD software

runsweep("sweep_material");

########################################################
# DATA COLLECTION FROM MONITORS

Ts=getsweepdata("sweep_material","Ts"); #Surface monitor
Tb=getsweepdata("sweep_material","Tb"); #Bottom monitor
Tr=getsweepdata("sweep_material","Tr"); #Reflection monitor
Tco=getsweepdata("sweep_material","Tco"); #TCO/ARC monitor
Tnp=getsweepdata("sweep_material","Tnp"); #NP monitor
#Tcds=getsweepdata("sweep_material","Tcds"); #CdS monitor

f=getdata("monitor_surface","f"); # frequency
nf=length(f); #number of data points in frequency

lambda = c/f;

absp_metal=-Ts+Tb;   # absorbed power within Absorbing layer


########################################################
#PLOTS, NON-NECESSARY
```

```
#plots Absorption
plot(lambda*1e9,absp_metal,"wavelength [nm]","Absorption");

#plots Reflection
plot(lambda*1e9,Tr,"wavelength [nm]","Reflection");

#plots Transmission
#plot(lambda*1e9,-Tb,"wavelength [nm]","Transmission");

#plots absorption in TCO/ITO
#plot(lambda*1e9,-Tco+Tcds,"wavelength (nm)","Loss in TCO/ARC");

#plots absorption in the NP space
#plot(lambda*1e9,-Tnp+Tco,"wavelength (nm)","Loss due to NP");

#######################################################

#Bandgap of substrate in room temperature
E_g = 1.42; #eV for GaAs
#E_g = 1.5; #eV for CdTe

#######################################################
# GET SOLAR SPECTRUM (I_AM1.5) DATA:

#get solar spectrum data:

wl_ssp0 = solar(0);      # wavelength vector in meters
ssp0 = solar(1);         # solar spectrum in Watts/meter^2/meter

nmin=find(wl_ssp0,0.3e-6);  #solar wavelength start
nmax=find(wl_ssp0,0.87e-6); #solar wavelength end

#Sets the solar wavelength in the range of min to max
wl1 = wl_ssp0(nmin:nmax);

#Sets solar spectrum in the range of min to max
ssp1 = ssp0(nmin:nmax);

wl_qe0 = flip(c/f,1);  #Makes a wavelength vector

#######################################################
# CALCULATES QE OF A SOLAR CELL
```

```
qe0_bare=flip(pinch(absp_metal(1:nf,1,1)),1);
qe0_r1=flip(pinch(absp_metal(1:nf,2,1)),1);


#######################################################
# CALCULATES NUMERATOR OF THE IQE EQUATION FOR SOLAR
# CELL BOTH WITH AND WITHOUT NANOPARTICLES:

#Calculates the numerator of the IQE equation
#The *100 is to normalize to the
#standard solar spectrum of P=100 mA/cm2

IQE_bare_n =integrate((wl1/h*c)*spline(qe0_bare,wl_qe0,wl1)*100*ssp1,1,wl1);
IQE_r1_n =integrate((wl1/h*c)*spline(qe0_r1,wl_qe0,wl1)*100*ssp1,1,wl1);


#######################################################
#CALCULATES THE DENOMINATOR OF THE IQE EQUATION

#The IQE for I_AM 1.5 spectrum
IQE_AM15 = integrate((wl1/h*c)*ssp1,1,wl1);

IQE_bare = IQE_bare_n/IQE_AM15;
IQE_r1 = IQE_r1_n/IQE_AM15;


#######################################################
# CALCULATES THE SHORT CIRCUIT CURRENT DENSITY WITH THE ASSUMPTION THAT
# ALL ELECTRON-HOLE PAIR CONTRIBUTES TO PHOTOCURRENT:

J_SC_bare = (((e*IQE_bare_n)/10)*e)/E_g;
J_SC_1 = (((e*IQE_r1_n)/10)*e)/E_g;


#######################################################
# CALCULATE G ENHANCEMENT FACTOR:

G_1 = IQE_r1/IQE_bare;
```

This page intentionally left blank.

Appendix B

Script For Convergence Testing

Script for convergence testing, slightly modified version of Lumerical's "testing_convergence_analysis.lsf" file [63].

```
########################################################
# Description:  This file will calculate CONVERGE
#     TEST FOR PML DISTANCE AND MESH ACCURACY
#   MODIFIED SCRIPT FROM LUMERICAL
# https://support.lumerical.com/hc/en-us/article_attachments/
#360049569373/testing_convergence_analysis.lsf
#
#
########################################################

########################################################
# SIMULATIONS FOR CONVERGENCE TESTING

#FINDS FREQUENCY
run;

f=getdata("monitor_surface","f"); # frequency

########################################################
#STARTS PML AND MESH ACURRACY SWEEPS

runsweep;

TS=getsweepdata("sweep_PML_distance","TS"); #Surface monitor
TB=getsweepdata("sweep_PML_distance","TB"); #Bottom monitor

TSM=getsweepdata("sweep_mesh_accuracy","TSM"); #Surface monitor
TBM=getsweepdata("sweep_mesh_accuracy","TBM"); #Bottom monitor
```

```
# Absorption in junction/absorbing layer for PML test
absp_PML=-TS+TB;

# Absorption in junction/absorbing layer for Mesh accuracy test
absp_mesh=-TSM+TBM;

######################################################
#CONVERGENCE TEST FOR PML DISTANCE

span = getsweepdata("sweep_PML_distance","z_span");
delta_s_abs_distance = absp_PML(1:length(f),2:length(span))
-absp_PML(1:length(f),1:length(span)-1);

delta_s_abs_distance = sqrt(integrate(delta_s_abs_distance^2,1,c/f) /
integrate( absp_PML(1:length(f),2:length(span))^2, 1, c/f) );

# delta_s_N
s_abs_distance_N = meshgridx(pinch(absp_PML,2,length(span)),span);

delta_s_abs_distance_N = s_abs_distance_N-absp_PML;

delta_s_abs_distance_N=sqrt(integrate(delta_s_abs_distance_N^2,1,c/f) /
integrate( s_abs_distance_N^2, 1, c/f) );

#makes a vector with the wanted x-axis number.
xAxis = 50:50:500;

# plot delta_s and delta_s_N
  plotxy(xAxis(2:length(xAxis)),delta_s_abs_distance,
         xAxis,delta_s_abs_distance_N,
         "Distance between monitor and boundary (nm)",
         "sigma_s","Deviation in PML Distance");
  legend("sigma_s","sigma_N");


######################################################
#CONVERGENCE TEST FOR MESH ACCURACY SETTING

mesh = getsweepdata("sweep_mesh_accuracy","mesh_accuracy");


# delta_s
delta_s_absp_mesh = absp_mesh(1:length(f),2:length(mesh))
-absp_mesh(1:length(f),1:length(mesh)-1);
```

```
delta_s_absp_mesh = sqrt( integrate( delta_s_absp_mesh^2, 1, c/f) /
integrate( absp_mesh(1:length(f),2:length(mesh))^2, 1, c/f) );

# delta_s_N
s_absp_mesh_N = meshgridx(pinch(absp_mesh,2,length(mesh)),mesh);

delta_s_absp_mesh_N = s_absp_mesh_N-absp_mesh;

delta_s_absp_mesh_N = sqrt( integrate( delta_s_absp_mesh_N^2, 1, c/f) /
integrate( s_absp_mesh_N^2, 1, c/f) );

# plot delta_s and delta_s_N
  plotxy(mesh(2:length(mesh)),delta_s_absp_mesh,
         mesh,delta_s_absp_mesh_N,
         "mesh accuracy setting","sigma_s",
         "Deviation in Mesh Accuracy");
  legend("sigma_s","sigma_N");
```

This page intentionally left blank.

Bibliography

[1] *The Paris Agreement.* https://unfccc.int/process-and-meetings/the-paris-agreement/the-paris-agreement. Accessed: 12-04-2021.

[2] Robert Curley, editor. *Renewable and Alternative Energy.* Energy: Past, Present, and Future. Britannica Educational Publishing, Rosen Educational Services, 2012.

[3] Ari Kahan. *EIA projects nearly 50% increase in world energy usage by 2050, led by growth in Asia.* https://www.eia.gov/todayinenergy/detail.php?id=41433. Accessed: 12-04-2021.

[4] Robert Curley, editor. *Fossil Fuels.* Energy: Past, Present, and Future. Britannica Educational Publishing, Rosen Educational Services, 2012.

[5] T.A. Boden, G. Marland, and R.J. Andres. *Global, Regional, and National Fossil-Fuel CO2 Emissions. Carbon Dioxide Information Analysis Center, Oak Ridge National Laboratory, U.S. Department of Energy, Oak Ridge, Tenn., U.S.A.*, 2017.

[6] Tomas Kåberger. *Progress of renewable electricity replacing fossil fuels. Global Energy Interconnection*, 1(1):48–52, 2018.

[7] IEA. *Evolution of solar PV module cost by data source, 1970-2020.* https://www.iea.org/data-and-statistics/charts/evolution-of-solar-pv-module-cost-by-data-source-1970-2020. Accessed: 13-04-2021.

[8] Aurélie Beauvais, Lukas Clark-Memler, Máté Heisz, Beatriz Ildefonso, and Raffaele Ross. *Global Market Outlook for Solar Power 2020 - 2024.* SolarPower Europe (2020).

[9] I.M. Dharmadasa. *Advances in thin-film solar cells.* CRC Press, 2018.

[10] F. Enrichi, A. Quandt, and G.C. Righini. *Plasmonic enhanced solar cells: Summary of possible strategies and recent results. Renewable and Sustainable Energy Reviews*, 82:2433–2439, 2018.

[11] Chetan Singh Solanki and Hemant Kumar Singh. *Anti-reflection and light trapping in c-Si solar cells.* Springer, 2018.

[12] Davy Gérard and Stephen Gray. *Aluminium plasmonics. Journal of Physics D: Applied Physics*, 48, 05 2015.

[13] Michael B. Ross and George C. Schatz. *Aluminum and Indium Plasmonic Nanoantennas in the Ultraviolet. The Journal of Physical Chemistry C*, 118(23), 2014.

[14] Shruti Sharma, Kamlesh Jain, and Ashutosh Sharma. *Solar Cells: In Research and Applications—A Review. Materials Sciences and Applications*, 06:1145–1155, Jan 2015.

[15] Bethel Afework, Jordan Hanania, Kailyn Stenhouse, Brodie Yyelland, and Jason Donev. *Photovoltaic cell.* URL: `https://energyeducation.ca/encyclopedia/Photovoltaic_cell`, Jun 2018.

[16] H. Victor Du John, D. Jackuline Moni, and D. Gracia. *A detailed review on Si, GaAs, and CIGS/CdTe based solar cells and efficiency comparison. PRZEGLĄD ELEKTROTECHNICZNY*, Des 2020.

[17] Philip Hofmann. *Solid state physics: an introduction.* John Wiley & Sons, 2015.

[18] Peter Würfel and Uli Würfel. *Physics of solar cells: from basic principles to advanced concepts.* John Wiley & Sons, 2016.

[19] H.D. Young, R.A. Freedman, A.L. Ford, F.W. Sears, M.W. Zemansky, and Pearson. *University Physics with Modern Physics, Global Edition.* Pearson Education, Limited, 2015.

[20] J. Van Zeghbroeck. *Principles of Semiconductor Devices.* Bart Van Zeghbroeck, 2011.

[21] Rod Nave. *Fermi level and Fermi function.* `http://hyperphysics.phy-astr.gsu.edu/hbase/Solids/Fermi.html#c1`. Accessed: 07-04-2021.

[22] G. Stepniak, M. Schüppert, and C.-A. Bunge. *8 - Polymer-optical fibres for data transmission.* In Christian-Alexander Bunge, Thomas Gries, and Markus Beckers, editors, *Polymer Optical Fibres*, pages 217–310. Woodhead Publishing, 2017.

[23] Neil W Ashcroft, N David Mermin, et al. *Solid state physics.* Holt, Rinehart and Winston, 1976.

[24] Adrian Kitai. *Principles of Solar Cells, LEDs and Related Devices: The Role of the PN Junction.* John Wiley & Sons, 2018.

[25] Rod Nave. *Bands for Doped Semiconductors.* `http://hyperphysics.phy-astr.gsu.edu/hbase/Solids/dsem.html`. Accessed: 07-04-2021.

[26] Karl W Böer. *Handbook of the physics of thin-film solar cells.* Springer Science & Business, 2014.

[27] Polina Anikeeva, Geoffrey Beach, and Niels Holten-Andersen. *3.024 Electronic, Optical and Magnetic Properties of Materials, Lecture 18*, Spring 2013. Massachusetts Institute of Technology: MIT OpenCourseWare.

[28] Rakesh Afre, N. Sharma, and Madhuri Sharon. *Transparent Conducting Oxide Films for Various Applications: A Review. Reviews on Advanced Materials Science*, 53:79–89, 01 2018.

[29] G. Leftheriotis, S. Papaefthimiou, and P. Yianoulis. *Development of multilayer transparent conductive coatings. Solid State Ionics*, 136-137:655–661, 2000. Proceedings of the 12th International Conference on Solid State Ionics.

[30] Sven Rühle. *Tabulated values of the Shockley–Queisser limit for single junction solar cells. Solar Energy*, 130:139–147, 2016.

[31] Pabitra Nayak, Suhas Mahesh, Henry Snaith, and David Cahen. *Photovoltaic solar cell technologies: analysing the state of the art. Nature Reviews Materials*, 4, 03 2019.

[32] William Shockley and Hans-Joachim Queisser. *The Shockley-Queisser limit. J. Appl. Phys*, 32:510–519, 1961.

[33] D.R. Myers. 1.12 - solar radiation resource assessment for renewable energy conversion. In Ali Sayigh, editor, *Comprehensive Renewable Energy*, pages 213–237. Elsevier, Oxford, 2012.

[34] C.S. Ferekides, U. Balasubramanian, R. Mamazza, V. Viswanathan, H. Zhao, and D.L. Morel. *CdTe thin film solar cells: device and technology issues. Solar Energy*, 77(6):823–830, 2004.

[35] Clark A. Miller, Ian Marius Peters, and Shivam Zaveri. *Thin Film CdTe Photovoltaics and the U.S. Energy Transition in 2020.* First Solar.

[36] Antonio Arce-Plaza, Fernando Sánchez-Rodriguez, Maykel Courel-Piedrahita, Osvaldo Vigil Galán, Viviana Hernandez-Calderon, Sergio Ramirez-Velasco, and Mauricio Ortega López. *CdTe Thin Films: Deposition Techniques and Applications.* In Jaime Andres Perez-Taborda and Alba G. Avila Bernal, editors, *Coatings and Thin-Film Technologies*, chapter 7. IntechOpen, Rijeka, 2019.

[37] Sunghyun Moon, Kangho Kim, Youngjo Kim, Junseok Heo, and Jaejin Lee. *Highly efficient single-junction GaAs thin-film solar cell on flexible substrate. Scientific reports*, 6(1):1–6, 2016.

[38] Jianling Xiao, Hanlin Fang, Rongbin Su, Kezheng Li, Jindong Song, Thomas F. Krauss, Juntao Li, and Emiliano R. Martins. *Paths to light trapping in thin film GaAs solar cells. Opt. Express*, 26(6):A341–A351, Mar 2018.

[39] J. Li, A. Aierken, Y. Liu, Y. Zhuang, X. Yang, J. H. Mo, R. K. Fan, Q. Y. Chen, S. Y. Zhang, Y. M. Huang, and Q. Zhang. *A Brief Review of High Efficiency III-V Solar Cells for Space Application. Frontiers in Physics*, 8:657, 2021.

[40] Xu Zhang, Xiao-Hong Sun, and Liu-Di Jiang. *Absorption enhancement using nanoneedle array for solar cell. Applied Physics Letters*, 103:211110–211110, 11 2013.

[41] Kangho Kim, Hoang Duy Nguyen, Sunil Mho, and Jaejin Lee. *Enhanced efficiency of GaAs single-junction solar cells with inverted-cone-shaped nanoholes fabricated using anodic aluminum oxide masks. International Journal of Photoenergy*, 2013.

[42] Dror Sarid and William A Challener. *Modern introduction to surface plasmons: theory, Mathematica modeling, and applications.* Cambridge University Press, 2010.

[43] Liudmila Nickelson. *Electromagnetic theory and plasmonics for engineers.* Springer, 2018.

[44] Stefan Alexander Maier. *Plasmonics: fundamentals and applications.* Springer Science & Business Media, 2007.

[45] Zeev Zalevsky and Ibrahim Abdulhalim. *Integrated nanophotonic devices.* Elsevier, 2014.

[46] Anatoly V. Zayats, Igor I. Smolyaninov, and Alexei A. Maradudin. *Nano-optics of surface plasmon polaritons. Physics Reports*, 408(3):131–314, 2005.

[47] Matthew Pelton and Garnett W. Bryant. *Introduction to metal-nanoparticle plasmonics*, volume 5. John Wiley & Sons, 2013.

[48] Heinz Raether. *Surface plasmons on smooth and rough surfaces and on gratings. Springer tracts in modern physics*, 111, 1988.

[49] David D. Evanoff Jr. and George Chumanov. *Synthesis and Optical Properties of Silver Nanoparticles and Arrays. ChemPhysChem*, 6(7):1221–1231, 2005.

[50] Charles Kittel. *Introduction to solid state physics.* John Wiley & Sons, 2004.

[51] Christoforus Satrya and Yudi Darma. *Dielectric-function analysis of metals for plasmonic-device application. Journal of Physics: Conference Series*, 877:012040, 07 2017.

[52] Cristian Della Giovampaola and Nader Engheta. *Plasmonics without negative dielectrics. Phys. Rev. B*, 93:195152, May 2016.

[53] M.S. Dresselhaus. *Solid state physics part ii optical properties of solids. Lecture Notes (Massachusetts Institute of Technology, Cambridge, MA)*, 2001.

[54] Edward D Palik. *Handbook of Optical Constants of Solids I-III*, volume 1 - 3. Academic press, 1985 - 1998.

[55] Mark W. Knight, Nicholas S. King, Lifei Liu, Henry O. Everitt, Peter Nordlander, and Naomi J. Halas. *Aluminum for Plasmonics. ACS Nano*, 8(1):834–840, 2014.

[56] Yasuaki Kumamoto, Atsushi Taguchi, Mitsuhiro Honda, Koichi Watanabe, Yuika Saito, and Satoshi Kawata. *Indium for Deep-Ultraviolet Surface-Enhanced Resonance Raman Scattering. ACS Photonics*, 1(7), 2014.

[57] Craig F. Bohren and Donald R. Huffman. *Absorption and scattering of light by small particles.* John Wiley & Sons, 1983.

[58] Uwe Kreibig and Michael Vollmer. *Optical Properties of Metal Clusters*, volume 25. Springer Berlin, 1995.

[59] Harry A. Atwater and Albert Polman. *Plasmonics for improved photovoltaic devices. Nature Mater*, 2010.

[60] *Finite Difference Time Domain (FDTD) solver introduction.* `https://support.lumerical.com/hc/en-us/articles/360034914633-FDTD-solver`. Accessed: 28-05-2021.

[61] *FDTD solver - Simulation Object.* `https://support.lumerical.com/hc/en-us/articles/360034382534-FDTD-solver-Simulation-Object`. Accessed: 04-03-2021.

[62] *Frequency-domain Profile and Power monitor - Simulation object.* https://support.lumerical.com/hc/en-us/articles/360034902393-Frequency-domain-Profile-and-Power-monitor-Simulation-object.

[63] *Convergence testing process for FDTD simulations.* `https://support.lumerical.com/hc/en-us/articles/360034915833-Convergence-testing-process-for-FDTD-simulations`. Accessed: 05-03-2021.

[64] *Solar cell methodology.* `https://support.lumerical.com/hc/en-us/articles/360042165634-Solar-cell-methodology`. Accessed: 05-03-2021.

[65] Robert Treharne, A Seymour-Pierce, K. Durose, K Hutchings, S Roncallo, and David Lane. *Optical Design and Fabrication of Fully Sputtered CdTe/CdS Solar Cells. Journal of Physics: Conference Series*, 286:012038, 04 2011.

[66] Tobias A. F. König, Petr A. Ledin, Justin Kerszulis, Mahmoud. A. Mahmoud, Mostafa A. El-Sayed, John R. Reynolds, and Vladimir V. Tsukruk. *Electrically Tunable Plasmonic Behavior of Nanocube–Polymer Nanomaterials Induced by a Redox-Active Electrochromic Polymer. ACS Nano*, 8(6):6182–6192, 2014. PMID: 24870253.

[67] Swagato Sarkar, Vaibhav Gupta, Mohit Kumar, Jonas Schubert, Patrick T. Probst, Joby Joseph, and Tobias A.F. König. *Hybridized Guided-Mode Resonances via Colloidal Plasmonic Self-Assembled Grating. ACS Applied Materials & Interfaces*, 11(14):13752–13760, 2019.

[68] Gurjit Singh and S.S. Verma. *Plasmon enhanced light trapping in thin film GaAs solar cells by Al nanoparticle array. Physics Letters A*, 383(13):1526–1530, 2019.

[69] Abolfazl Jangjoy, Hamid Bahador, and Hamid Heidarzadeh. *A Comparative Study of a Novel Anti-reflective Layer to Improve the Performance of a Thin-Film GaAs Solar Cell by Embedding Plasmonic Nanoparticles. Plasmonics (2020)*, Sep 2020.

[70] *Ultrasound cleaning baths, USC.* `https://no.vwr.com/store/product/10694225/ultrasound-cleaning-baths-usc`. Accessed: 30-05-2021.

[71] *Planar silicon solar cell.* `https://support.lumerical.com/hc/en-us/articles/360042165534-Planar-silicon-solar-cell`. Accessed: 05-03-2021.